LBL-23180 c.2

Lawrence Berkeley Laboratory

UNIVERSITY OF CALIFORNIA

Materials & Chemical Sciences Division

RECEIVED
LAWRENCE
BERKELEY LABORATORY

JUN 2 1987

LIBRARY AND
DOCUMENTS SECTION

DEFECTS IN ION IMPLANTED SILICON, INVESTIGATED BY TRANSMISSION ELECTRON MICROSCOPY

K.S. Jones
(Ph.D. Thesis)

March 1987

TWO-WEEK LOAN COPY

This is a Library Circulating Copy which may be borrowed for two weeks.

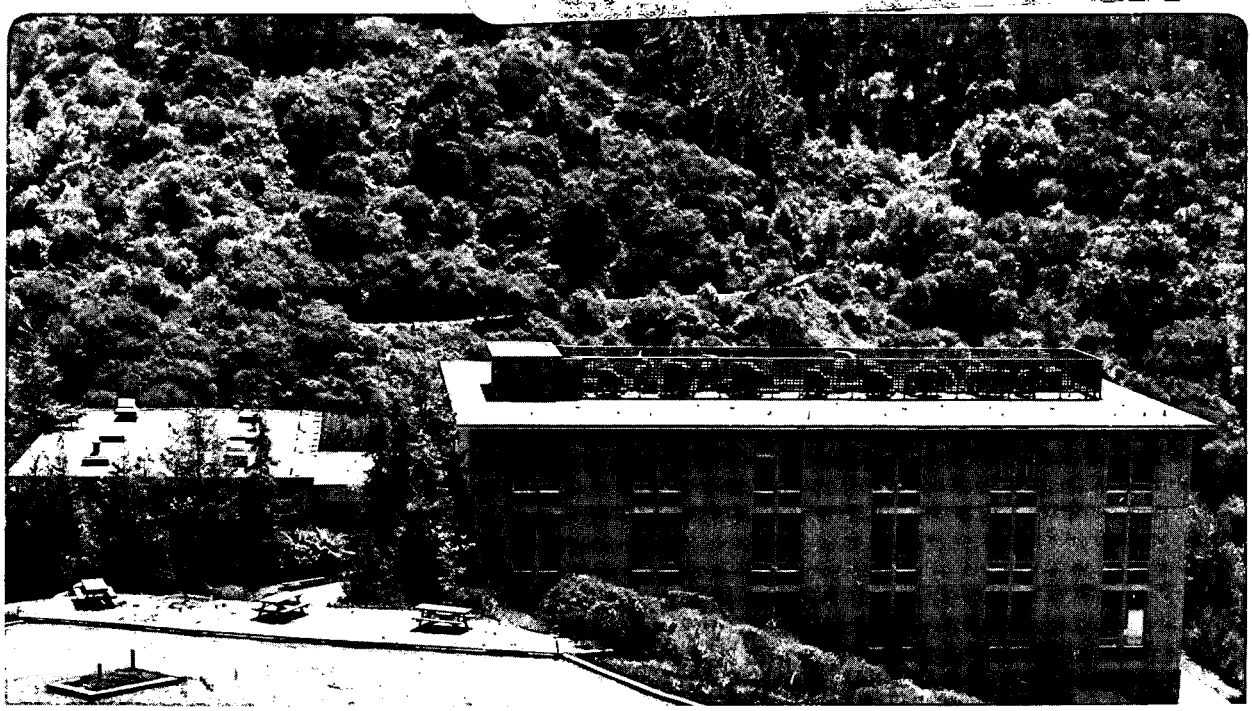

LBL-23180 c.2

Prepared for the U.S. Department of Energy under Contract DE-AC03-76SF00098

DISCLAIMER

This document was prepared as an account of work sponsored by the United States Government. While this document is believed to contain correct information, neither the United States Government nor any agency thereof, nor the Regents of the University of California, nor any of their employees, makes any warranty, express or implied, or assumes any legal responsibility for the accuracy, completeness, or usefulness of any information, apparatus, product, or process disclosed, or represents that its use would not infringe privately owned rights. Reference herein to any specific commercial product, process, or service by its trade name, trademark, manufacturer, or otherwise, does not necessarily constitute or imply its endorsement, recommendation, or favoring by the United States Government or any agency thereof, or the Regents of the University of California. The views and opinions of authors expressed herein do not necessarily state or reflect those of the United States Government or any agency thereof or the Regents of the University of California.

DEFECTS IN ION IMPLANTED SILICON, INVESTIGATED BY TRANSMISSION ELECTRON MICROSCOPY

KEVIN SCOTT JONES

(Ph.D. Dissertation)

Materials and Chemical Sciences Division
Lawrence Berkeley Laboratory and
Department of Materials Science and Mineral Engineering
University of California
Berkeley, CA 97420

March 1987

DEFECTS IN ION IMPLANTED SILICON, INVESTIGATED BY TRANSMISSION ELECTRON MICROSCOPY

Kevin Scott Jones

ABSTRACT

A classification scheme for the different forms of implant-related damage which arise upon annealing consisting of five categories is presented. The sources of the different types of damage along with their morphologies is discussed in detail.

Pre- and post-amorphization studies indicate that implantation of a preamorphized surface can result in a significant increase in the concentration of the category II (end of range) damage. The dose dependence of the increased category II damage becomes more enhanced with the increasing ion mass. This evidence has been used along with results from the category II defect studies to support a model that the category II damage concentration can be increased by the creation of free atoms in the amorphous layer which then migrate or recoil to the deeper category II damage layer.

We found the annealing kinetics to be dependent on the implant species and dose. Direct comparison of similar weight ions indicated quite different annealing kinetics with comparable initial damage distributions. An enhanced dissolution of the category II defects was observed for certain species. It appears this enhanced dissolution driving force is not directly a result of stress, impurity diffusion processes, the thermodynamic instability of dislocation loops or oxidation. The dissolution process occurs when the solid solubility was exceeded and the resulting precipitates were dissolving. The category II damage is much more stable when no precipitates are formed, as is true for Si and Ge implants over all dose ranges or for other ions when the implant dose is such that the resulting peak concentration is below solid solubility at the annealing temperature. When the precipitates are not dissolving as with antimony implants for our time, temperature regimes, the category II damage does not dissolve. Studies over several temperatures indicate an activation energy of approximately 5 eV for the dissolution process. A model for this enhanced dissolution process is proposed which involves the creation of an interstititial sink or generation of vacancies upon precipitate dissolution.

ACKNOWLEDGEMENTS

I will always be indebted to Si Prussin at T.R.W. Inc. for his initiative, support, endless discussions and friendship. Without his help this project would not have been possible. I am also grateful to Eicke Weber and Jack Washburn for their assistance and guidance. I would like to thank Devendra Sadana for performing so much of the initial work that led to this classification scheme and for his help, as well as Zuzanna Lilliental-Weber's help with the High Resolution TEM studies. A special thanks go to Brett Dyson for his assistance in preparing the many TEM specimens and to Hing Wong for generating the Brice damage density distribution curves. I would like to acknowledge the assistance of my fellow graduate students especially Mark Hoinkis and Lisa Parachanian-Allen.

I am most grateful to Debra L. Dauphin-Jones (my wife) for reviewing the manuscript thereby changing a basically unintelligible work into something readable and for her friendship, love, paitence and understanding. Finally, none of this would have been possible without the love and support from William M. Jones and Elizabeth N. Jones (my parents).

This work was supported by T.R.W. Inc. and the University of California M.I.C.R.O. Program. In addition, this work was supported by the Director, Office of Energy Research, Office of Basic Energy Science, Materials Sciences Division of the U.S. Department of Energy under contract #DE-AC03-76SF00098.

Table of Contents

	Page
1. Introduction	-1-
1.1 Ion Implantation: Theory and Purpose	-2-
1.2 Ion Implantation Damage	-4-
1.3 Amorphous Layer Formation	-5-
1.4 Amorphous Layer Regrowth	-9-
1.4.1 Wafer Orientation Effects	-9-
1.4.2 Dopant Effects	-10-
1.4.3 Ion Beam Induced Epitaxial Crystallization	-10-
2. Experimental Procedure	
2.1 Ion Implantation	-13-
2.2 AnnealingTreatments	-14-
2.3 Transmission Electron Microscopy	-15-
2.3.1 Plan-view TEM Sample Preparation	-15-
2.3.2 Cross-sectional TEM Sample Preparation	-16-
2.3.3 Microscopy Procedure	-19-
3. Damage Classification Scheme	-23-
4. Experimental Results	
4.1 Category I Damage	-32-
4.2 Category II Damage	-41-
4.2.1 Models for Defect Formation	-45-
4.3 Category III Damage	-60-
4.3.1 Hairpin Dislocations	-60-
4.3.2 Microtwins	-62-
4.3.3 Segregation Related Defects	-63-
4.4 Category IV Damage	-66-
4.4.1 {111} Oriented Wafers	-66-
4.4.2 {100} Oriented Wafers	-67-
4.5 Category V Damage	-74-
4.5.1 Precipitates	-74-
4.5.2 Half Loop Dislocations	-76-

Page

4.6 Defect Stability -98-

4.6.1 Enhanced Dissolution -99-

4.6.1a Activation Energy for Defect Dissolution -100-

4.6.1b Sheet Resistivity Measurements -102-

4.6.1c Model for Enhanced Dissolution -103-

5. Conclusions -112-

References -114-

Appendix 1 -127-

1. INTRODUCTION

During the past 25 years ion implantation has become increasingly important as a method of controllably doping the near surface region of semiconductors. The major dissadvantage of ion implantation is the damage which arises during implantation and the need to activate the dopant. In addition to creating large numbers of Frenkel pairs per incoming ion, due to nuclear collisions, the implantation process is inherently nonconservative in that it introduces a large concentration of extra atoms. The damage which develops from the displaced atoms and the implanted dopant atoms can adversely affect device performance. For example, the gettering of impurities to the core of dislocations in the damaged region can subsequently increase the leakage currents of any p-n junction regions traversed by the dislocations.

In the 1960's and 1970's the damage associated with the implantation process was removed by a high temperature (1100°C) furnace anneal. The impurity profile typically occupies a depth of less than a micron after implantation. However, diffusion of the implanted species during such high temperature annealing can result in p-n junction depths of several microns or more. When the device sizes were equally large, the problems of punch-through in field effect transistors were not a limitation. As device sizes decreased the deep diffusions of the implanted species were no longer acceptable. For this reason, the study of implantation damage is of increasing interest as methods for the dissolution of the defects are sought which do not result in a significant increase in the junction depths. The sub-micron device technology necessary for the next generation of integrated circuits is the driving force for investigating the types of implantation damage, how they arise and what influences the defect annealing kinetics.

This work represents a major effort on the part of the University of California at Berkeley and T.R.W. Inc. to understand the basic phenomena of implantation damage.

Over 2500 different plan-view and cross-sectional transmission electron microscope specimens have been examined to study the effect of implant species, dose, energy, annealing time and temperature, wafer temperature during implantation, wafer orientation, preamorphization and postamorphization on defects formed and their annealing kinetics.

1.1 Ion Implantation, Theory and Purpose

The potential application of ion implantation in the doping of semiconductors was realized around 1956,[1] and by 1962 the first papers were published on its use for the fabrication of thin contacts on nuclear radiation detectors.[2] Since these early beginnings a large volume of work has been done and many books and review articles written on ion implantation.[1,3-5] Today, ion implantation is the prefered doping technique in semiconductor processing. This is primarily due to several advantages it has over doping by surface in-diffusion.

Implantation provides a relatively low temperature means of controllably changing the chemical composition of the near-surface region of the target. The chemical profiles as well as the precise control of the quantity of dopant introduced are not attainable via diffusion from the surface. The relatively shallow initial profiles made possible by implantation are of increasing importance as the lateral dimensions of integrated circuit devices become smaller. The precise quantitative control afforded by implantation has been shown to result in increased consistancy of electrical device characteristics.[5,6]

In addition to limited control, surface source diffusion of phosphorus and boron, at the high doping concentration necessary for low resistivity contacts, is known to result in the formation of misfit dislocation networks. [7-11] This problem is relieved for phosphorus by the simultaneous diffusion of arsenic.

Ion implantation also has its drawbacks. The primary problem is that during the

implantation process the crystalline lattice of the semiconductor is damaged and an annealing step is necessary to repair the damage as well as to electrically activate the dopant. The damage which forms has many sources, which will be discussed in depth in the ensueing chapters. It suffices to say that the most common defect morphologies consist of dislocations which form upon annealing. These dislocations are known to be detrimental to device performances [12-17] resulting in for example increased emitter-base and collector-base leakage currents for bipolar junction transistors[14] as well as significat decreases in free carrier mobility.[15] Dislocations are unstable as the crystal approaches thermodynamic equilibrium, thus in order to reduce the kinetic limitations on defect elimination and to activate the dopant, an annealing treatment is used. During such annealing treatments concommitant diffusion will result in a broadening of the impurity profiles as well as loss of dopant by out-diffusion. The electrical activation of a significant fraction of the dopant is possible, upon annealing at relatively low temperatures (550°C) for most species implanted at doses above $1 \times 10^{14}/cm^2$. However, annealing at temperatures of 900°C or higher is necessary to eliminate the secondary defects (dislocations) which form when the primary damage is annealed.

Not all forms of implantation damage are unwanted as will be discussed further in the next section. This text will be concerned with those forms of damage which are detrimental to device performance.

Over the past decade, the main focus of ion implantation research has been how one can activate the implanted dopant and remove the damage while minimizing the amount of dopant redistribution. The optimal means of removing the damage cannot be realized unless those effects which dominate the defect annealing kinetics are thoroughly understood. A large quantity of work has gone into studying the defect structures which arise upon annealing. However, the limited understanding of the forces behind the different anneal

kinetics observed was the driving force behind this work.

1.2 Ion Implantation Damage: Basic Theory

Interaction between an incident ion and the electrons and nuclei of the target account for its loss of kinetic energy upon penetration of the target. At typical ion implant energies of 25-200 keV, light ions such as boron will lose most of their kinetic energy to inelastic processes. These include excitation of the target electrons to higher electronic states or complete ionization by the incoming ion. These processes do not directly result in the production of lattice displacements or damage to the crystal. Heavier ions, such as antimony, will lose most of their kinetic energy to elastic collisions between the incoming ion and target atom nuclei. This can result in the production of lattice displacements. Combining the elastic and inelastic loss mechanisms between the implanted ion and the target atoms, J. Lindhard and M. Scharff first proposed the statistical amorphous theory for ion energy loss in the keV energy range. This was later expanded and published by Lindhard, Scharff and Schiott,[18] thus becoming known as the LSS theory. This theory has been used by Gibbons, et al[19] to calculate the projected range and standard deviation for a large number of different ions implanted into different substrates.

Primary damage to the lattice arises from the creation of Frenkel pairs by the incoming ion or recoiled atoms. Kinchen-Pease[85] formulas have been used to estimate the number of displaced atoms. The number of displacements is proportional to the energy lost to elastic collisions divided by the energy necessary to create a Frenkel pair. [20, 21] Typical values of the energy for displacement of a silicon atom from its lattice site are around 15 eV at room temperature while values for energy lost to elastic collisions are several hundred times greater. Thus, each incoming ion will produce a large number of displaced target atoms. In order to understand and to predict how the different forms of damage evolve, it is necessary

to estimate the depth distribution of energy deposited into elastic collisions.

The elastic energy deposited per ion, at a depth x, is defined by:

$$S_n(x) = \int_0^\infty S_n(E)\, p(E;\, x,E_o)\, dE$$

where $S_n(E)$ is the Thomas-Fermi nuclear stopping power discussed by Lindhard et.al.[18] and $p(E;\, x,E_o)dE$ is the probability an ion has energy between E and E + dE at depth x. E_o is the initial ion energy. Using the above equation, Brice[22] has extended the transport equations derived by Lindhard et al [18] and Sigmund and Sanders,[23] from final ion distributions to energy deposition distributions and tabulated these values for a variety of substrates and implanted species. The equations used by Brice to partition the kinetic energy of the incoming ion are simplified by assuming that energy deposited into recoiling electrons does not reappear as energy deposited into elastic stopping processes. Brice's curves are based on statistical techniques which assume an amorphous target and thus are not accurate for predicting nuclear stopping in the channeling tail region. Experimental evidence substantiating Brice's model include early studies[24] which indicated that the ratio of the depth of the damage peak to the depth of the ion distribution peak was ~0.6 ± 0.1.

Additional methods for estimating ion and deposited energy distributions include Monte Carlo type simulations[26,27] i.e. the TRIM and MARLOWE programs which are more flexible than statistical methods but are inherently more computer-time consuming. Whether Monte Carlo type simulations or Brice's statistical estimates are more accurate in estimating the damage density distribution profile is still being studied.[28]

For a sufficiently high concentration of damage, it is possible to transform the crystalline silicon into the amorphous phase. The depth of this amorphous layer can be

used to test the different methods of calculating the damage density distributions. Recent results correlating the depth of the amorphous/crystalline interface(s) to Brice's calculations have been published[25] and will be discussed in depth in the following section.

In addition to Frenkel pair formation, point defect clusters and extended defects can form upon annealing. These appear in some instances to be associated with the net increase in the density of the crystal lattice. It will be proposed in section 4.2 that the excess interstitials, from the implantation dose coalesce into extrinsic dislocation loops with annealing. Two additional sources of extended defects include the annealing of any amorphous layer which forms, and exceeding the solid solubility of the dopant in the crystal. The source of these different forms of damage will be discussed in chapter 3.

Defects have been shown to be detrimental when they occur in the active region of the device. However, they can be useful if they occur elsewhere. It has long been known that unwanted impurities such as transition metals are gettered by defects.[29,30,31] Oxygen precipitates for example are used for intrinsic gettering of impurities.[32,33] Implant damage is also used for gettering by performing argon implantation on the backside of wafers.[29,30] There are numerous papers indicating implantation damage is very efficient for gettering impurities.[34,35,36] Thus, depending on its location and stability, ion implant damage can be either useful or detrimental. The focus of this text is on two topics; the source of the different implant related defects and what influences their annealing kinetics. In order to understand these topics it is necessary to understand amorphous layer formation during implantation and the subsequent annealing kinetics.

1.3 Amorphous Layer Formation

The formation of an amorphous phase in silicon has been extensively reviewed by Shih.[37] Amorphous silicon is believed to be composed of a random network structure.[38,39] In the model, the tetrahedral bonding and nearest neighbor distance, characteristic of the

diamond cubic lattice, are preserved. The amorphous phase does have variations in the next nearest neighbor distance through rotations and formation of 5, 7 and 8 member rings. Experimental evidence supporting some form of a random network structure for the amorphous phase includes Raman spectroscopy,[43,44] comparisons of diffuse x-ray scattering spectrums[37,45] and electron paramagnetic resonance (E.P.R.) measurements.[46,47,59] The density of the amorphous phase is known to be ~1% less than the density of the crystalline phase.[40] By studying deposited silicon films, Veprek et al[41] have shown that for a decrease in the linear lattice expansion $\Delta d/d_o$ = 0.01-0.02, the diamond cubic lattice becomes unstable with respect to the amorphous phase. The thermodynamic arguments[42,37] comparing the free

energy of the crystalline and amorphous phases, confirm this value of the linear lattice expansion as that necessary to make the amorphous phase more energetically favorable.

The cystalline to amorphous phase conversion has been shown to be a first order phase transformation and not just a gradual accumulation of point defects. Among the observations supporting this are high resolution TEM micrographs of the a/c interface indicating the transformation is atomically abrupt.[48-51] Raman spectroscopy,[52] electrical conductivity,[53] and the sign of the Hall coefficient[54] all show abrupt changes.

The physical reason silicon becomes amorphous via a first order phase transformation is believed to be associated with the highly directional covalent bonding which limits the flexability of the lattice in accomodating the mismatch between the bonding constrains and the degrees of freedom.[55] These bonding restraints make the formation of an amorphous phase upon implantation possible for semiconductors, where as the increased flexability of the metallic bond make amorphous layer formation impossible for metals.[56]

The amount of damage from implantation necessary to convert the crystalline surface to amorphous is dependent upon the mass of the implanted species, the wafer temperature during implantation, as well as the dose rate and implant energy. In an attempt to explain these dependencies, several models have been proposed. These models are usually divided into the heterogeneous and homogeneous nucleation models which apply to heavy ions at low temperatures and light ions at high implant temperatures, respectively.

The heterogeneous model was first proposed by Morehead and Crowder[57] and has been refered to and discussed extensively.[4,37,48,50,56,] The model assumes that an amorphous cylinder of radius R is created by each incoming ion and a portion of this cylinder's volume (∂R) remains crystalline due to the out-diffusion of vacancies. The out-diffusion of interstitials has also been considered.[37] This diffusion process is used to explain the temperature dependence of amorphous layer formation. Experimental evidence for heavier ions confirms the model's premise that amorphous layer formation involves the

overlap of amorphous zones.[4,48,50]

The heterogeneous nucleation model does not apply for light ions such as boron implanted into silicon. For this species, the homogeneous nucleation model is more accurate. The homogeneous nucleation model is based on the premise that when the point defect concentration reaches a critical value the system relaxes to an amorphous state.[58] This model has been further modified by the idea that the creation of small amorphous zones at the end of the light ion track act as nuclei for the subsequent crystalline to amorphous transformation.[37,48,50] These modifications may apply to low temperature (77K) or high dose rate implantation[37] of boron into silicon, however, as will be reported elsewhere, these modifications do not appear to apply to room temperature medium current implantation of boron.[60]

The models above indicate, theoretically, when the silicon should become amorphous and they correlate qualitatively with EPR[61] and RBS[37] data in estimating the temperature dependence of this process. However, the models fail to determine the type (buried or surface) or continuity (isolated pockets, continuous) of the amorphous layer. Understanding the type and continuity of the amorphous layer is crucial in understanding the defects which form upon annealing.

Stein et al[62] proposed the concept of a critical energy deposition or a threshold damage density. This is the amount of energy deposited into nuclear collisions that is necessary to change the crystalline lattice to an amorphous phase. The threshold damage density can be calculated by comparing the depth of the a/c interface(s) as measured for example by cross-sectional TEM[63] or tapered groove profilometry[26] with the damage density distribution curve calculated from Brice curves or Monte Carlo type simulations. The deposited damage per ion, necessary for amorphous layer formation, can be directly read off the graph. Multiplication of this value by the dose yields the threshold damage density. Initially a crude estimate of the threshold damage density was reported[4] as $\sim 10^{21}$keV/cm^3,

corresponding to 20eV/atom, for room temperature implantation. It is now known that the threshold damage density is a function of ion mass, dose rate and wafer cooling during the implantation. The concept of a threshold damage density appears to apply best to implants described by the heterogeneous nucleation model since our medium current room temperature B implantation results showed no correlation, in the framework of the threshold damage density, between the Brice curve and the resulting amorphous layer.

One of the disadvantages of calculating the threshold damage density is that it is very dependent upon the depth of the a/c interface. The interface, although atomically sharp, exhibits spatial undulations due to ion range straggling.[64] To minimize this effect, the a/c depth for a range of implant energies and/or doses is compared to the corresponding Brice curves. This has been done for room temperature, medium current (265μA) P and As implants.[25,63] The depth of the amorphous layer for these experiments was determined primarily by tapered groove profilometry. This technique was shown by us to correspond well with cross-sectional TEM measurements.[63] The effective threshold damage density, determined for this work by cross-sectional TEM, as well as previously reported values, as a function of ion mass are plotted in figure 1. The value are for room temperature (Waycool endstation[65]) medium-current (265μA) implant conditions. The error bars are for the reasons just discussed. Use of this data and the corresponding Brice damage density distribution curve allows one to estimate the type (if any) of amorphous layer which will result from implantation of silicon with most species between the energies of 25 and 200 keV. This data also applies only to {100} wafers, stabilized at room temperature during the implant and for a single dose rate (265 μA). Even with these restrictions, the use of the effective threshold damage density still represents the most accurate method of predicting the type and depth of the amorphous layer which is produced and the categories (types) of defects which may result upon annealing.

1.4 Amorphous Layer Regrowth

The regrowth of the amorphous layer is known to occur by the motion of the a/c interface not the nucleation of new crystals within the amorphous layer.[66] The thermal regrowth of the a/c interface has been studied by RBS[67,68] and TEM.[66,69] The velocity was shown to follow the Arrhenius curve:[67,68]

$$v = v_o \exp(-2.35\ eV/kT)$$

where v_o depends on the doping and wafer orientation. The activation energy reported from TEM investigations is ~2.9 ± 0.1 eV. This descrepancy may be due to the strong doping and wafer orientation dependence or the difference in measurement techniques.

1.4.1 Wafer Orientation Effects

It is well documented that the solid phase epitaxial regrowth velocity of the a/c interface is very dependent upon the orientation of the substrate. This was expected since similar orientational dependencies were exhibited by epitaxial growth from liquid and gas sources. Evidence indicates the the growth rates of {111} : {110} : {100} substrate material are proportional to 1 : 6.5 : 15 respectively.[69] The fact that {111} regrowth is much slower than {100}[70,71] has also been noted for ion beam induced epitaxial crystallization (IBIEC) or dynamic annealing.[72]

This orientational dependence has been explained by a model[69,73] which begins by assuming that for an atom to be a part of the crystal, two undistorted bonds must form. For the {100} surface, a single atom can attach anywhere but three adjacent atoms must attach simulatneously for the {111} surface. This is less probable, therefore, the {111} interface grows at a slower rate. The model also sucessfully explains the observation of microtwin formation upon regrowth of {111} implanted wafers, which will be discussed further in the chapter on category III defects.

1.4.2 Dopant Effects

Regrowth of the amorphous layer at 500°C (a typical regrowth temperature) results in activation of the implanted dopant with little redistribution.[74,75] Substitutional incorporation of the dopant is expected since group III, IV and VA elements prefer substitutional sites in silicon.[76] What is unusual, is the fact that substitutional concentrations incorporated upon amorphous layer regrowth can exceed the retrograde solid solubility by as much as 560 times.[64] Although excess concentrations of dopants can be incorporated on lattice sites, RBS studies of {111} and {100} wafers implanted with As and Pb at a high dose indicate that, for species with low solid solubility (such as Pb), redistribution of the implanted species can occur during amorphous layer regrowth.[77] This redistribution involves segregation at the moving a/c interface. Such segregation has also been reported for flourine in BF_2 implanted silicon[78] and can be responsible for a class of category III defects.

The incorporation and segregation of dopants by the motion of the a/c interface affects the regrowth rate.[79] Most Group III and VA dopants increase the regrowth rate of the amorphous layer by as much as an order of magnitude, while implantation with oxygen and inert gases is known to reduce the regrowth velocity.[70,80] These observations have prompted the idea that segregation of impurities at the regrowing a/c interface could influence the nucleation and propagation of growth steps.[73] In addition, it is speculated that cooperative reordering of the dopants at the interface and the inability of the lattice to accomodate the oxygen and inert gases may be responsible for the affects on the regrowth velocity.[70]

1.4.3 Ion Beam Induced Epitaxial Crystallization

Aside from thermal regrowth of the amorphous layer, it is also possible to regrow the amorphous layer by ion beam induced epitaxial crystallization (IBIEC).[81] IBIEC studies during Ar implantation of wafers not thermally heat sunk indicate that four stages exist.[82]

They are: 1) disorder production, 2) amorphous layer formation, 3) IBIEC, 4) modification of resultant crystal structure. Studies of IBIEC also indicate that the regrowth process is virtually athermal. and is controlled by point defect production and migration in the a/c interface region.[81,83] This is substantiated by HRTEM studies showing shrinkage of amorphous pockets when irradiated by 1.5 MeV electrons at room temperature.[48] It is proposed that during thermal regrowth of the amorphous layer the 2.35 eV activation energy is dominated by a 2.0 eV nucleation barrier.[81] This nucleation barrier is circumvented during IBIEC by point defect creation.

It will be shown that post implant annealing of samples which underwent a large amount of IBIEC, results in the same secondary defects as those produced by thermal annealing of heat sunk wafer and the possibility of additional defects arising from either imperfect regrowth of the amorphous layer (category III defects) or the increased likelihood of producing a buried amorphous layer and the concommitant (category IV) defects. In addition, the heating results in an increased threshold damage density and thus a larger number of category II (end of range) defects. In order to minimize the secondary defect concentration, it is best to minimize the amount of ion beam induced epitaxial crystallization.

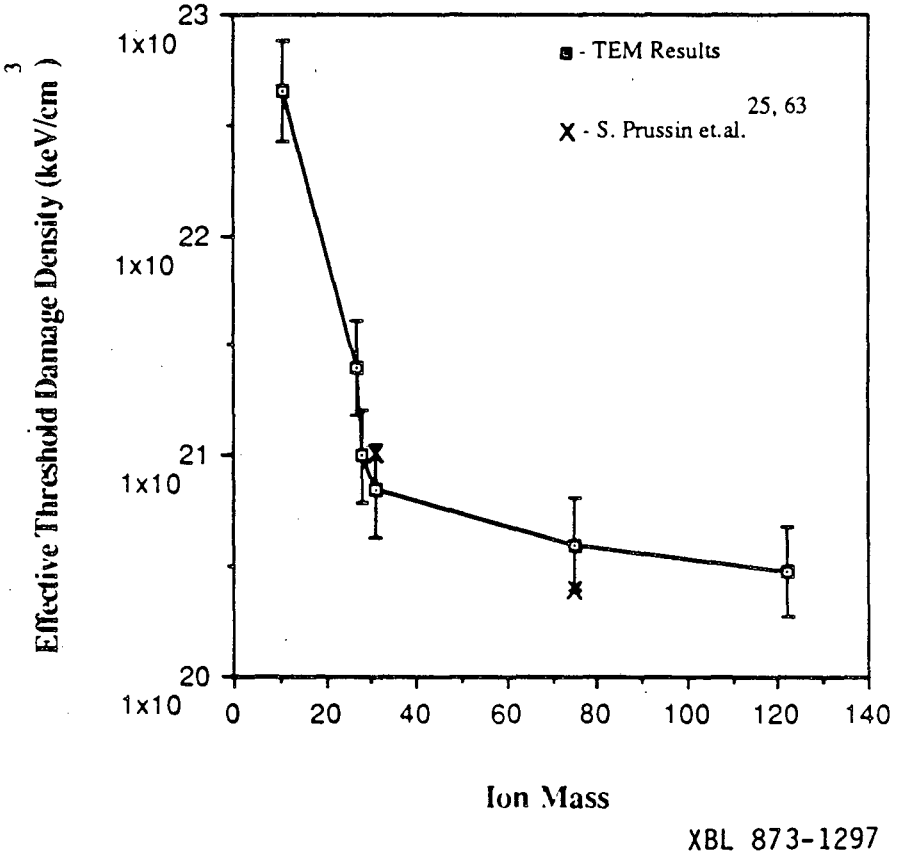

Figure 1

Effective Threshold Damage Density versus Ion Mass
Implant Temperature Stabilized at Room Temperature (Waycool Endstation)
Medium Beam Current (265 μA)

2. EXPERIMENTAL PROCEDURE

2.1 Ion Implantation

As previously mentioned, this study involved the production of over 2500 different plan-view and cross-sectional TEM specimens. Most of the implantations were done on a Varian medium current ion implanter model CF-3000. The wafers were typically 5-10 Ω-cm Czrochralski grown 3" or 4" wafers of type opposite the dopant to be implanted. The major thrust of the investigation was to determine the effects of ion species, dose, annealing time and temperature on the secondary defect annealing kinetics. For this reason the projected range (~600Å), dose rate (265μA), wafer orientation ({100}) and implant temperature (Waycool endstation, 300K) were kept approximately constant unless otherwise noted. Higher beam currents are being investigated for increased production throughput and new defects associated with these increased currents have been reported.[84] No dose rate studies were done in this work. Wafers of {111} orientation often have microtwins associated with amorphous layer regrowth, thus {100} wafers were used. The Waycool endstation uses circulating, room temperature, Freon^R to extract heat from the wafer during implantation. This is in contrast to the Wayflow endstation in which the wafer is thermally floating and cools primarily via radiative heat loss. Such slow cooling is ideal for ion beam induced epitaxial crystallization (IBIEC). The arguments presented in the previous section on the detrimental effects of IBIEC are some of the reasons why a Waycool endstation was used. Another reason was to control, as much as possible, the affects of beam induced heating, therein allowing for direct comparison of the different doses of the species on the defect annealing kinetics. The thermal trajectories for these two endstations was calculated by Prussin et. al.[25] as a function of arsenic dose. As shown for the Waycool endstation, the wafer theoretically only heats up to < 50°C while the Wayflow endstation results in the wafer heating up to ~200°C for a 1 x 10^{16}/cm^2, 100 keV arsenic implant which was the maximum dose used. The Waycool endstation is far more effective

in maintaining a constant wafer temperature. Finally, the wafers were clamped securely by a ring to the endstation. It has been shown that using a massive Cu holder at room temperature, it is still possible to heat the wafer as high as 270°C during implantation if poor thermal contacting is used.

2.2 Annealing Treatments

Research by Alessandrini et.al.[86] has shown that, for As implantation, a two stage annealing process resulted in the fewest secondary defects. The first anneal regrows the amorphous layer. By studying several temperatures between 500°C and 600°C, they determined that regrowth at 550°C resulted in the fewest secondary defects after the higher temperature second stage anneal which they chose to be 1000°C for 1 hour. For this reason, all of the implanted wafers were annealed in two stages. First the amorphous layer was regrown at 550°C, then the secondary defect formation, evolution and dissolution kinetics were studied at a higher temperature (900°C, 1100°C). The 900°C anneals were done in a furnace under a dry nitrogen atmosphere. The annealing times varied from 4 minutes to 72 hours. The other anneal temperature studied to any extent was 1100°C. A halogen lamp annealing system was used. The use of rapid thermal annealing in this time regime (seconds to minutes) is being actively investigated,[87,201,211] due to evidence (which will be discussed thoroughly) that indicates the activation energy for dissolving the secondary defects is greater than the activation energy for diffusion. Since the current goal of VLSI technology is to produce defect free p-n junctions with the minimum amount of diffusion, the above evidence suggests using shorter time, higher temperature anneals would be prefered. Laser annealing (nanosecond time regime) was extensively studied in the late 1970's until it was shown that such annealing introduces quenched-in electrically active defect centers.[88] Thus, annealing times between microseconds and minutes are now being studied.

2.3 Transmission Electron Microscopy

It is possible to detect the physical damage resulting from ion implantation by a number of methods of which Rutherford backscattering (RBS) and transmission electron microscopy (TEM) have been used most extensively. It is known[89] that TEM has a higher sensitivity than RBS for detecting the presence of implantation damage. Attempts to improve RBS resolution have been made[94] by correlating different defect structures observed by TEM with the corresponding RBS spectra, but there still exists the problem of errors in interpretation of the results. In addition, characterization of the different forms of damage (dislocations) is essential to understanding their evolution and is only possible by TEM. Although RBS yields depth information as well as lattice location (interstitial/substitutional) information, correlation of plan-view and cross-sectional TEM samples yields the three dimensional information which is manditory if a thorough understanding of the origins of the various forms of damage is to be attained. RBS does not involve as much sample preparation time as TEM. However, the sample preparation time has been dramatically reduced using the techniques to be described.

2.3.1 Plan-view TEM Sample Preparation

The standard method[90] of preparing a plan-view Si TEM sample involves cutting (drilling) a 3 mm diameter disc from the wafer, lapping the sample, mechanical dimpling of the surface and jet etching a hole from the backside (unimplanted side) of the disc. The drilling operation is time consuming and only one potential sample is prepared at a time.

A new method which was used for all plan-view TEM sample preparation in this study is presented here. After each anneal, two pieces of each wafer (~1.5cm x ~1.5cm) were cleaved off. One was used for plan-view TEM sample preparation and the other for cross-sectional TEM sample preparation. Typically, there were several species at many doses being studied enabling a large number of samples to be produced from a single anneal treatment.

Procedure

1. Fifteen to twenty of these pieces were mounted, implanted side up, on a 4" dummy wafer using crystalwax (figure 2). Crystalwax is an adhesive that melts at around 150°C and is soluble in acetone.

2. Using a Tempress[R] dicing saw*, 2.12 mm x 2.12 mm squares were cut out of the mounted pieces. These squares are 3mm in the diagonal direction and so will fit into the TEM sample holder.

3. Eight to nine different squares are mounted onto a lapping jig using crystalwax and lapped from the backside (unimplanted) until they are ~150 μm thick using 5 μm abrasive.

4. The squares are removed from the lapping jig, cleaned in acetone aand the implanted surface is dipped in molten parafin to protect it during etching.

5. Each square sample is etched from the backside using a South Bay Technologies jet etching apparatus. An optical detection system stops the jet etching process just prior to a hole being produced. A slow etch (buffered etch) is used to produce the final hole.

6. After removing the wax with n-heptane, the sample is ready for TEM examination.

Cutting the samples takes approximately 1 hour and preparartion of 8 samples takes about 3 hours for an average preparation time of 30 minutes per sample. This is a dramatic time savings over the standard sample preparation method.

*A dicing saw is commercially available and is used by the semiconductor manufacturing industry to slice processed wafers into chips for packaging. Producing the maximum number of chips per wafer is of the utmost importance, so dicing saw technology has developed to the point where the diamond blade widths are about 25 microns.

2.3.2 90º Cross-Sectional TEM Sample Preparation

Conventional cross-sectional sample preparation[91-93] involves cleaving off two pieces

of the wafer ~2-3 millimeters wide and glueing the surfaces of interest together. After glueing, the sample is lapped from its initial thickness down to ~200 microns. Then, the sample is often dimpled (a small indentation ground into the surface) and finally ion milled to produce a hole. The time to lap the sample is often 6-8 hours and only a single specimen can be done at a time as the thickness from sample to sample varies. The dimpling operation can take several hours and ion milling times of 8-12 hours are not unusual. Thus, preparation of a single sample can be quite time consuming. An alternative approach was proposed[94a] which involved glueing the samples together with parafin after the lapping operation and jet etching a hole through the cross-sectional sample. Many attempts to reproduce this method proved unsuccessful. However, an alternative approach was developed which greatly reduced the sample preparation time and several hundred samples have been produced.

This new technique, as with plan-view sample preparation, involves the use of a dicing saw. The primary time savings from this technique arise from the ability to slice strips 100-150 microns wide as opposed to cleaving strips and to produce a large number of samples with the exact same thickness so that more than one specimen can be prepared at a time.

Procedure

1. The samples to be processed (usually pieces of wafers 1.5 X 1.5 cm) are mounted on a dummy wafer by using crystalwax. The samples are arranged in a straight line so that each pass of the saw blade will cut as many as possible (see figure 3). As seen in the figure, a gap is left between the samples which aids in the removal of the strips after cutting by enabling the pieces to be slid out while the wafer is being heated.

2. After mounting the samples and pressing them down to insure they are as flat as possible, they are cut with the dicing saw into strips approximately 100 microns wide. The speed at which the blade travels across the wafer should be slow enough to not tear the slices out.

3. After slicing , the strips are removed by heating up the dummy wafer (which was only scratched by the saw) and sliding the strips out. These strips are placed in acetone to remove any excess glue.

4. After cleaning, the implanted (shiny) side of the strips are glued together using Ablebond 789-3 epoxy. In addition to the two slices of interest, an additional dummy slice is glued to the unimplanted sides to increase the total width to four thicknesses. This protects the inner two pieces, and makes the use of a laser stop on the ion mill possible. Pressing the slices together with tweezers is adequate for obtaining good contact between the slices. As many as ten different samples are glued at one time.

5. The epoxy is cured in an oven with the strips resting on a teflon pad.

6. The glued slices are mounted on a lapping jig as with the plan-view samples and a minor (1 micron grit) lapping of each side is done to remove any excess glue. The thickness of the slices decreases from 100 μm to ~40 μm during lapping.

7. The lapped strips are mounted, using epoxy, onto 3mm diameter Cu discs which have a 1x2mm oval in them. The interface of the center strips is aligned with the long axis of the oval hole.

8. A brief dip in a slow etch after mounting the slices on the Cu holder was found to reduce the ion milling time by 1-2 hours.

9. Finally, a hole is produced through the samples using a Gatan ion mill. The ion mill used a 5.5 kV Ar^+ beam with a beam current of 0.5 mA. The samples were tilted 15° from edge-on and two guns were used (0.25 mA/gun). A laser auto-terminator was used to determine when a hole had been created. It was discovered that if only two slices were glued together the hole in the Cu disc was not always covered and use of the auto-terminator was not possible. Thus, four slices were used to ensure complete coverage of the hole.

Once the samples are sliced, it typically takes ~4 hours to produce eight samples which are ready for ion milling. The ion milling time varies with the final sample thickness as shown in figure 4. The average milling time was 2-3 hours per sample. Thus, the time

per sample is reduced from approximately 20 hours per sample to about 4 hours per sample. This is still more time consuming than plan-view preparation, and as such is not used as extensively. The time saved in producing both plan-view and cross-sectional TEM samples was necessary for the thorough investigation of implantation damage as a function of the several parameters mentioned.

2.3.3 Microscopy Procedure

TEM micrographs were taken of each condition (species, dose, anneal time and temperature) to characterize the secondary defects. For the majority of the micrographs, diffraction contrast was used to image the defects. Kinematical and dynamical electron contrast theory[95,96] is well understood and excellent reviews have been published by Edington[97] and others.[98,99]

The secondary defects arising from implantation damage are, in general, dislocations (loops, half loops, networks). Diffraction contrast theory predicts that a defect is visible if $\mathbf{g} \cdot \mathbf{R} \neq 0$ where **g** is the reciprocal lattice vector corresponding to the diffracting plane and **R** is the strain vector (or Burgers vector for a dislocation) of the defect. For both the plan-view and cross-sectional samples a 2-beam condition was used with $s > 0$, where s is the deviation from the exact Bragg condition. Since the Burgers vectors for most of the dislocations were of either a/2<110> or a/3<111> type, the g_{040} reflection was used for the plan-view samples in order to image both sets of dislocations with Burgers vectors parallel to the {001} surface (a/2[110] type). This is important in detecting network dislocations as well as half loop dislocations to be discussed in the chapter on category V defects. The g_{220} reflection was used for the cross-section samples because the defect constrast intensity was greatest for this reflection.

Characterization of the Burgers vectors and habit planes of the dislocation loops was done using conventional techniques.[97,98,100,101,102] For all tilting experiments, the Kikuchi electron diffraction lines were used to determine the position in reciprocal space.[105]

The intrinsic/extrinsic nature of the loops was determined using a technique described by Dahmen et al.[103] The loop is tilted edge-on, then tilted away from edge-on by ~20-30° and photographed with plus (+) and minus (-) g reflections. Positive g is defined as pointing back towards the edge-on orientation. If the loop exhibits outside contrast with +g and inside contrast with -g then it is extrinsic in nature. This follows directly from kinematical diffraction contrast theory.[104]

In some instances it was necessary to use weak beam dark field[106] (WBDF) conditions to increase the resolution of the dislocations. This technique involves using a large deviation parameter $|s| \geq 0.02$ Å^{-2} and results in increased resolution since only the region of highest strain, that closest to the dislocation core, diffracts the beam sufficiently to yield contrast in the image.

Most of the high resolution images[97,107,122,137] were taken on a Philips 400 electron microscope modified with high resolution pole pieces. The images were taken under bright field axial illumination with the foil oriented such that the beam was parallel to the (110) pole. Seven Bragg beams ±(111), ±(111), ±(002) and the transmitted beam were included in the objective aperture and used for image formation. These seven beams were used because they were the only planes within the zero-order pass band of the contrast transfer function.

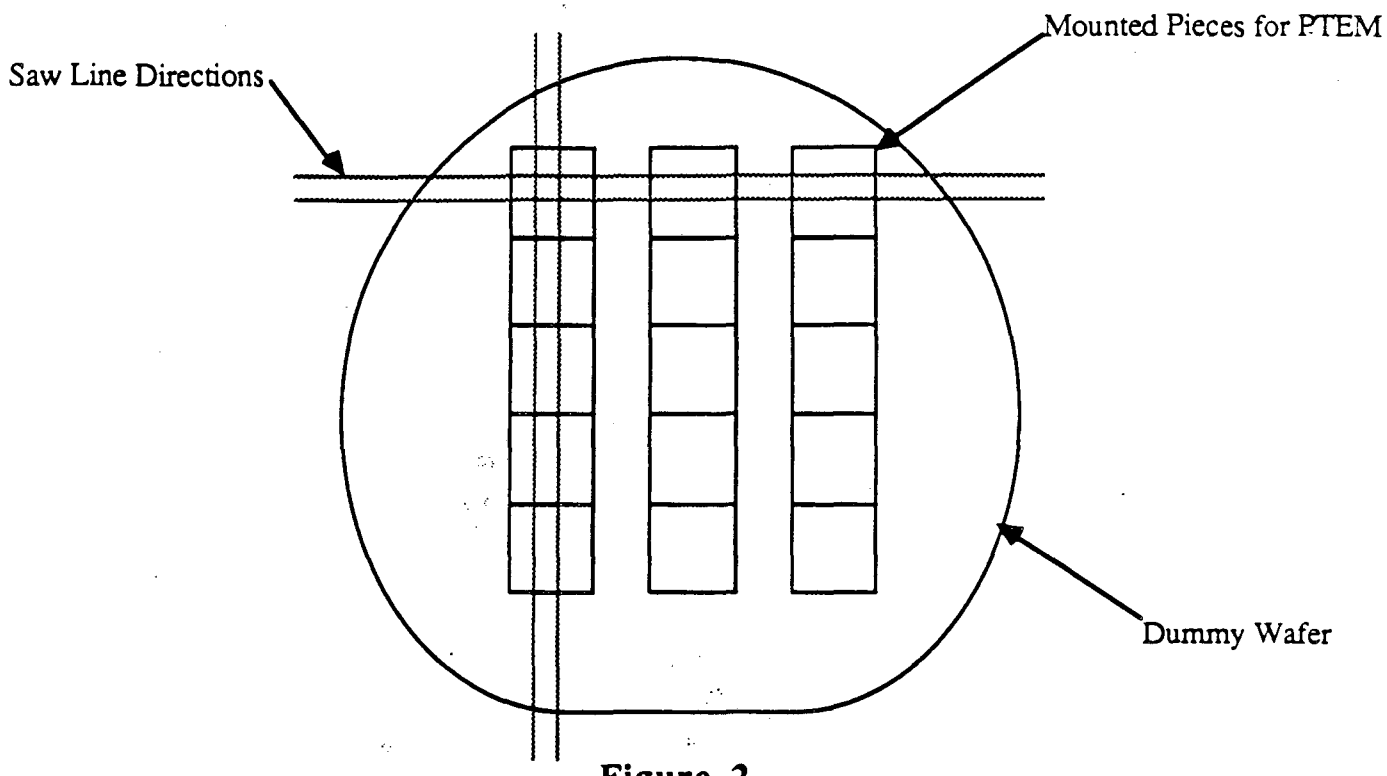

Figure 2

Plan-View TEM Sample Preparation

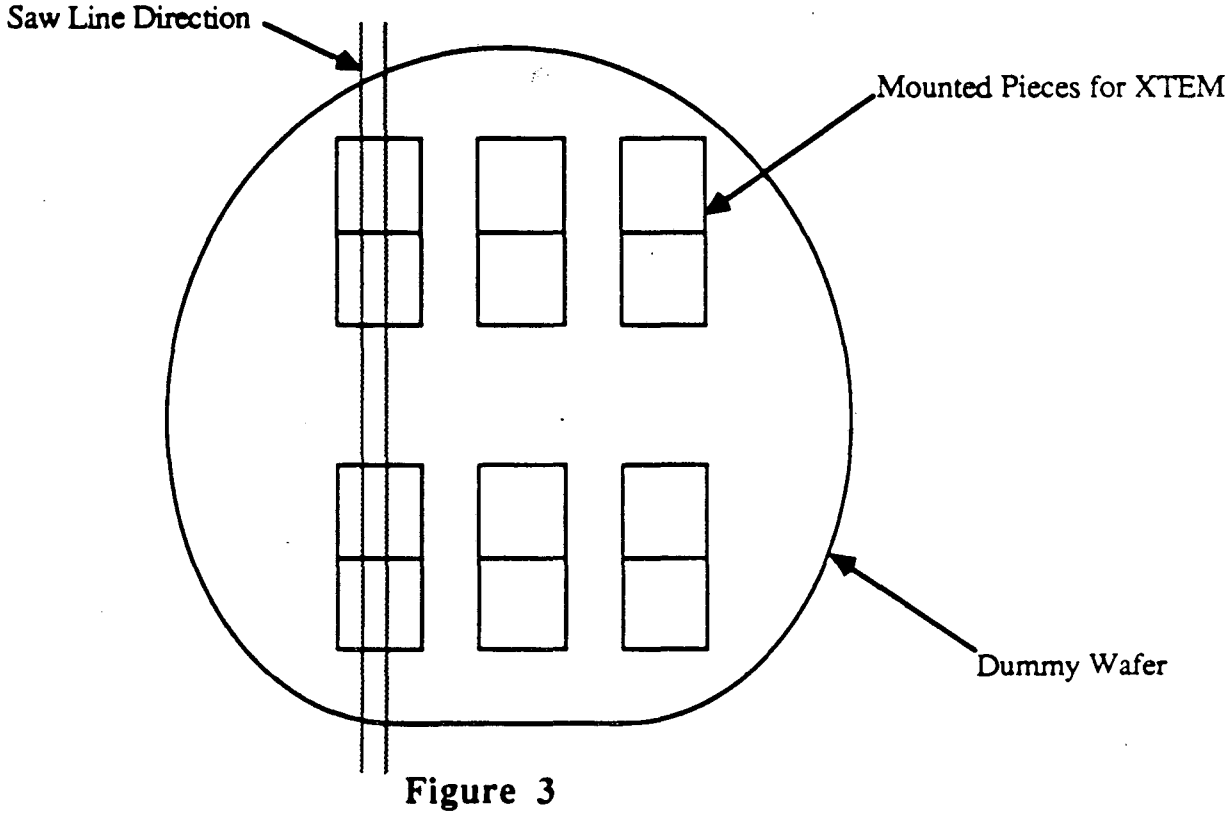

Figure 3

Cross-Sectional TEM Sample Preparation

XBL 873-1298

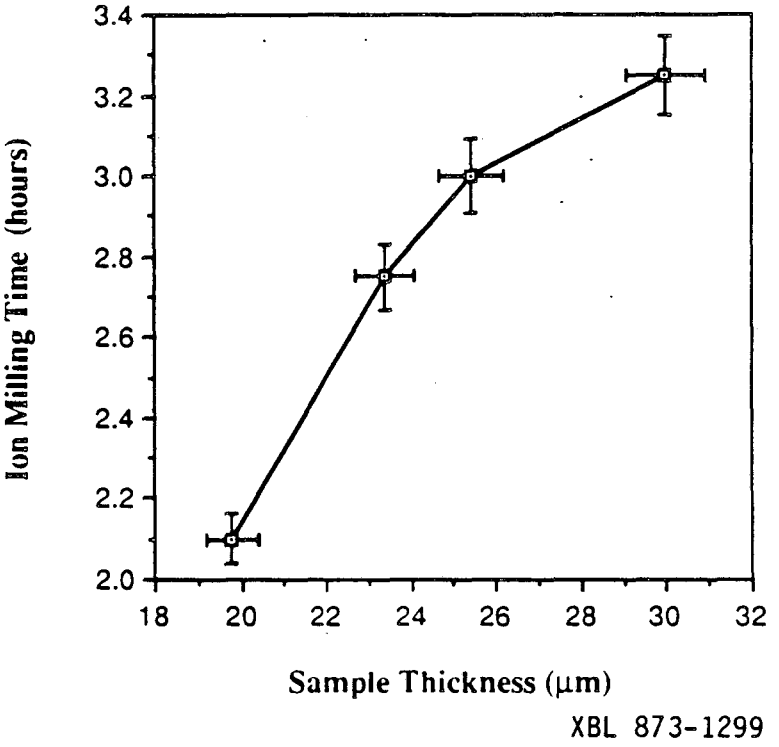

Figure 4

Ion Milling Time for Cross-Sectional TEM Sample Preparation
5.5 kV Ar^+ Beams
Beam Current 5 mA (2.5mA per beam), 15° Incident Angle

3. DAMAGE CLASSIFICATION SCHEME

Comparison of the damage density distribution curve with the concept of an effective threshold damage density leads to three possible conditions arising from implantation. No amorphous layer forms if the dose is too low or the effective threshold damage density is too high. With increasing dose or decreasing threshold damage density, a buried amorphous layer forms first which can upon continuing implantation grow to the surface, forming a "surface" amorphous layer or one that is continuous from the surface down to a certain depth. This transition is important in determining the type of secondary defects that arise from annealing.

A classification scheme[63,108] has been developed for the secondary defects which arise or develop during annealing of implanted silicon. This classification scheme sucessfully groups all secondary defects into five categories based upon the origin of the damage. The categories are closely related to the morphology of the near surface region specifically that of the amorphous layer (if any) resulting from implantation. To understand the origins of the different types of damage, it is necessary to correlate plan-view and cross-sectional annealed TEM samples with the corresponding as-implanted cross-sectional samples to determine the amorphous layer morphology. This chapter is an introduction to the proposed classification scheme. Chapter 4 will discuss each of the categories in further detail. It should be stated that this classification scheme applies quite well to our implantation results for energies $\leq$ 200 keV. There may exist additional sources of extended defects, especially for MeV implantations, but none were observed by us.

Category I Damage

This damage forms when the dose exceeds a critical value and simultaneously no amorphous layer is formed. Another term for this damage is "sub-threshold" damage. Figure 5a shows a schematic of the relationship between the damage density distribution

and the effective threshold damage density. This curve is a schematic and does not correspond to any particular species, dose or energy. Also shown is the location of the defects. These defects (e.g. figures 6 and 7) are typically extrinsic dislocation loops. For room temperature implantation, this damage is typically associated with light ions (^{11}B) since the effective threshold damage density is high and the critical dose (~1 x $10^{14}/cm^2$) can be exceeded without the formation of an amorphous layer. This concept of a "critical dose" is an empirical observation based on our experiments. The ramification of this concept is that for heavier species, where amorphization begins below this critical dose, no category I defect formation is possible.

The characteristics of category I damage include its location being centered around the projected range of the implanted species. The concentration of the category I dislocation loops was observed to increase proportional to the dose. This damage, although it evolves upon annealing, is quite stable with respect to dissolution. It is proposed that category I defects arise from increasing the density of the lattice by the implantation process. According to our model, upon annealing the extra atoms (implanted ions or most probably silicon interstitials) coalesce into the observed extrinsic dislocation loops.

Category II Damage

This damage arises whenever an amorphous layer is produced. It is also known as "end of range" damage. The location of this damage is beneath the amorphous-crystalline interface in the heavily damaged but still crystalline material. Figure 5b shows a schematic of the position of the a/c interface and the location of the category II defects. Similar to category I damage, only extrinsic dislocation loops are observed to form upon annealing (e.g. figure 12). The concentration of category II defects is not as strong function of dose as catagory I defects due to the existence of an amorphous layer which increases in thickness as the dose increases. An in-depth analysis of the factors influencing the concentration of these defects, including ion mass, pre- and post amorphization, species

solubility and implant temperature will be presented. The activation energies for dissolution of these dislocation loops will also be discussed.

Category III Damage

Regrowth of the amorphous layer can result in the formation of category III damage. The location of these defects is in the region previously occupied by the amorphous layer, as shown in figure 5c. There are several forms of category III damage. Hairpin dislocations or "spanners" nucleate when the regrowing amorphous/crystalline interface encounters pockets of misoriented crystalline material within the amorphous material. In our experiments, these defects were only encountered when a Wayflow endstation (one that allows the wafer to heat up during implantation) was used. Most of our research used the Waycool endstation so that hairpin dislocations, which are well understood, were not formed and subsequently not studied. Other forms of category III damage are microtwins which can result upon regrowth of amorphous layers on {111} oriented wafers. There have also been reports of defect formation just beneath the surface associated with rejection of species such as flourine by the advancing a/c interface, if the dose is sufficient. Since extensive work in the past has been done characterizing these defects and the defects were avoided for most of our studies, this work will not discuss category III defects in great detail.

Category IV Damage

A buried amorphous layer forms first with increasing dose. Regrowth of a buried amorphous layer occurs by the motion of both amorphous/crystalline interfaces. This leads to the creation of category IV defects at the depth where these two interfaces meet, as illustrated in figure 5d. These defects have also been termed "clamshell" or "zipper" defects (e.g. figure 24). Category IV defects can be avoided by decreasing the implant energy, increasing the dose or decreasing the implant temperature, all of which alter the relationship between the damage density distribution and the effective threshold damage density in favor

of producing a surface amorphous layer. The influence of wafer temperature, orientation and species on the type of category IV defects formed upon annealing have been investigated and will be presented.

Category V Damage

It is possible to exceed the solid solubility of a species in the target by ion implantation. Upon regrowth of the amorphous layer, all of the dopant within the amorphous layer is incorporated on lattice sites. When annealing at higher temperatures (>700°C), precipitation of the dopant is often observed by electrical measurements. Defects associated with the precipitation phenomena are sometimes observed to form at a depth corresponding to the projected range of the dopant. The defects include both dislocation loops and precipitates. Their location is illustrated in figure 5e. Figure 30 shows some examples of category V defects. The dissolution of these precipitates for certain species (Ga, P, and As) has a major effect on the category II damage. This effect includes the complete elimination of category II defects after relatively short time, low temperature annealing treatments (900°C, 4 hours, 1100°C 2 seconds). The morphology of the precipitates has been studied by high resolution TEM and the dissolution kinetics have been studied by Hall effect and sheet resistivity measurements.

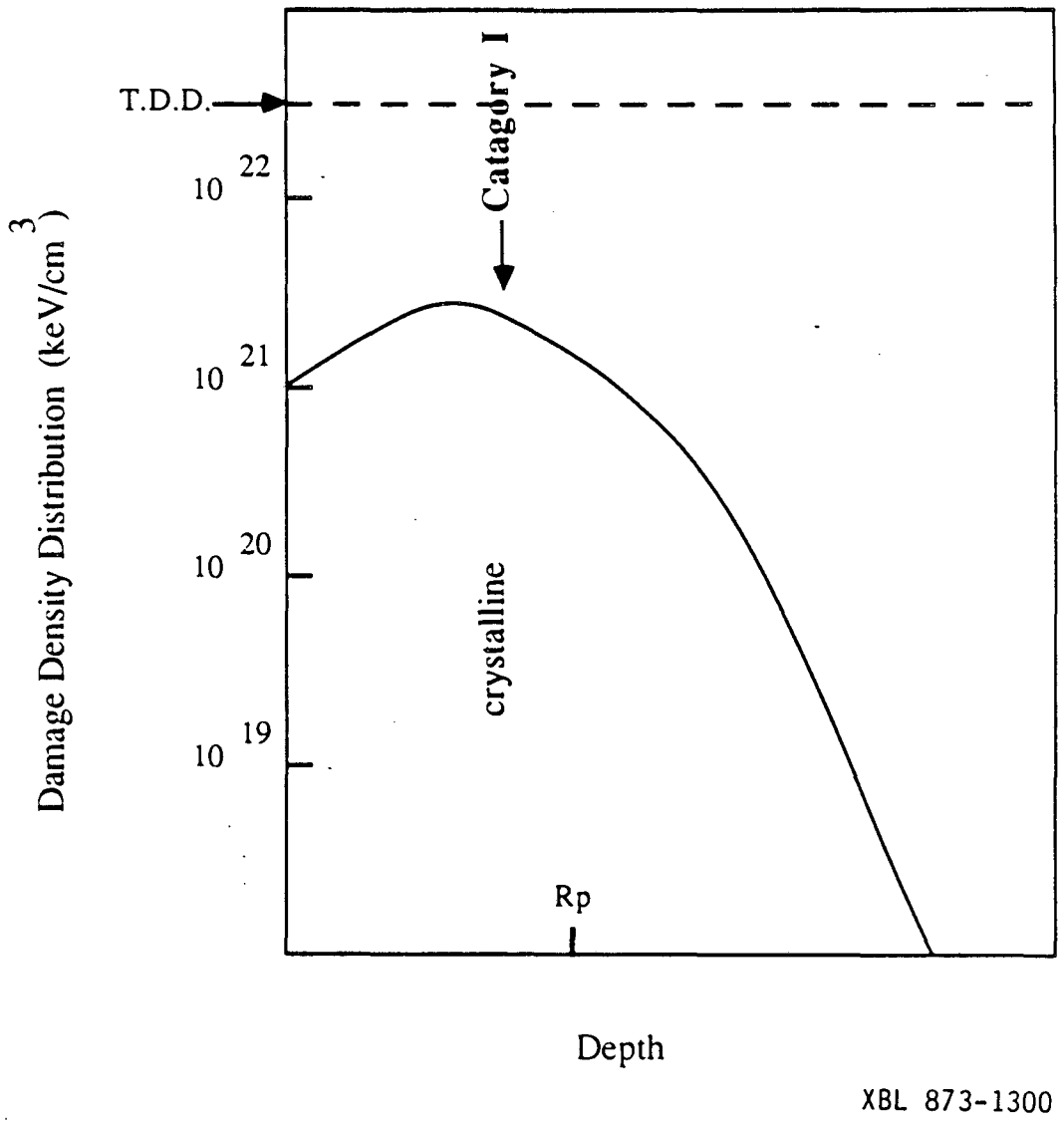

1. No Amorphous Layer Produced
2. Defect Concentration Increases With Dose

Catagory I Damage

Figure 5a

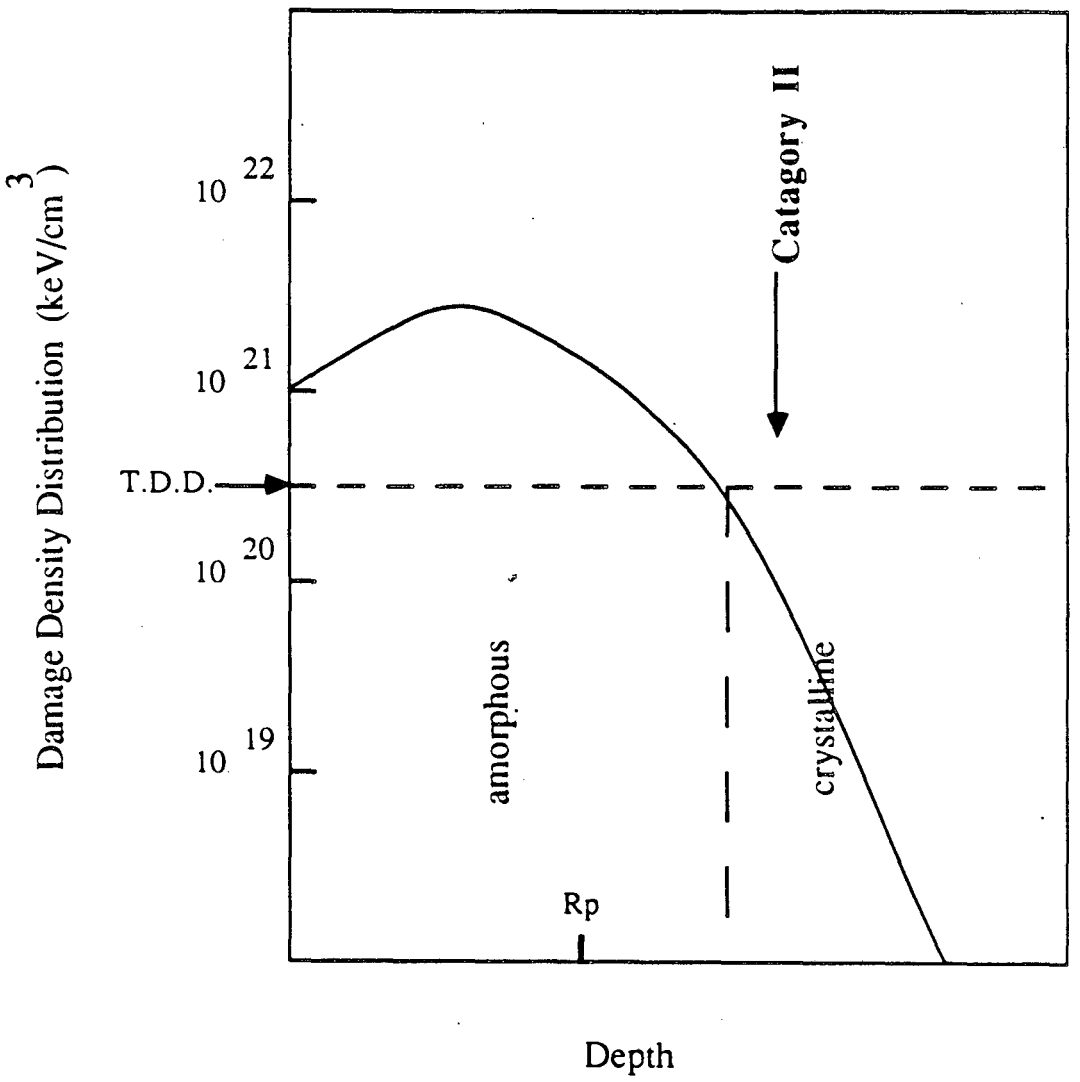

XBL 873-1301

1. Surface Amorphous Layer
2. Single Layer of Defects,
   not a strong function of dose

Catagory II Damage

Figure 5b

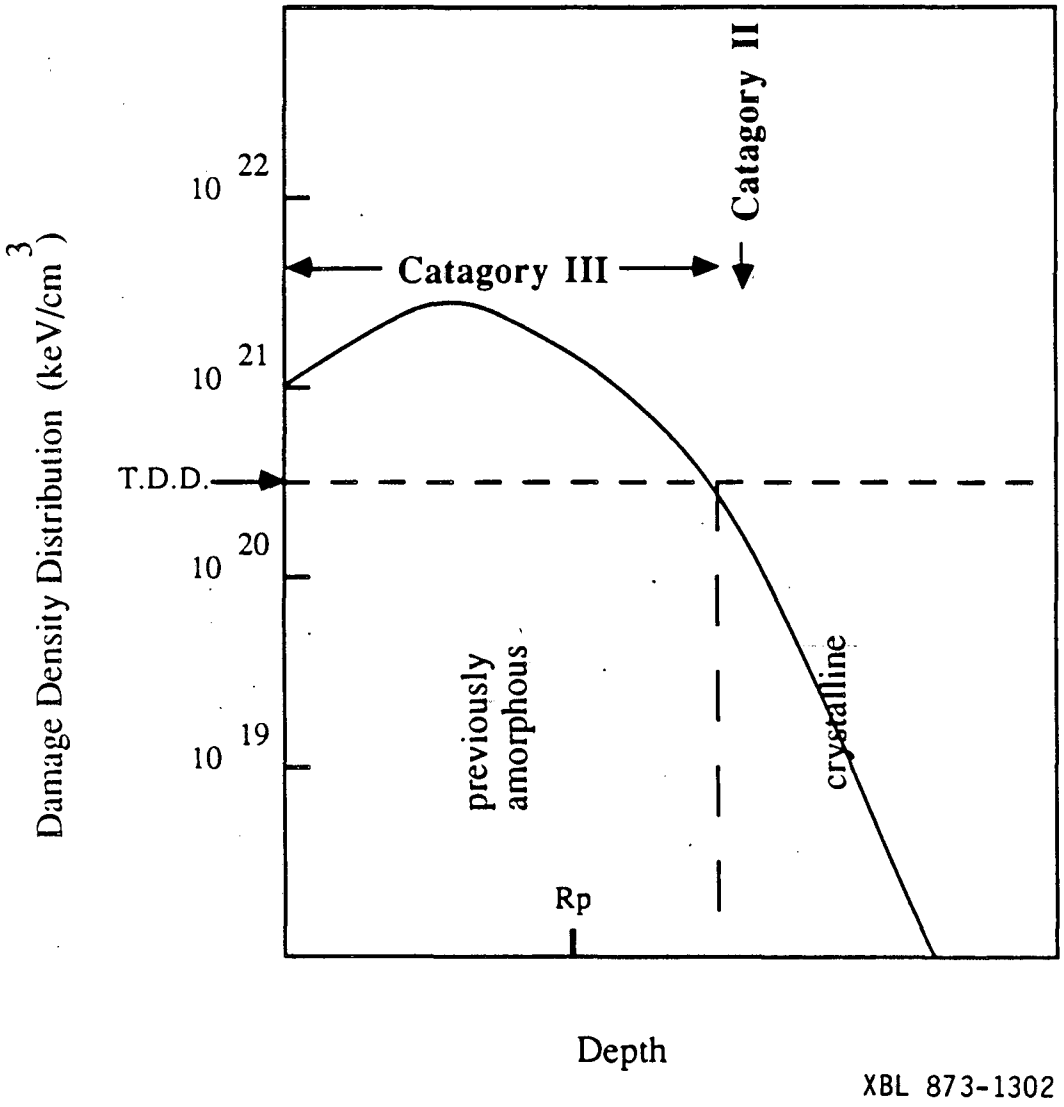

1. Regrown amorphous Layer
2. Poor Quality a/c Interface or {111} Wafers

Catagory II and Possibly Catagory III Damage

Figure 5c

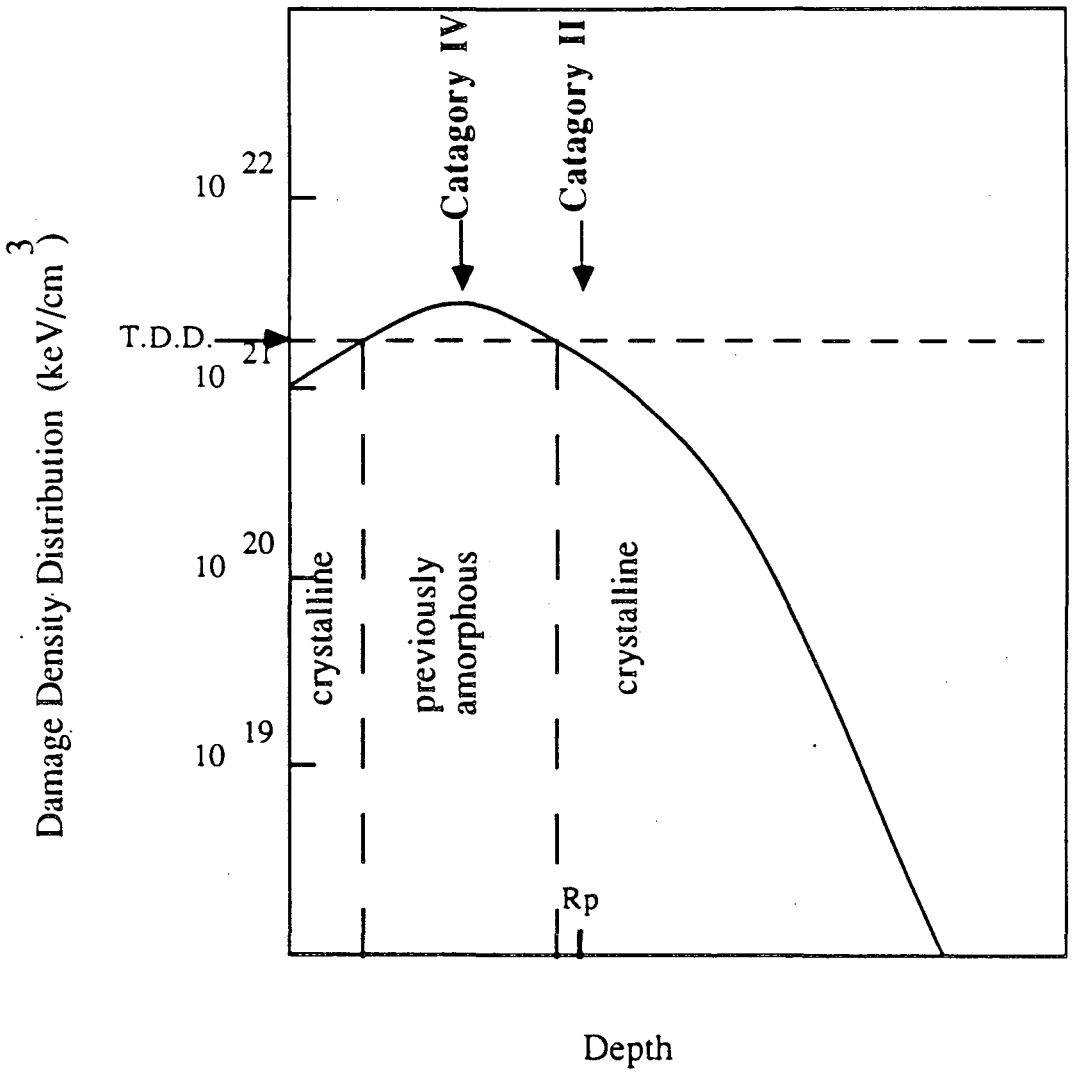

XBL 873-1303

1. Regrown Buried Amorphous Layer
2. Double Layer of Defects

Catagory II and IV Damage

Figure 5d

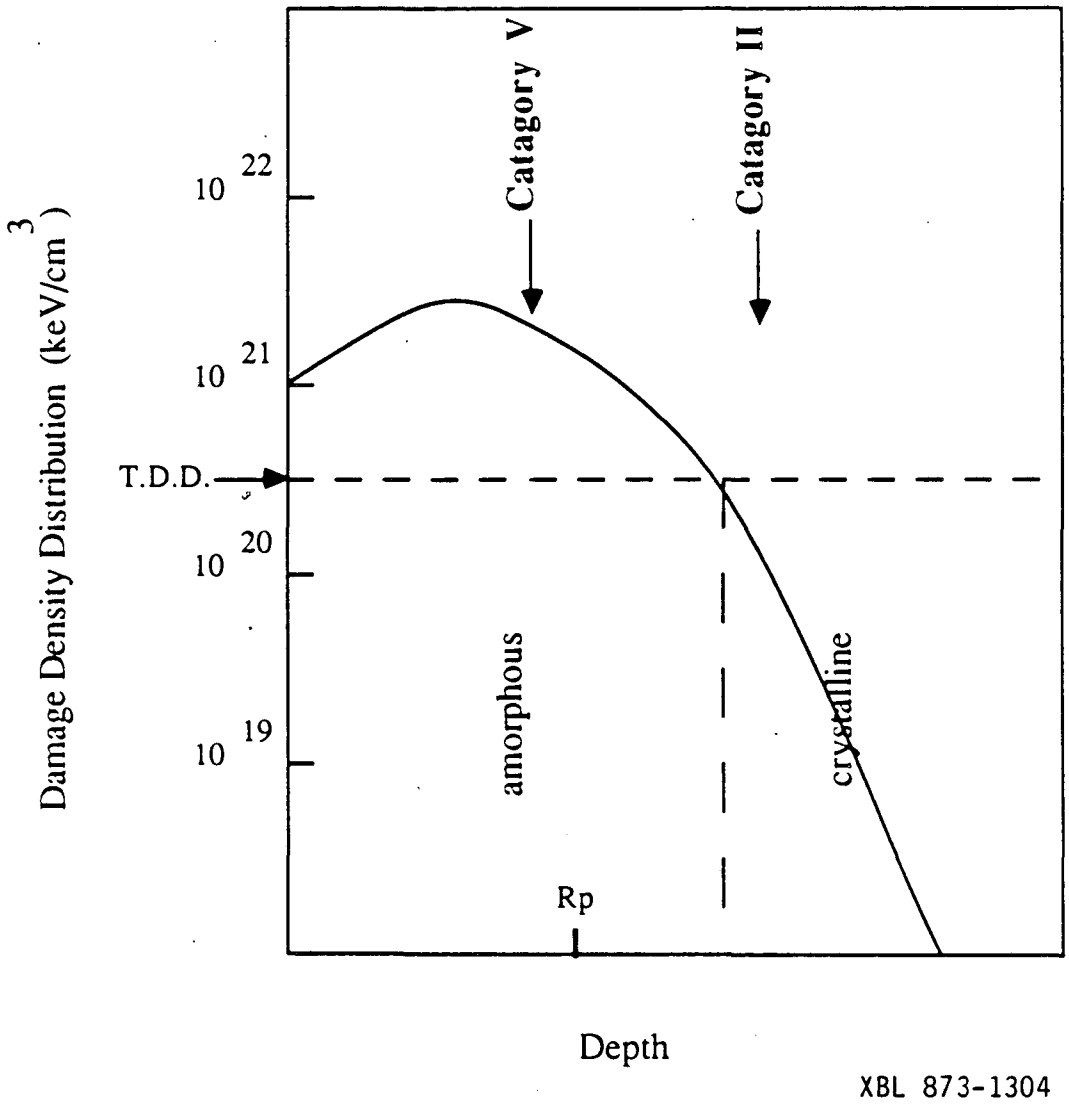

1. Exceed Solid Solubility
2. Precipitation

Catagory II and Possibly Catagory V Damage

Figure 5e

4. EXPERIMENTAL RESULTS

4.1 Category I Damage

Category I damage forms when the implantation damage is insufficient to produce an amorphous layer. Extended defects or dislocation loops will result if the dose or peak concentration is above a critical value. As shown in figure 5a, the category I defects form at a depth corresponding approximately to the peak of the impurity distribution (R_p). In addition, extended defects will be shown to form only if the dose exceeds a critical concentration. The evolution from a supersaturation of point defects to a layer of perfect dislocation loops as a function of annealing treatment has been extensively studied. The following model, proposed by Tan[109-111] is the result of numerous published observations.

The point defects left over after recombination of vacancies and interstitials will be dominantly interstitial clusters due to the nonconservative nature of the implantation process. These point defects coalesce into what have been termed intermediate defect configurations (IDC's). These initial damage clusters were estimated to be ~20Å in size.[112] IDC's include rod-like defects as well as {113} stacking faults.[113,109] They are predicted by clustering arrangements which minimize the number of dangling bonds and have been observed by high resolution TEM.[114] In addition, numerous high voltage TEM experiments at 400°C to 700°C have reported IDC formation in unimplanted silicon and germanium due to damage from the electron beam.[115-119] Upon annealing B and Ne implanted Si (<700°C) rod-like defects have been observed to grow.[120,121,123] HRTEM studies indicate they lie on (113) or (001) planes and have displacement vectors of ~a/4[116] or a/4[001] respectively.[115] They were also shown to be extrinsic. These rod-like defects are unstable and will dissolve at annealing temperatures above 700°C. Wu et. al.[120] showed the shrinkage of the defects to be controlled by the diffusivity of boron, implying that they contain boron. The activation energy for their shrinkage was determined to be ~3.5 eV. During the shrinkage of the rod-like defects, nearby extrinsic, faulted

dislocation loops were observed to grow.[120,124] After the rod-like defects dissolved, the category I defects remaining consist of faulted dislocation dipoles and loops. These faulted loops and dipoles are observed to unfault,[120,125] by 900°C, through the nucleation of a partial dislocation. The resulting perfect dislocation loops[126-128] are on {111} habit planes, elongated in the [110] directions and have a/2[110] type Burgers vectors perpendicular to the long axis of the loops. Extensive studies[84] of these elongated perfect dislocation loops indicate the Burgers vector evolves through a sequence from; a<100> to a/6<411> to a/3<111> to a/2<110>. The evolutionary steps involve the nucleation of specific Shockley partial dislocations.

All of these changes in the defect morphology upon annealing may be the cause of the reverse annealing observed with respect to the electrical activation of the implanted boron.[128,129] During reverse annealing below 900°C, the free carrier concentration was observed first to increase, then to decrease and finally to increase again, with increasing anneal temperatures. Reverse annealing does not occur when an amorphous layer is formed either prior to implantation with boron by preamorphization with silicon, or simultaneously by using BF_2 implants.[128-130]

The total concentration of atoms bound by these elongated extrinsic dislocation loops was shown to be approximately equal to the dose.[69,126] At high doses, above 2 x $10^{15}/cm^2$, the density of dislocation loops is sufficient to result in network formation, upon annealing, via dislocation-dislocation interaction.[123,126,127] At lower doses, the category I loops are quite stable and difficult to dissolve even at 1100°C.[126] The network structure was also quite stable.

Our results confirm several previously reported findings for the elongated perfect dislocation loops. Figure 6 shows the loops located at a depth centered near R_p (the projected range). The loops are on {111} planes, elongated in the [110] directions with

Burgers vectors perpendicular to the long axis of the loops. This is illustrated in figure 7, where the three fold and four fold symmetry of the {111} and {100} oriented wafers is apparent. The dependence of the concentration of category I defects on the implant dose can be seen in the micrographs in figure 8 and is also shown in the graph in figure 9.

Figure 10 also illustrates a concept which has not been discussed quantitatively in the literature. There is a critical dose (or more specifically a critical peak concentration) which must be exceeded in order to form extended defects such as dislocation loops. For doses below $2 \times 10^{14}/cm^2$ no dislocation loops were observed. This corresponds to a critical peak concentration of $\sim 1.6 \times 10^{19}/cm^3$. This critical concentration is shown in figure 10 to be independent of the species and wafer orientation. The observation that species with different peak values for the damage density distribution (33 eV/Å for 100 keV Al and 10eV/Å for 50 keV B) have the same dose requirements for producing category I damage implies that the quantity of atoms is more critical than the damage introduced in determining if extended defects will form, within the implantation energy co...nes of these experiments (<200 keV). This supports the model that the higher density of the silicon lattice due to the non-conservative nature of the implantation process is primarily responsible for category I defects.

During room temperature implantation of heavier ions such as antimony, at energies below 200 keV, the peak of the damage density distribution exceeds the effective threshold damage density when the dose is $\sim 5 \times 10^{13}/cm^2$. At these implant energies the peak of the impurity concentration is below the critical concentration necessary for category I formation. Antimony implants at 190 keV did not form any dislocation loops at a dose of $2 \times 10^{13}/cm^2$ (figure 11), where the peak of the damage density distribution was below the effective threshold damage density, (no amorphous layer formation) and the peak concentration is less than the critical concentration for category I extended defect formation. Upon increasing the dose to $5 \times 10^{13}/cm^2$, an amorphous layer forms and category II and IV

damage is produced prior to exceeding the critical peak concentration necessary for category I defect formation. Thus, it is not possible to produce category I extended defects by room temperature (or lower temperature) implantation with heavier ions such as antimony.

A possible model for category I extended defects formation is: above a critical concentration the extra atoms introduced into the lattice by implantation will ultimately result in the formation of extrinsic perfect dislocation loops upon 900°C annealing, as this is the preferred way energetically of accomodating the increased lattice density. This model accounts for the strong dependence of category I defects on dose as well as their independence of orientation. In addition, if the concentration of atoms bound by the extrinsic dislocation loops exceeds the concentration of atoms in a mono-layer of the {111} plane of silicon (~$1.4 \times 10^{15}/cm^2$), then dislocation network formation becomes possible upon annealing via dislocation-dislocation interactions.

Figure 6

30 keV ^{11}B 2 x $10^{15}/cm^2$, {100}, Annealed 900°C 30 minutes
Cross-Sectional TEM, Bright Field g_{220}

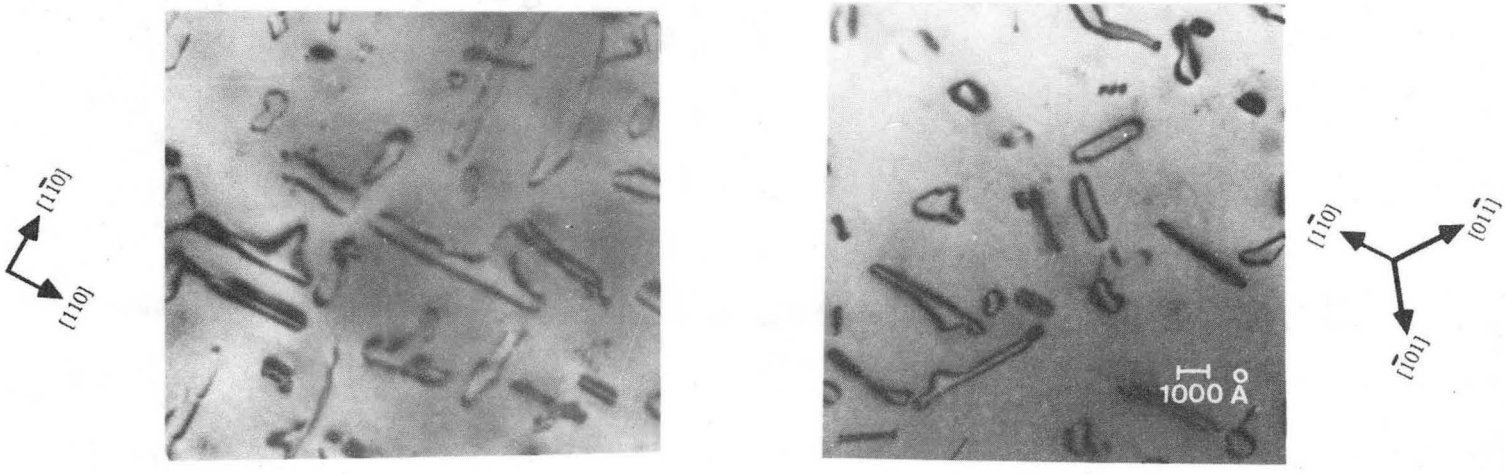

{100} **{111}**

XBB 873-2364

Figure 7

50 keV ^{11}B 5 x $10^{14}/cm^2$, Annealed 900°C 30 Minutes
Plan-View TEM, Bright Field g_{220}

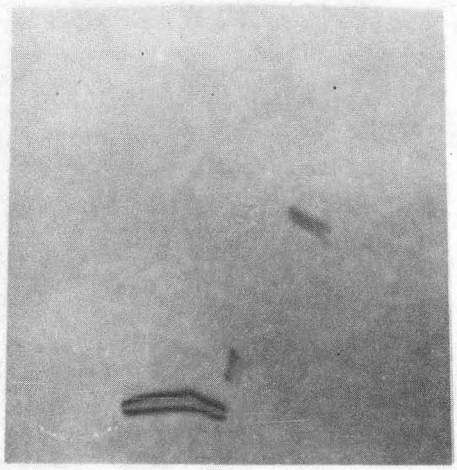

$2 \times 10^{14}/cm^2$

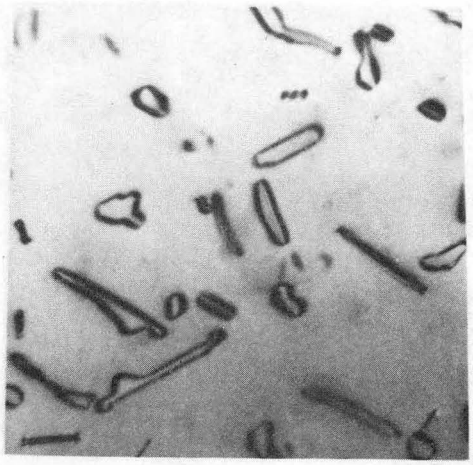

$5 \times 10^{14}/cm^2$

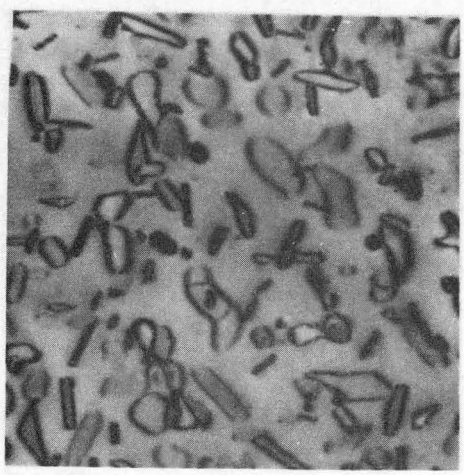

$1 \times 10^{15}/cm^2$

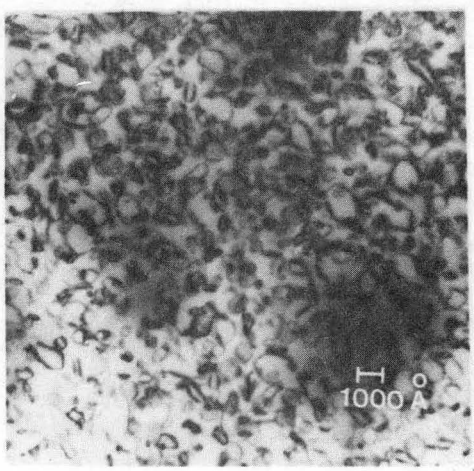

$2 \times 10^{15}/cm^2$

XBB 873-2365

Figure 8

50 keV ^{11}B, {111}, Annealed 900°C 30 Minutes
Plan-View TEM, Bright Field g_{220}

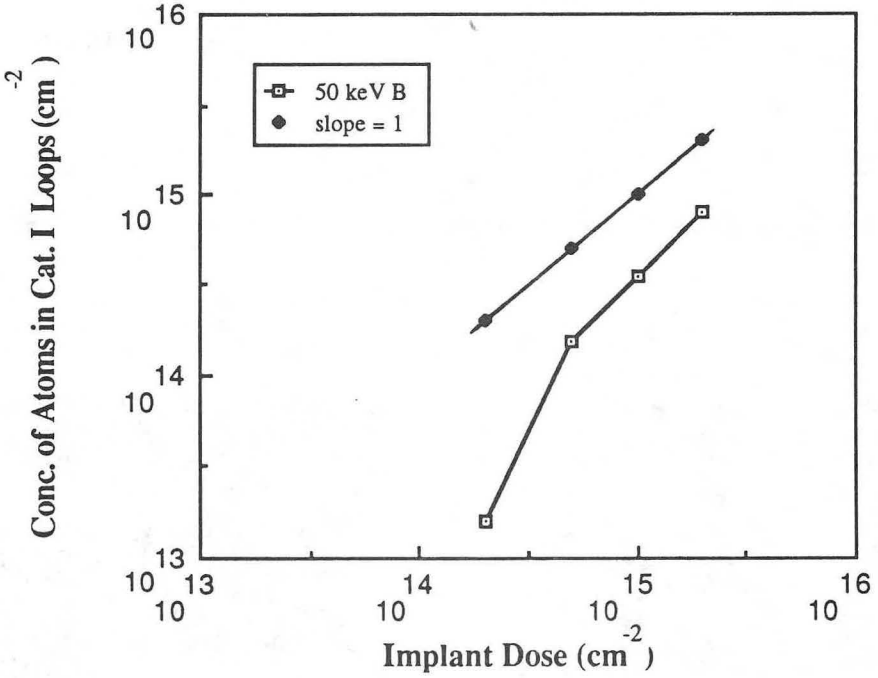

XBL 873-1305

Figure 9

50 keV ^{11}B, {111}
Annealed 900°C, 30 minutes

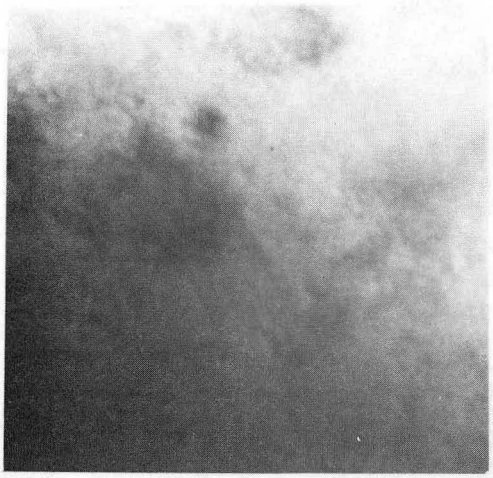

50 keV ^{11}B, 1 x $10^{14}/cm^2$
{111}

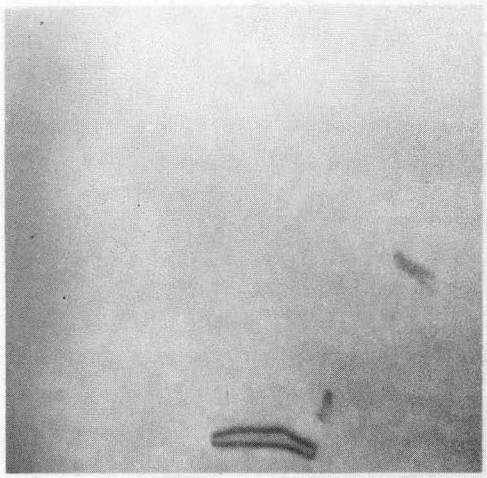

50 keV ^{11}B, 2 x $10^{14}/cm^2$
{111}

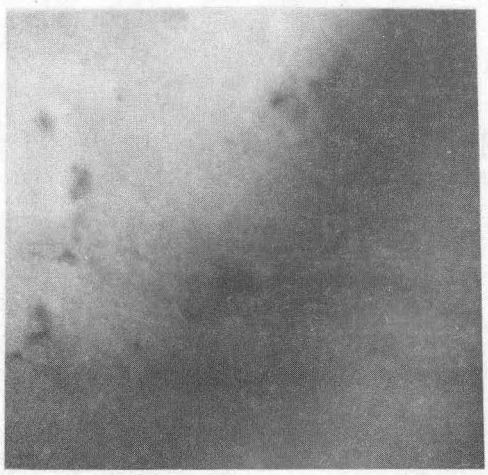

190 keV ^{11}B, 1 x $10^{14}/cm^2$
{100}

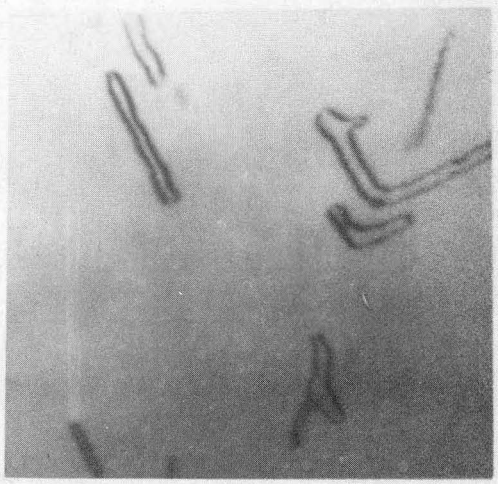

190 keV ^{11}B, 2 x $10^{14}/cm^2$
{100}

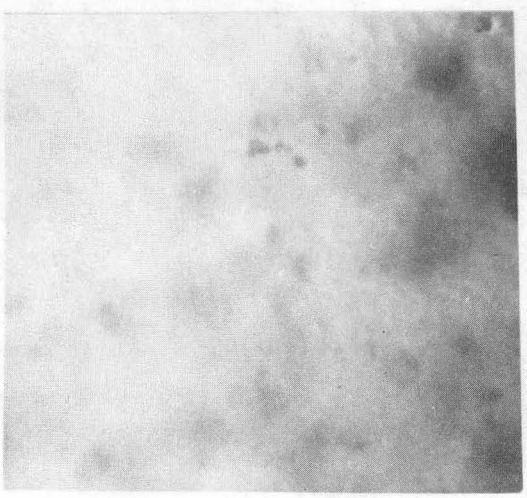

100 keV ^{27}Al, 1 x $10^{14}/cm^2$
{100}

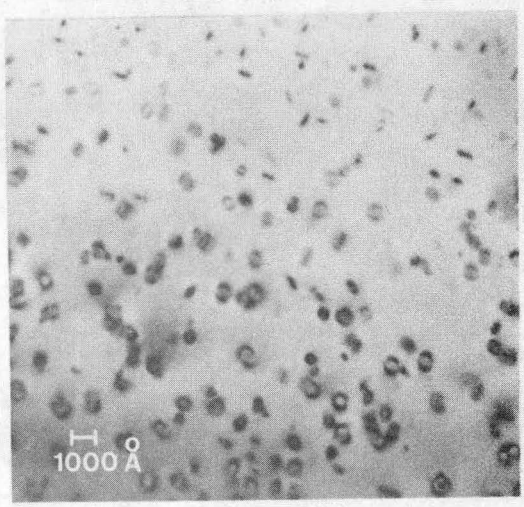

100 keV ^{27}Al, 2 x $10^{14}/cm^2$
{100}

XBB 873-2366

Figure 10

Annealed 900°C 30 minutes,
Plan-View TEM, Bright Field, g_{040}

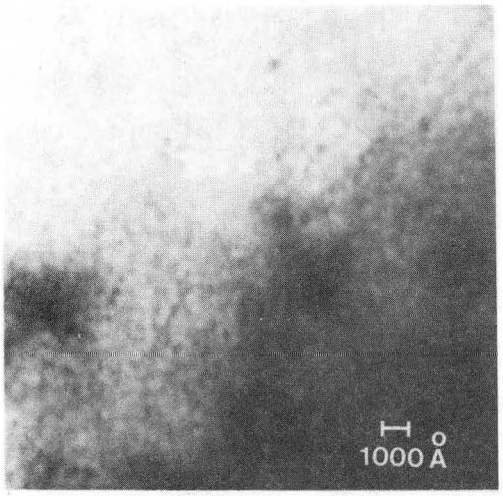

2 x 10^{13}/cm^2

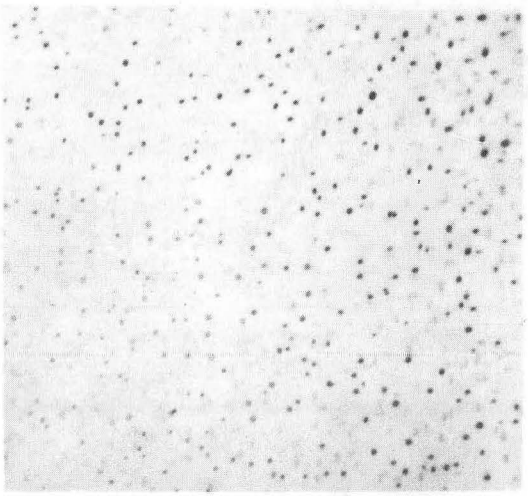

5 x 10^{13}/cm^2

XBB 873-2367

Figure 11

190 keV ^{122}Sb, {100}
Annealed 900°C, 30 minutes
Plan-view TEM, Bright Field, g_{040}

4.2 Category II Damage

Category II defects occur beyond the amorphous/crystalline interface in the crystalline material. The schematic in figure 5b shows the relationship between the damage density distribution and the effective damage density which results in a surface amorphous layer. The location of the category II defects is also indicated. It is important to stress that category II defects arise whenever an amorphous layer is formed by implantation. Category II defects do not form when category I defects are forming, probably because the category I defects act as sinks for the excess interstitials. It is possible to produce an amorphous layer and avoid formation of category III, IV and V defects by operating at the right implant energy, dose and temperature. However, category II defects cannot be avoided once an amorphous layer (buried or surface) is formed. This fact and the results from category I studies imply that implantation at room temperature of any of the group III, IV, or VA elements below 200 keV will, at the very least, result in the formation of either category I or category II extended (dislocation loops) defects upon annealing if the dose exceeds 1 x $10^{14}/cm^2$.

The category II defects evolve into extrinsic dislocation loops after regrowing the amorphous layer at 550°C and additional higher temperature annealing (i.e. 900°C, 30 minutes). The dislocation loops are typically 150 Å - 300Å in diameter making it possible to study them by diffraction or phase contrast in a transmission electron microscope.[131,132] After reviewing how the loops form, the following discussion will focus on why only extrinsic dislocation loops are observed for the category II defects, and the unusual dependence of defect concentration on mass and dose.

The category II region, after implantation, is supersaturated with interstitials or becomes so upon annealing. In addition to the observation of only extrinsic dislocation loops by TEM, it has been shown via X-ray studies[142] that two strain field regions exist for

a 8 x $10^{15}/cm^2$ As^+ implanted sample. The region occupied by the amorphous layer is negatively strained after annealing while the deeper, category II region is positively strained which may be due to the extra concentration of interstitials in this region. The formation of extrinsic dislocation loops in the category II region is energetically favorable to the formation of a large cluster of interstitials. This is attributed to the large reduction in strain energy associated with formation of a plate. This reduction in energy dominates the increase in energy associated with the larger surface area/volume ratio. There is still a strain field associated with the dislocation loop, therefore, it can behave as a gettering site for impurities and implanted dopants. Such segregation for implanted dopants (phosphorus[133] and arsenic[134]) has been observed by SIMS and mobility profile measurements as well as by EBIC studies.[135] Regrowth of the amorphous layer at <600°C indicates no dopant redistribution, thus the segregation to the category II loops, observed after higher temperature annealing, must result from diffusion of the impurity.[136] Additional evidence of extensive diffusion of the implanted dopant below the a/c interface implies that it is not unreasonable to expect such diffusion to occur. This gettering of implanted impurities has also been observed for flourine[134] from BF_2 implants and was used to investigate[35]. category II and category IV damage layer existence and location by ion microprobe mass analysis.[152] The detrimental aspects of such gettering include pipe diffusion and higher leakage currents if the defects occur near a p-n junction. Implantation through an oxide layer has been shown to result in "gettering" of recoiled oxygen atoms by the category II dislocation loops.[133,138,139] Such gettering can result in severe pinning of the dislocation loops which restricts the dissolution kinetics upon higher temperature annealing. Since one of the goals is to remove the damage with the least amount of concommitant impurity redistribution, such pinning is unwanted. It may be desirable if the damage is to be used as a gettering site due to its increased stability.

The evolution of category II damage from point defects to extrinsic dislocation loops upon annealing is believed to occur in a manner similar to that discussed for category I defects, that is via intermediate defect configurations such as {113} stacking faults.[109,140] By 900°C most of the category II dislocation loops are either faulted (a/3 [111]) or perfect (a/2[110]) on {111} planes as shown in figure 12 for a 100 keV, 1 x $10^{15}/cm^2$, Ga^+ implant after annealing at 900°C for 30 minutes. The dark spots are Ga precipitates which will be discussed in the chapter on category V defects. The high resolution TEM micrograph in figure 13 shows the faulted nature of this extrinsic dislocation loop.

The effect of implant dose, mass and wafer temperature on category II defects have been studied and several interesting trends have been observed. In order to study category II loops only, {100} wafers were used to avoid microtwins (category III) defects observed for {111} wafers. A Waycool endstation was used to avoid dynamic annealing which could lead to hairpin dislocations (category III) and buried amorphous layers (category IV defects). The heavier ions (Ge^+ and As^+) were implanted at 100 keV while the light ions were implanted at 50 keV. In order to produce a surface amorphous layer, the dose for the lighter ions had to be at least 1 x $10^{15}/cm^2$, while the heavier ion dose had to exceed 2 x $10^{14}/cm^2$. For the dopants (As, P) any dose of 5 x $10^{15}/cm^2$ or more produced a peak concentration above solid solubility at the 900°C annealing temperature. Thus only a narrow dose "window" could be studied for these species (especially phosphorus). Si^+ and Ge^+ implants were not under such solubility restrictions and will be emphasized below. In order to make the loops well defined for TEM study the samples were annealed at 900°C for 30 minutes in a dry nitrogen ambiant.

Figure 14 shows plan-view TEM micrographs illustrating the effect of dose and mass on the concentration of category II dislocation loops. The fact that only category II loops are formed is shown in the cross-sectional TEM micrographs in figure 15. The depth of the

amorphous/crystalline interface prior to annealing is indicated. To further illustrate the effect of dose and mass, the concentration of atoms bound by the extrinsic dislocation loops was estimated based on the density and average diameter of the loops. This is shown graphically in figure 16. The concentration of atoms bound by the dislocation loops increases dramatically for the heavier ions with increasing dose and to a lesser extent for the lighter ions. The large dose dependence of the category II damage is not predicted by the model[141] attributing the defects to the damage deposited into elastic collisions beyond the a/c interface. As seen in the schematic in figure 17, the area under the damage density distribution beyond the a/c interface does not, to a first order, increase with higher doses due to the increase in thickness of the amorphous layer. The region of interest is the tail region of the damage density distribution where the accuracy of the calculation is more questionable. Examination of the change in area beyond the a/c interface for heavier species such as Ge indicate their is actually a slight decrease (by a factor of 2) in the integrated damage density with an increase in dose from $1 \times 10^{14}/cm^2$ to $1 \times 10^{15}/cm^2$. Again this calculation is subject to the error in the damage density distribution still we believe that the amount of damage deposited beyond the a/c interface cannot explain the dramatic dose dependence of the category II defects for heavier species.

In addition, the amount of damage deposited into elastic collisions beyond the a/c interface is much greater for the Si^+ implants than the Ge^+ implants due to the higher effective threshold damage density for Si^+ implants as shown in figure 18. Our data could not confirm if the concentration of atoms bound by the loops is less for heavier ions than lighter ions, at lower doses. However, it was confirmed to be greater for Ge^+ implants than for Si^+ implants at higher doses which does not match the models predictions. Also, the association of the category II damage with just the damage created does not explain the extrinsic nature of the dislocation loops. These observations suggest that there must be an

alternative explanation for the category II loops other than simply the amount of damage deposited into elastic collisions.

4.2.1 Models for Defect Formation

One possible model,[141] developed to explain the extrinsic nature of the loops, suggests that category II loops form from the dissolution of amorphous islands beneath the a/c interface (inside the crystalline material). This model also suggests that the concentration of loops should be less for heavier ions due to the more abrupt a/c interface. As stated, this is not observed at higher doses. In addition, the model also predicts that the concentration of atoms bound by dislocation loops should decrease as the a/c interface becomes more abrupt with increasing dose. This is contrary to the observations in figure 14.

One possible model to explain the data is that the excess concentration of ions coming to rest beyond the a/c interface is one of two contributing sources for the category II dislocation loop formation. As with category I defects, the implanted ions result in an increased density in the crystal lattice thus, the dislocation loops should be extrinsic. From a purely statistical viewpoint, the category II loops should be composed primarily of Si_i. This can be reasoned from the fact that each implanted ion creates several hundred Frenkel pairs as it comes to rest. Beyond the a/c interface the number of Frenkel pairs generated is considerably less since much of the ion's energy is lost in the amorphous layer, however, there are still more Frenkel pairs than implanted ions (~10 to 100 times as many Frenkel pairs) in this region. There is a, relatively high, strain field associated with Group III, IV and VA interstitials in silicon,[56] so both dopant interstitials and silicon interstitials prefer occupying substitutional sites. After annealing and recombination of interstitials and vacancies, the chances are greatest that Si_i will remain. It is possible to calculate the concentration of implanted species coming to rest beyond the a/c interface ($Ø_2$) by

integrating the concentration profile from the a/c interface to infinity. For a gaussian distribution this can be calculated from:

$$\varnothing_2 = \varnothing/2 \text{ erfc } [(a/c - R_p) / (\sqrt{2}\, \Delta R_p)]$$

where Ø is the implant dose and x(a/c) is the depth of the amorphous/crystalline interface. It was possible to generate the graph in figure 19 by using the actual values for the a/c interface, as measured by cross-section TEM, for different doses. Comparison with figure 16 shows that this effect matches, quantitatively, quite well for the lighter ions and may dominate for Si^+ implants. Though, it may contribute to the total concentration observed for heavier ions, this effect cannot account for the increase associated with increasing dose. For heavier ions, we propose that a second factor may dominate at higher doses. This second contribution arises from energy deposited into nuclear collisions within the amorphous layer. Figure 20 shows that the integrated area of the damage density distribution curve within the amorphous layer is greater for Ge than Si implants and increases at a rate approximately proportional to the dose as predicted by basic implantation damage theory. This qualitatively matches the dose dependence for the concentration of atoms bound by dislocation loops for Ge. The manner in which these elastic collisions may contribute to the total concentration of atoms in the loops may be via the creation of free atoms within the amorphous layer which either recoil or possibly diffuse through the a/c interface to the category II region. One method used to test this model is via pre- and post-amorphization studies.

Preamorphization[143-145] is most commonly used as a means of preventing the deep channeling tails associated with random channeling of lighter ions such as boron.[146] The surface is usually preamorphized with a high dose, high energy Si^+ implant into which a

second, lower energy, implant is done with the lighter ion. Regrowth of a preamorphized layer implanted with boron results in electrical activation of the boron,[147] avoids the problem of reverse annealing[128] and reduces the leakage current. The problem with preamorphizing with Si^+ is the increased likelihood of category III (hairpin) dislocation formation. This is associated with the less abrupt a/c interface for higher energy Si^+ implants,[148] which can be avoided by preamorphizing with Ge^+ instead of Si^+ as the a/c interface is more abrupt.

In addition to its technological importance, pre-amorphization was used to study the effect of implant species on the defect annealing kinetics by, "in theory" normalizing the initial category II dislocation loop concentration. This "normalization", however, did not occur. The category II concentration increased if the preamorphized layer was implanted with a second lower energy species. This may be understood from the model suggested above, that recoiled or diffusing free atoms from the amorphous layer can contribute to the concentration of atoms within the category II dislocation loops. A series of experiments was conducted involving the implantation of Si^+ at different energies into the same sample. Figure 21 shows plan-view and cross-sectional TEM micrographs of a sample implanted with a 70 keV 5 x $10^{15}/cm^2$ Si^+ implant followed by a second 30 keV, 5 x $10^{15}/cm^2$, Si^+ implant. After regrowth of the amorphous layer at 550°C the sample was annealed at 900°C for 16 hours. When compared with a single 50 keV 1 x $10^{16}/cm^2$ Si^+ implant the concentration of atoms bound by dislocation loops, after annealing, for the preamorphized sample is observed to be greater than for the singly implanted sample. For the preamorphized sample, the concentration of atoms within the dislocation loops was sufficient to result in network formation via dislocation-dislocation interaction, as discussed in the category I damage section. If the order of the implants is reversed (also in figure 21) then the concentration of atoms bound by the loops is reduced such that it is insufficient for

network formation. This directly supports our suggestion that recoil or diffusion of atoms created during implantation of a preamorphized layer can result in increased category II damage.

The increased concentration of atoms in category II dislocation loops from implantation of a pre-amorphized surface can be detrimental to the dissolution of such damage. When the concentration of atoms within the loops is increased, as shown in figure 22, incomplete dissolution of all of the dislocation loops can result.

The wafer temperature influences the concentration of atoms within the category II loops. Published results indicate that reducing the implant temperature reduces the effective threshold damage density and, for all models for category II defect formation this should result in less category II damage.[64,149,150] It has also been suggested that the effective threshold damage density is independent of ion mass (5-6 x 10^{20}keV/cm^3)[151,51] at 77K or less, where self annealing and point defect migration processes are inhibited. For the model we proposed, decreasing the effective threshold damage density would reduce the concentration of atoms coming to rest beyond the a/c interface by increasing the thickness of the amorphous layer without affecting the final implanted ion distribution. A thicker amorphous layer would also mean fewer recoiled or diffusing free atoms could reach the category II region which would also reduce the concentration of atoms within the category II dislocation loops.

Figure 23 shows the comparison of a 100 keV 1 x 10^{15}/cm^2 P^+ implant and a 200 keV 4 x 10^{14}/cm^2 As^+ implant performed at 300K and 77K. The concentration of atoms within the category II loops decreases significantly with decreasing wafer implant temperature as predicted. Narayan et. al.[51] showed that the effective threshold damage density reaches a constant below 77K and does not continue to decrease. Thus, no further decrease in the concentration of category II damage would be expected at implant temperatures below 77K.

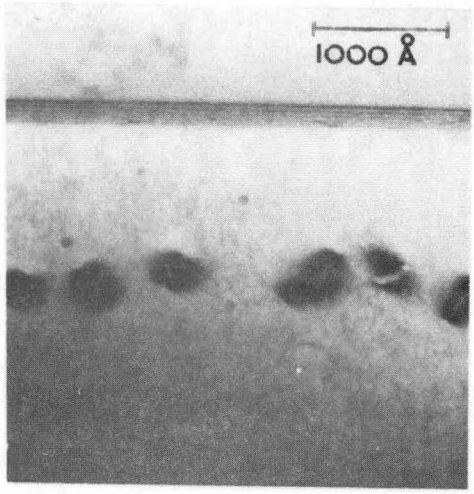

Figure 12

100 keV ^{70}Ga 1 x 10^{15}/cm^2, {100}, Annealed 900°C 2 hours
Cross-sectional TEM, Bright Field, g_{220}

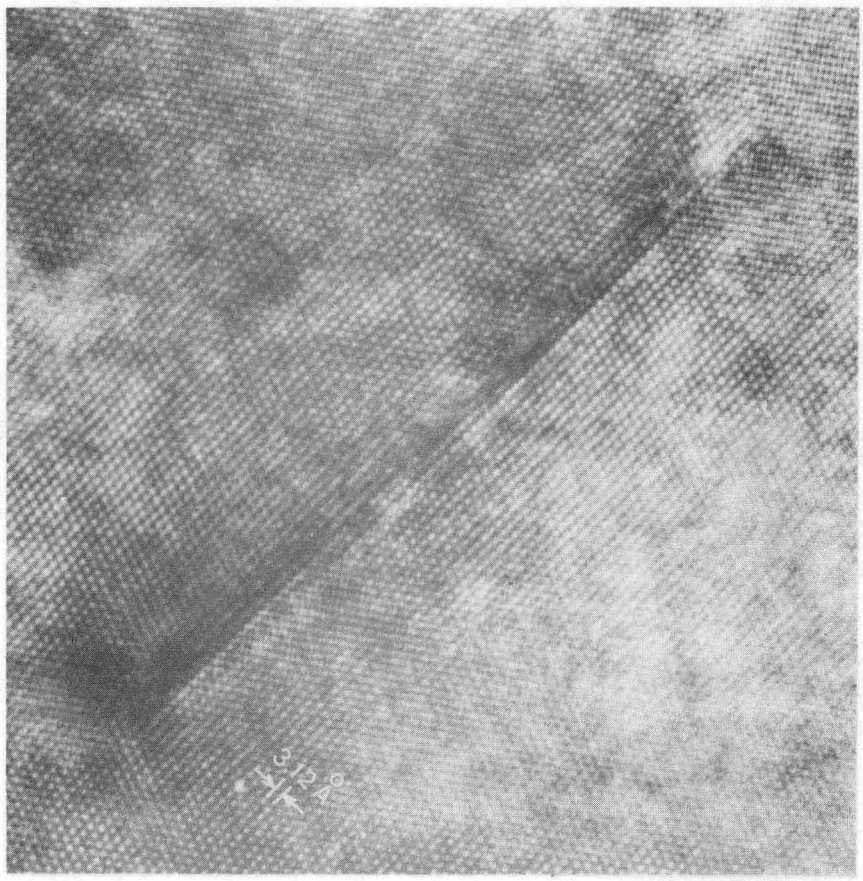

XBB 873-2368

Figure 13

100 keV ^{70}Ga 1 x 10^{15}/cm^2, {100}, Annealed 900°C 2 hours
High Resolution TEM, Bright Field multibeam condition.

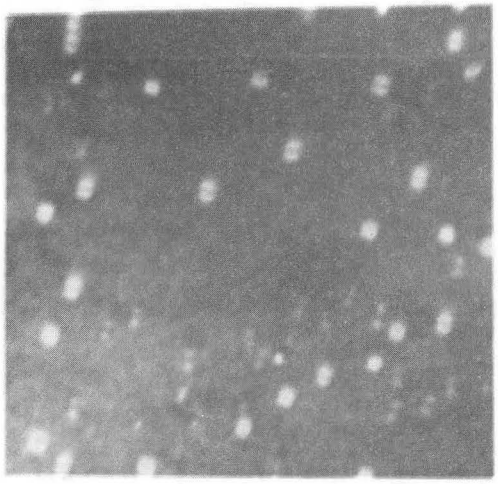

100 keV ^{72}Ge 2 x $10^{14}/cm^2$

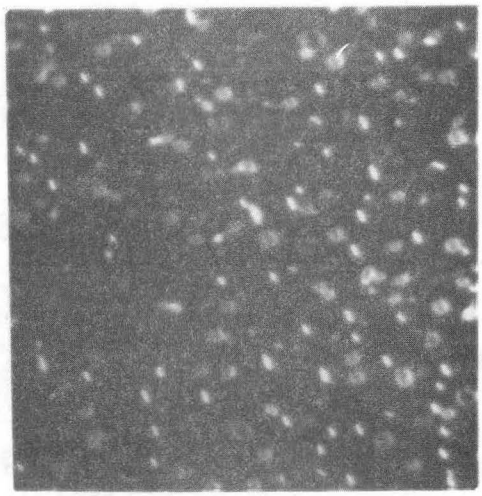

50 keV ^{28}Si, 1 x $10^{15}/cm^2$

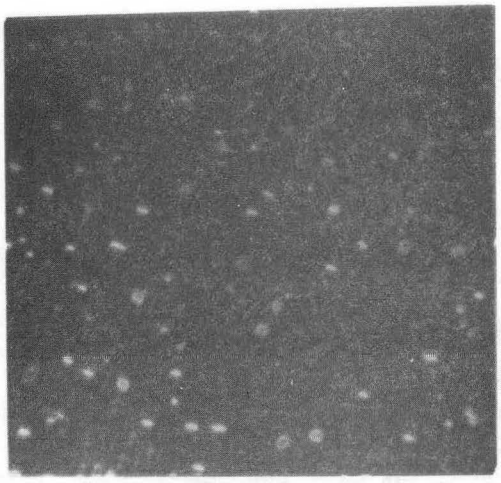

100 keV ^{72}Ge 1 x $10^{15}/cm^2$

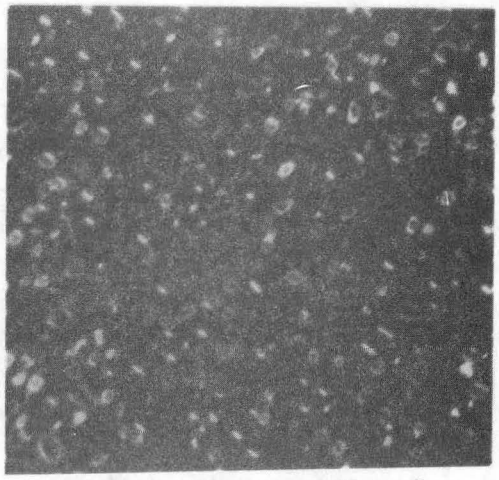

50 keV ^{28}Si, 5 x $10^{15}/cm^2$

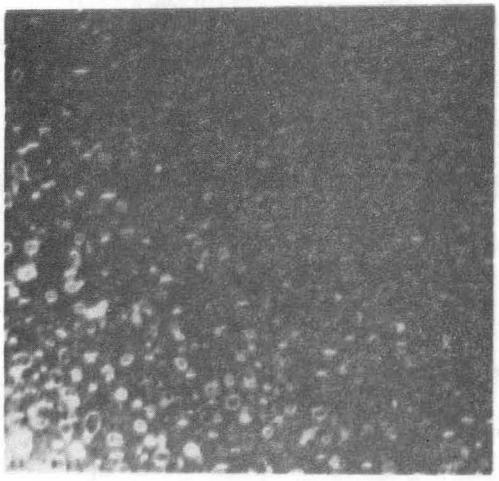

100 keV ^{72}Ge 1 x $10^{16}/cm^2$

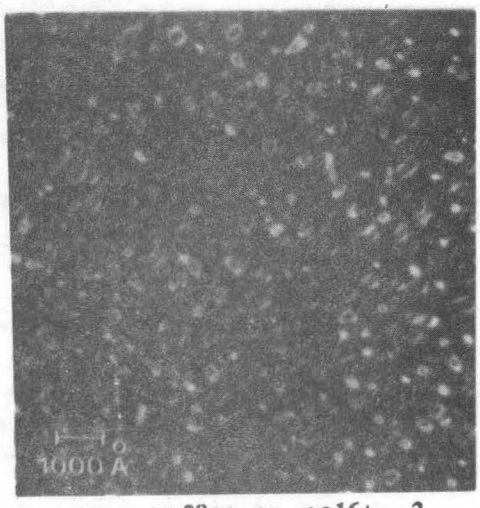

50 keV ^{28}Si, 1 x $10^{16}/cm^2$

XBB 873-2369

Figure 14

{100}, Annealed 900°C, 30 Minutes
Plan-view TEM, Centered Dark Field, g_{220}

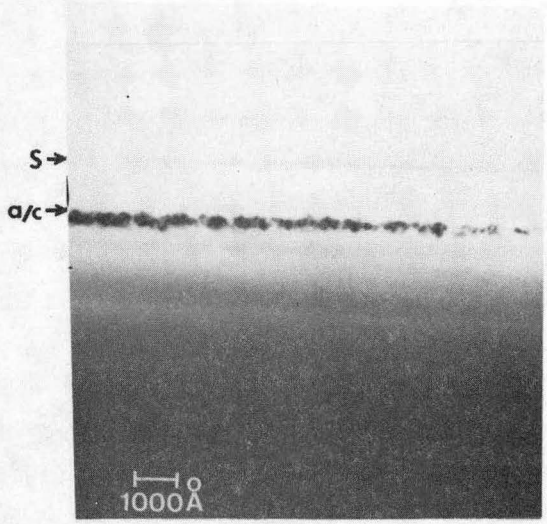

Figure 15a

100 keV ^{72}Ge, 1 x 10^{16}/cm^2
Annealed 900°C 60 Minutes, Bright Field, g_{220}

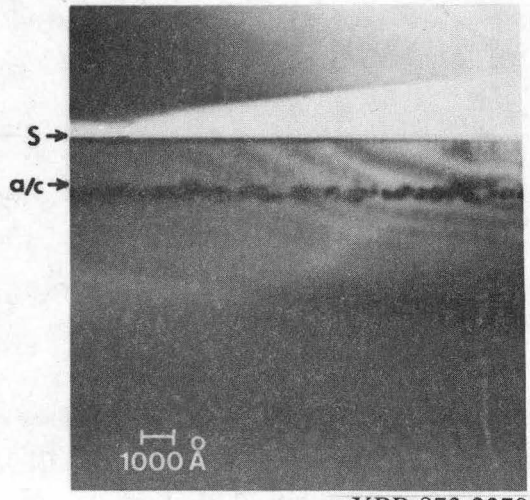

XBB 873-2370

Figure 15b

50 keV ^{28}Si 1 x 10^{16}/cm^2, {100}
Annealed 900°C 30 Minutes, Bright Field, g_{220}

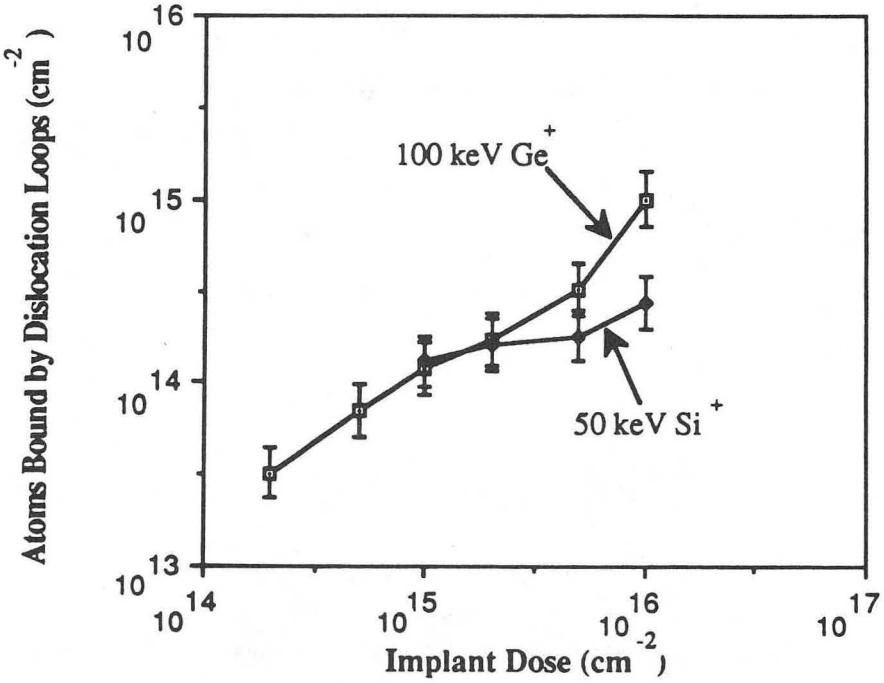

XBL 873-1306

Figure 16

Concentration of Atoms Bound by Catagory II Dislocation Loops as a Function of Dose.

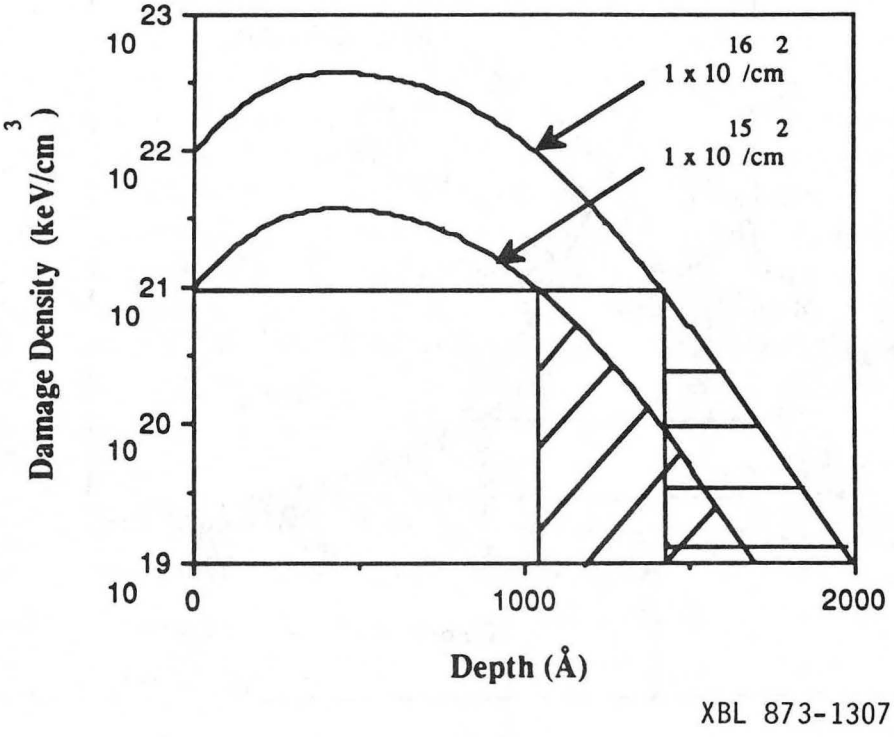

Figure 17

Damage Density Distribution for Two Different Implant Doses

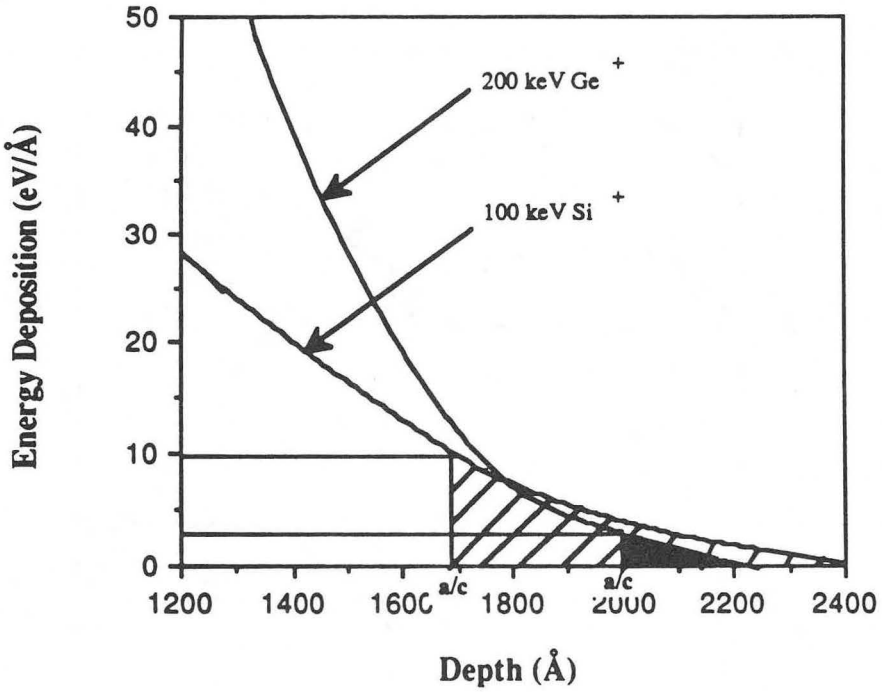

XBL 873-1308

Figure 18

Energy Deposited into Elastic Collisions Beyond the Amorphous Layer for Two Ions with Different Effective Threshold Damage Densities

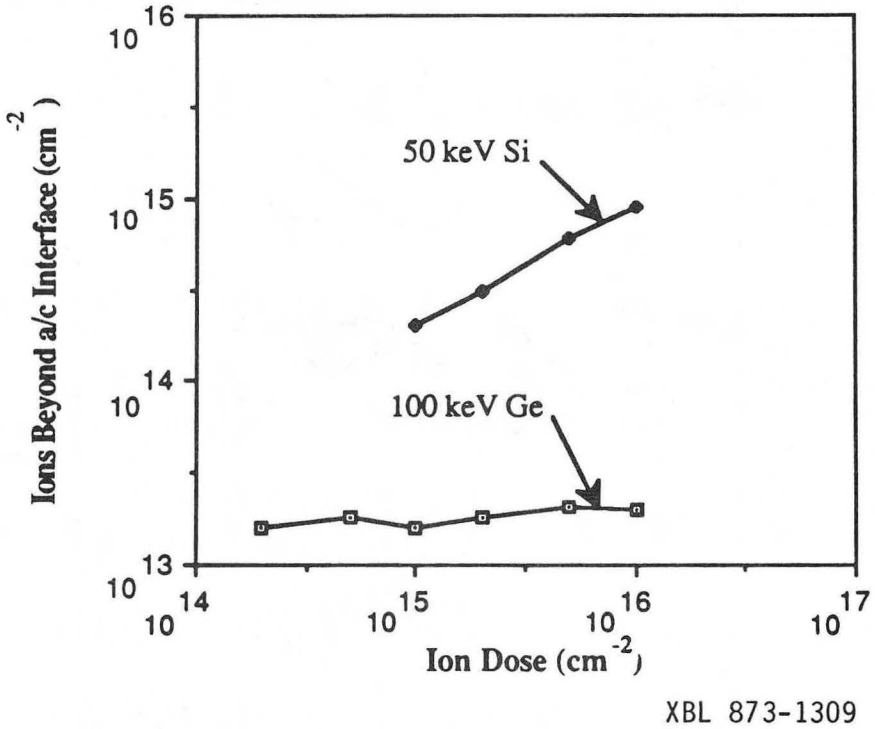

Figure 19

Ion Concentration Beyond Experimentally Measured Amorphous/Crystalline Interface Depth as a Function of Ion Dose.

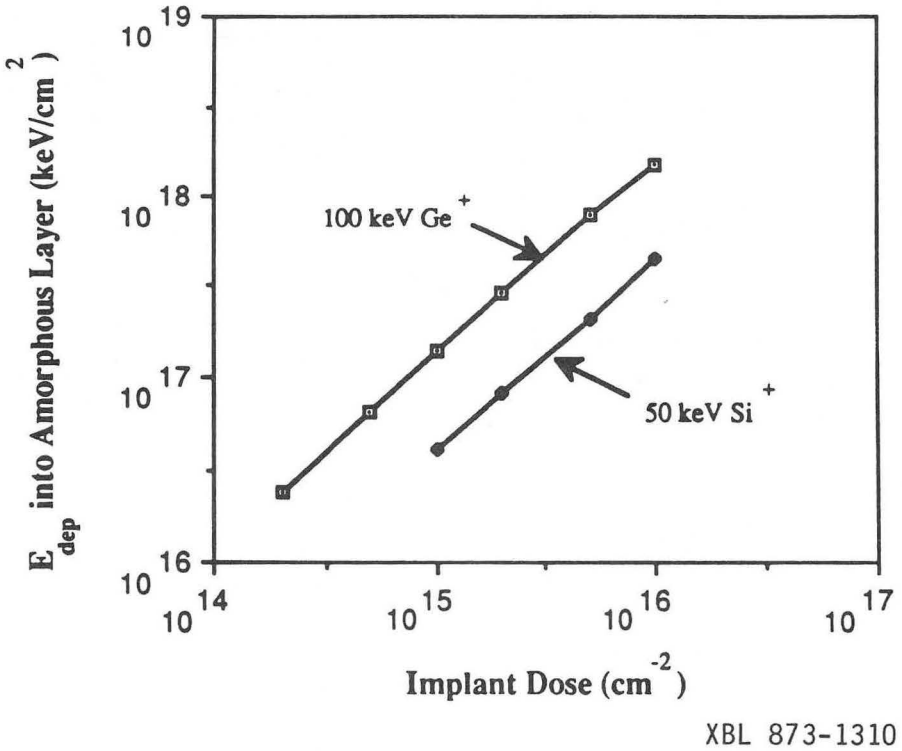

XBL 873-1310

Figure 20

Energy Deposited via Elastic Collisions into the Amorphous Layer as a Function of Ion Dose

PTEM, Bright Field, g_{040}

XTEM, Bright Field, g_{220}

70 keV ^{28}Si 5 x $10^{15}/cm^2$ + 30 keV ^{28}Si 5 x $10^{15}/cm^2$

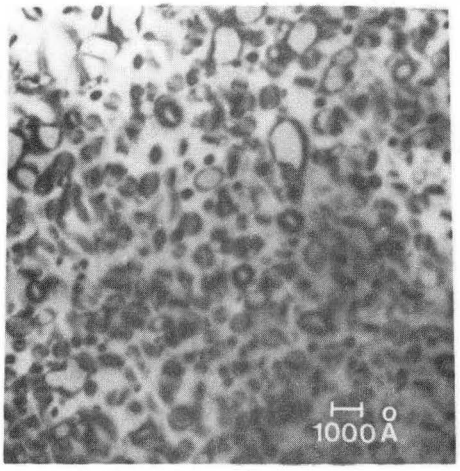

PTEM, Bright Field, g_{040}

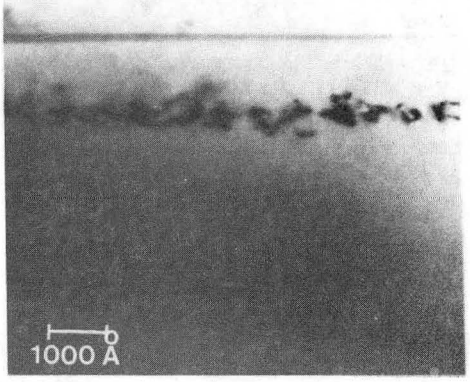

XTEM, Bright Field, g_{220}

30 keV ^{28}Si 5 x $10^{15}/cm^2$ + 70 keV ^{28}Si 5 x $10^{15}/cm^2$

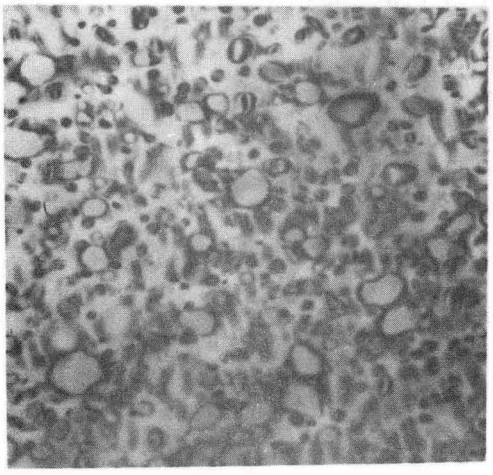

Bright Field, g_{040}

Bright Field, g_{220}

50 keV ^{28}Si 1 x $10^{16}/cm^2$

XBB 873-2371

Figure 21

All Samples Annealed at 900°C for 16 hours

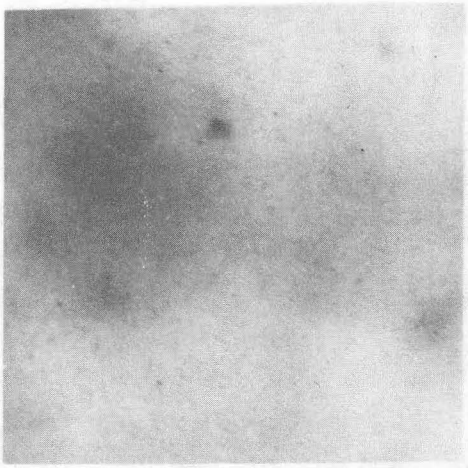

50 keV ^{31}P 1 x $10^{16}/cm^2$
into
{100} unimplanted silicon

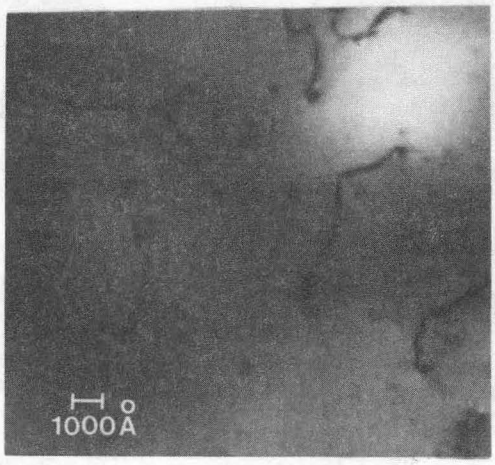

55 keV ^{31}P 1 x $10^{16}/cm^2$
into
{100} silicon preamorphized with
70 keV ^{28}Si 5 x $10^{15}/cm^2$ + 30keV ^{28}Si 5 x $10^{15}/cm^2$

XBB 873-2372

Figure 22

Annealed 900°C 4 hours, Bright Field, g_{040}

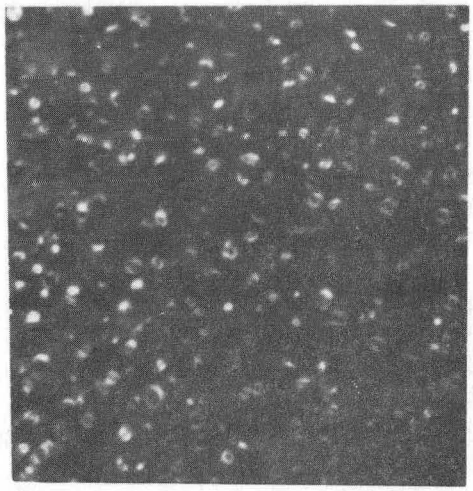

Waycool Endstation (300K)

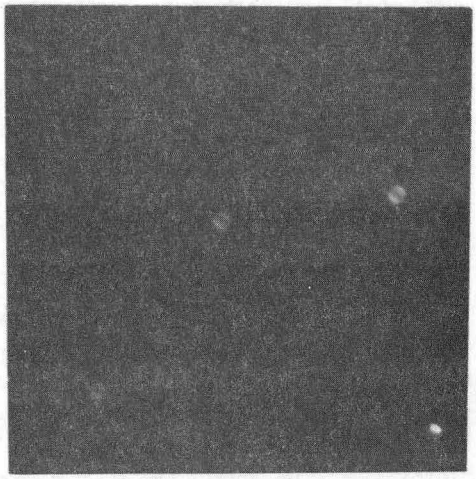

Liquid Nitrogen Implant (77K)

100 keV ^{31}P 1 x $10^{15}/cm^2$

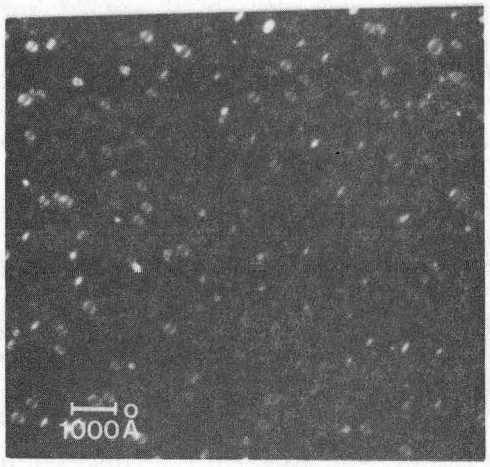

Waycool Endstation (300K)

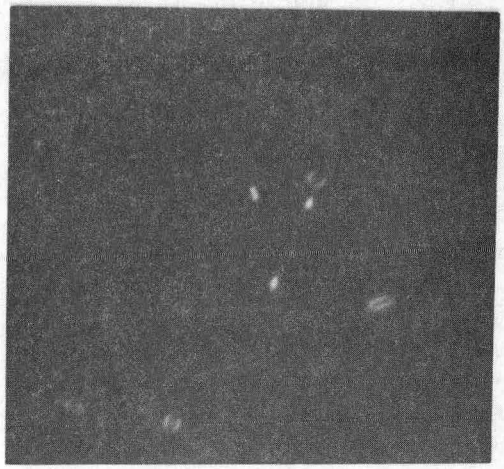

Liquid Nitrogen Implant (77K)

200 keV ^{75}As 4 x $10^{14}/cm^2$

XBB 873-2373

Figure 23

{100}, Annealed 900°C 30 minutes
Centered Dark Field, g_{220}

4.3 Category III Damage

Category III defects are probably the most understood of all of the different types of damage associated with ion implantation. They are associated with imperfect regrowth of any amorphous layer produced during implantation. One important aspect of such defects is that they can be avoided. The two major types of category III defects are "hairpin" dislocations and microtwins. These defects were sucessfully avoided in most of our experiments and the model for their nucleation and growth is fairly well established, therefore, the discussion concerning these defects will not be as involved as for other defects categories.

4.3.1 Hairpin dislocations

Hairpin dislocations are one of the earlier forms of implant damage characterized by TEM.[132] These defects are associated with the regrowth process of the amorphous layer.[148] Extensive studies by Sands et al,[34] using high resolution TEM, showed that hairpin dislocations nucleate when the regrowing amorphous/crystalline interface encounters small microcrystalline regions that have become misoriented slightly with respect to the bulk crystalline material. As the microcrystalline pocket is incorporated into the single crystal bulk a hairpin dislocation is nucleated. This dislocation propagates with the advancing a/c interface, becoming "V" in shape until it intersects the surface.

To avoid hairpin dislocations, it is necessary either not to form the misoriented microcrystalline regions or to remove them prior to solid phase epitaxial growth of the amorphous layer. Implantation with lighter ions (Si^+ versus Ge^+) results in a broader a/c transition region (2-15 times wider). The broader transition region contained a large number of misoriented microcrystallites and subsequently resulted in a greater number of hairpin dislocations.[34,78,153,154] This observation has led several groups to propose using Ge^+ instead of Si^+ ions for preamorphizationof Si.[34,155] In addition to the lower probability of

producing hairpin dislocations, the category II density is also less for low dose Ge^+ implants.

Another means of reducing the a/c transition width and the number of misoriented microcrystallites is by reducing the amount of ion beam induced epitaxial crystallization (or dynamic annealing), which occurs during implantation. If the wafer is cooled to liquid nitrogen temperatures during implantation, then the effective threshold damage density is reduced and the a/c transition width becomes narrower. Such cooling does avoid misoriented microcrystallite formation.[34] Our results indicate that, if the implantation is stabilized at room temperature using a Waycool implanter endstation, then hairpin nucleation can be avoided. However, as shown in figure 24, if the wafer cooling is inadequate during implantation and significant wafer heating occurs (Wayflow endstation), then even for heavier ions (As^+) hairpin formation becomes probable. In figure 24, a buried amorphous layer was produced, thus, the hairpin dislocations, nucleated at both a/c interfaces and grew to the depth where the two interfaces met (category IV region). Other studies[156] also note that use of a Wayflow endstation results in a large number of defects residing within the regrown amorphous layer region.

A novel means of avoiding hairpin dislocations has been reported by Rozgonyi et al.[156,157] Using what they termed "very low temperature annealing" (VLTA, 250-450°C) prior to solid phase epitaxial growth, it was possible to reduce the concentration of misoriented microcrystallites. High resolution TEM results indicate that the microcrystallites are metastable with respect to the amorphous phase. There is a slight increase in the amorphous layer thickness and a narrowing of the a/c transition region during VLTA treatment. This is shown to result in a reduction in the concentration of hairpin dislocation upon annealing.[157] VLTA is a processing step which allows preamorphization conditions to be expanded while still avoiding category III defects. These

broader preamorphization conditions would include increasing the implant energy, decreasing the dose or possibly decreasing the mass of the ion.

4.3.2 Microtwins

There have been a large number of published reports showing a correlation between use of {111} oriented wafer and microtwin formation upon amorphous layer regrowth.[50,64,69,123,159-165] The solid phase epitaxial growth rate was observed to be an order of magnitude slower for {111} oriented wafers than {100} wafers, as previously mentioned. Also {100} wafers did not result in any microtwin formation.[69] Various crystallization models have been proposed to explain microtwinning.[69,73,166] Washburn[69] discusses a model which accounts for both microtwin formation and the slower regrowth rate of the amorphous layer for {111} oriented wafers. The model is based on the bonding arrangements of the different [{111}, {110} and {100}] surfaces. In the model, formation of two undistorted bonds defines the difference between an atom in the amorphous phase and one that is part of the crystal. On a {001} face an atom can add anywhere and form two undistorted bonds, whereas for the {111} face requires simultaneous attachment of three adjacent atoms for the nucleation of a growth step. These three atoms can add in the correct position or with a twin orientation. Nucleation of the microtwins is frequently observed on the {111} planes inclined to the surface.

Figure 25a shows a cross-sectional TEM micrograph comparing a {111} versus {100} oriented wafer after amorphous layer regrowth. The samples were implanted at 190keV As^+ at a dose of $3 \times 10^{15}/cm^2$. The high density of microtwins for the {111} oriented wafer is missing for the {100} wafer. A Wayflow endstation was used for these implants thereby allowing some ion beam induced epitaxial crystallization (IBIEC) to occur. It is interesting to note that microtwin formation occurs whether the amorphous layer is regrown by thermal annealing (section closest to the surface) or by ion beam induced

epitaxial crystallization (lower region). The observation that microtwin formation occurs for arsenic implantation at elevated temperatures (200-300°C)[170] differs from phosphorus implantation at elevated temperatures[69] (100°C) which shows that twin formation is suppressed.

Upon annealing at higher temperatures (900°C), the microtwin defects evolve into a tangle[163] of dislocations (figure 25b) which are difficult to dissolve, even with furnace annealing of 1100°C.[167]

Microtwin formation does not always occur for {111} oriented wafers,[112] however, it rarely occurs for {100} oriented wafers (except under conditions favoring segregation related defects). Thus {100} oriented wafers were used for the bulk of the experiments discussed in this text.

4.3.3 Segregation defects

There is a third type of category III defect associated with the rejection of an implanted species by the moving amorphous/crystalline interface.[78,148,168-169] These defects generally extend from the surface to a depth of 300-500Å. They have been observed in samples implanted with flourine (BF_2) and high doses of indium. Because of the low solid solubility of these species in the crystalline silicon, the ion stays in the amorphous layer as long as is thermodynamically possible. However, at some maximum concentration, the regrowing a/c interface breaks down and defect formation occurs. These defects include misoriented microcrystallites, microtwins,[148] fine clusters (15-40Å in diameter) and small stacking faults.[168,169]

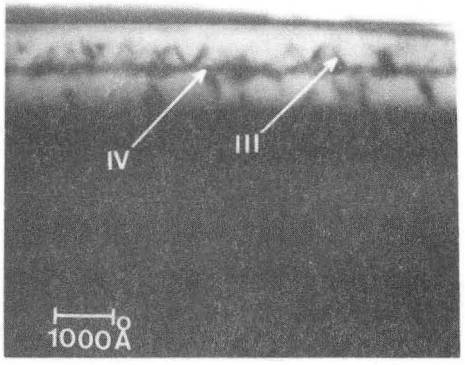

as-implanted

Annealed 900°C 30 minutes
XBB 873-2374

Figure 24

190 keV ^{75}As 5 x 10^{15}/cm^2, {100}, Wayflow Endstation
Bright Field, g_{220}

{100}

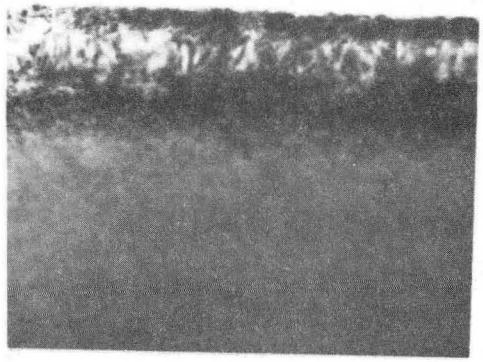

{111}

Figure 25a

190 keV ^{75}As 3 x 10^{15}/cm^2, Wayflow Endstation
Annealed 550°C 16 hours, Plan-view TEM, Bright Field, g_{220}

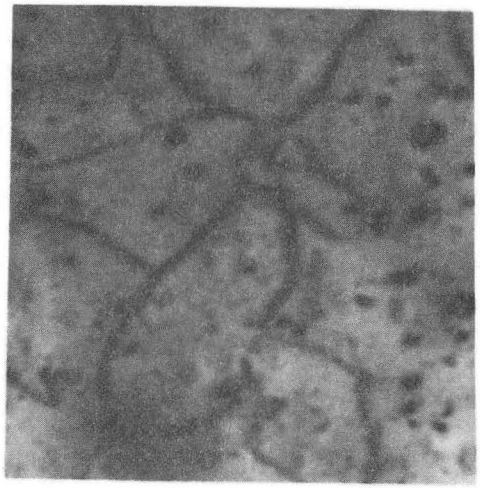

Plan-view TEM

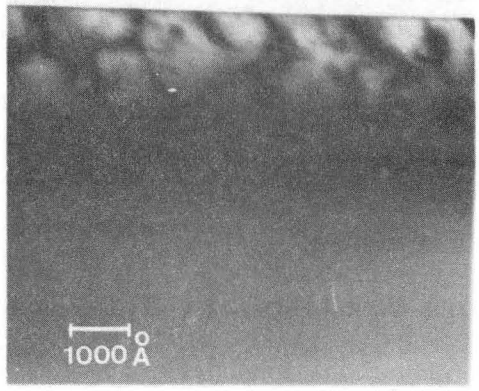

Cross-sectional TEM

XBB 873-2375

Figure 25b

160 keV ^{31}P 1 x 10^{15}/cm^2, {111}, Waycool Endstation
Annealed 900°C 30 minutes, Bright Field, g_{040}

4.4 Category IV Damage

Correlation between the damage density distribution with the effective threshold damage density, shows that a buried amorphous layer is produced prior to a surface amorphous layer with increasing dose. The regrowth of this buried amorphous layer results in a layer of defects labeled category IV defects[63] ("clamshell" defects[112]). These defects form where the two advancing a/c interfaces meet. Existance of these defects has been known for at least fifteen years.[171,89,172] Many different detection techniques, in addition to TEM, have noted category IV defects such as Cu decoration in conjunction with a radiochemical method,[171] Rutherford backscattering,[112,173] profiling of the free carrier mobility,[172] and flourine decoration in conjunction with ion microprobe mass analysis.[35] However, few studies characterizing category IV defects have been published. This is because both cross-sectional TEM samples and unusual plan-view TEM characterization methods[112] are needed to distinguish between category II and IV defects.

4.4.1 {111} Oriented Wafers

One of the few extensive works on category IV defects was done by Sadana et al.[112] Low dose ($5 \times 10^{14}/cm^2$) 120 keV P^+ implantation of (111) Si resulted in a buried amorphous layer, in their experiment. Regrowth of the amorphous layer at 550°C showed that the lower a/c interface advanced more rapidly than the upper a/c interface. Annealing at temperatures between 750°C and 1000°C resulted in the formation of two descrete layers of dislocation loops. By ion milling the implanted surface of the plan-view TEM sample, it was possible to characterize the dislocation loops in the different (category II and category IV) layers. After 950°C annealing, larger dislocation loops (~1000Å diameter) were observed in the category IV region than in the category II (~300Å diameter) region. The category IV loops consisted of both faulted dislocation loops (Burgers vector = a/3<111>) on the (111) plane parallel to the surface and perfect dislocation loops (Burgers vector = a/2<110>) on

{110} planes. The category II loops were the same as the category IV loops but they also included faulted dislocation loops on the other {111} planes. All of the loops were extrinsic in nature. SIMS analysis showed that segregation[69] of the phosphorus to the defects layers occurs upon annealing and the segregated concentration reaches a maximum at 750°C.[112]

4.4.2 {100} Oriented Wafers

Category IV defects were also studied, by us, for As^+ implantation of {100} oriented wafers.[174] Different types of category IV dislocation loops were observed for {100} regrowth compared to the {111} regrowth just discussed. In order to produce a buried amorphous layer, a Wayflow endstation was used on the implanter and the wafer was not tilted during implantation. The dose varied between $1 \times 10^{15}/cm^2$ and $5 \times 10^{15}/cm^2$ for the 190 keV implants. Figure 26 shows both plan-view and cross-sectional TEM micrographs of a sample implanted with a dose of $1 \times 10^{15}/cm^2$ and subsequently annealed. The plan-view micrograph of the sample annealed at 550°C shows large irregular dislocation loops. Comparison of the cross-sectional sample, in both a tilted and normal orientation in the microscope and the plan-view sample indicate that these large irregular disolcation loops are category IV defects. Analysis of the Burgers vectors of these defects indicate the loops are shear type loops i.e. the Burgers vectors are parallel to the habit plane of the loops and both are parallel to the (001) surface of the wafer. It is not suprising that the large loops are shear in nature, for on the basis of the other categories of defects, annealing at 550°C is insufficient to produce such large dislocation loops (~1000Å diameter) by climb. The shear nature may be due to the misorientation of the two interfaces when they meet.

The location of the category IV layer is closer to the upper amorphous/crystalline interface than the lower a/c interface. This implies a greater regrowth velocity of the lower a/c interface than the upper a/c interface. This was also observed for {111} oriented wafers, as mentioned. One possible explanation for the location of the category IV defects

is the effect of doping on the regrowth velocity.[80] Figure 27 shows a correlation between the a/c position and the calculated ion distribution. The lower a/c interface is exposed to a much greater doping concentration which may influence the final category IV position. The fact that the wafer was not tilted off axis during implantation would skew the profile in favor of an even higher dopant concentration at the lower a/c interface.

Further annealing at 900°C for 30 minutes (figure 26) results in the movement of some of the large category IV dislocation loops out of the plane parallel to the surface while other loops retain their shear nature. The category II damage evolves into small (100-300Å diameter) extrinsic perfect and faulted dislocation loops, with 900°C annealing. These results indicate that the category II loops have the same morphology for both the {111}[112] and {100} oriented wafers. However, since shear dislocation loops parallel to the surface are not possible for (111) wafers, only small defect clusters were observed after regrowth of the amorphous layer (≤600°C).

The effect of dose on the category IV defects was also investigated. Figure 28 shows the influence of increasing the dose from $1 \times 10^{15}/cm^2$ to $3 \times 10^{15}/cm^2$. The micrographs show that after 550°C annealing both samples have category II and category IV defects. A few category III (hairpin) dislocations were also observed for the higher dose sample. The defect annealing kinetics at 900°C varied dramatically for the two different doses. After 30 minutes at 900°C, the category III and most of the category IV dislocations have annealed out and only the category II dislocation loops (which have grown in size) remain for the higher dose sample. The dissolution of the category III and IV dislocations will be discussed further in section 4.6. The larger category II loops are not shear in nature although in plan-view they resemble the category IV loops in figure 26. These results illustrate the need for both plan-view and cross-sectional TEM for proper interpretation.

The ion beam induced epitaxial crystallization, which occured during the As^+

implantation because of the Wayflow endstation, not only prevented the amorphous layer from reaching the surface, but at the highest dose studied (5 x $10^{15}/cm^2$) resulted in complete regrowth of the amorphous layer (figure 24). Thus, category IV dislocations were observed to have formed in the as-implanted sample, prior to any furnace annealing. Category III dislocations (hairpin dislocations) were also observed to form nucleating at both amorphous/crystalline interfaces, as previously mentioned. Additional annealing of this higher dose sample at 900°C, results in a double layer structure. In this case the upper layer of loops is believed to be category V defects, not category IV defects. Category V defects are possible because at this dose because the solid solubility of As in Si at 900°C is exceeded (section 4.5). Another reason to believe the upper layer of defects are category V defects is based on the observation just mentioned reguarding the instability of the catagoy IV and III defects for higher dose implants (3 x $10^{15}/cm^2$) after annealing at this time and temperature (900°C, 30 minutes).

Category IV defects can be avoided by producing a surface amorphous layer. This is possible by several means such as decreasing the implant energy for a given dose, as shown in figure 29. The formation of a surface amorphous layer at the lower energy (100 keV) resulted in the formation of category II dislocation loops only.

From these results, it appears that category IV defects have very different morphologies depending upon the wafer orientation. The defects appear to arise from either a slight displacement of the two intersecting amorphous/crystalline interfaces or the coalescence of excess interstitials rejected by the advancing a/c interfaces. The stability of the defects is dose dependent for the As implants and probably for the P implants (chapter 5). Research on category IV defects is still in its infancy and additional work is needed to understand their characteristics.

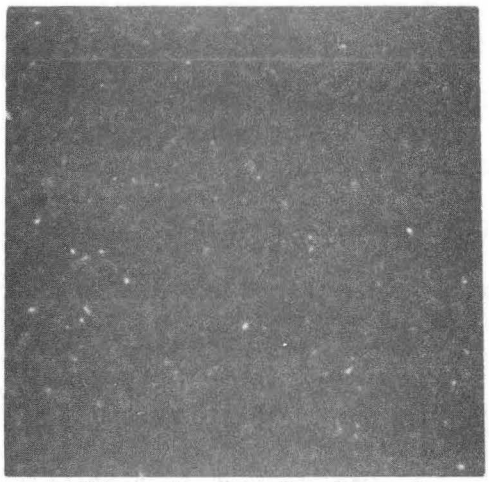

Plan-view, as-Implanted

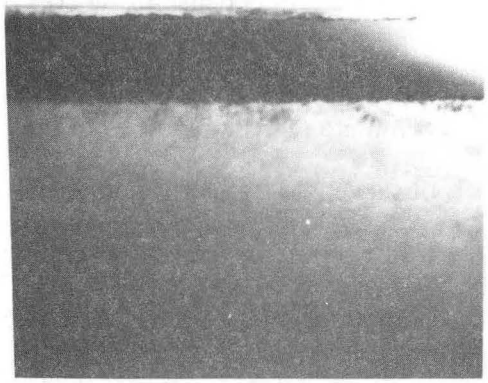

Cross-section, as-implanted

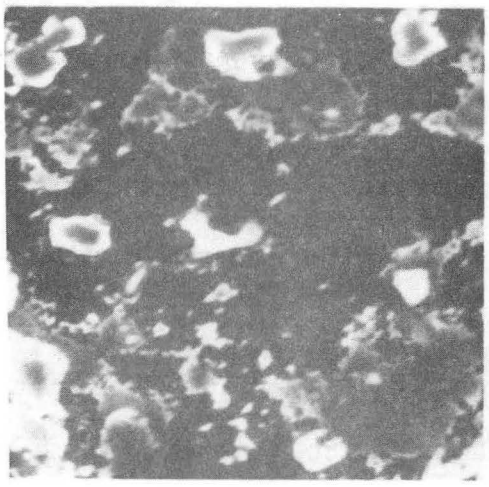

Plan-view, 550°C 16 hours

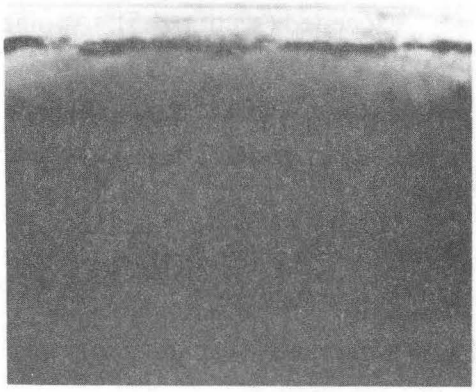

Cross-section, 550°C 16 hours

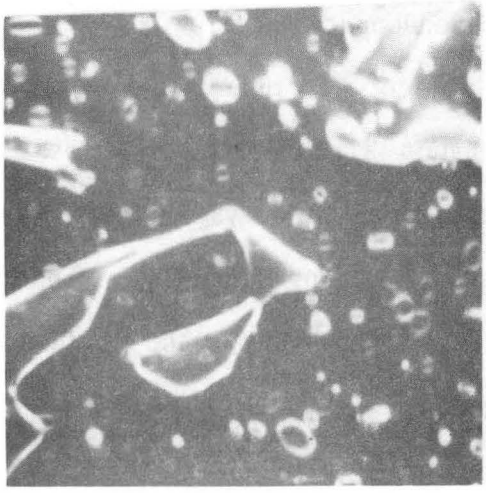

Plan-view, 900°C 30 minutes

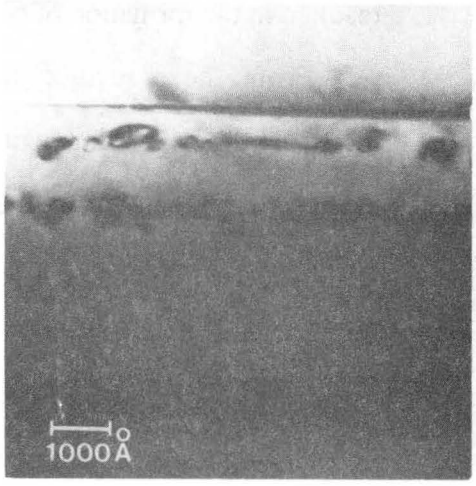

Cross-section, 900°C 30 minutes

XBB 873-2376

Figure 26

190 keV ^{75}As 1 x 10^{15}/cm^2, {100}, Wayflow Endstation
PTEM: Centered Dark Field, XTEM: Bright Field, g_{220}

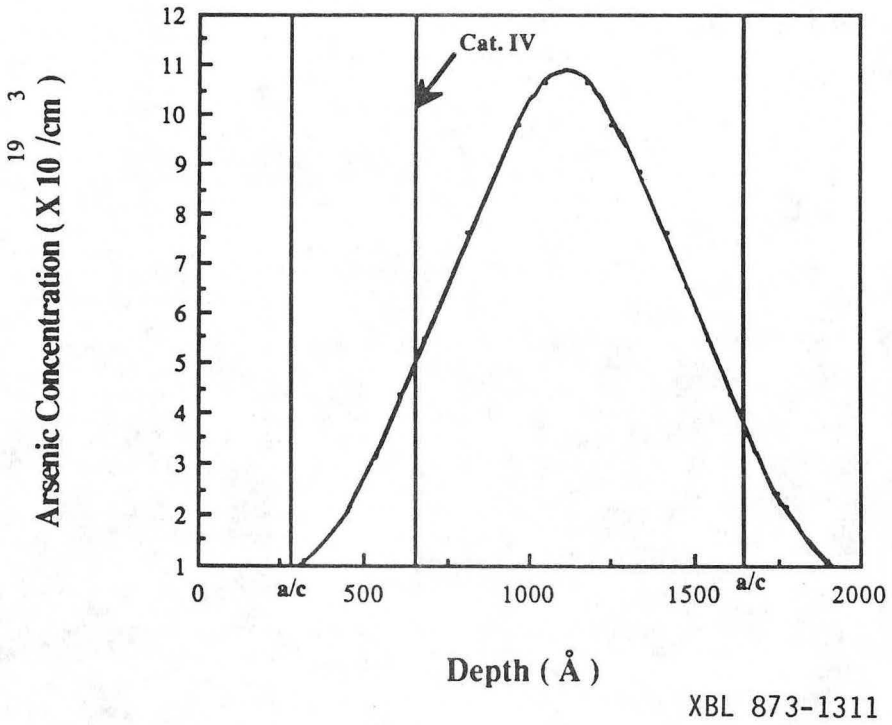

XBL 873-1311

Figure 27

Correlation Between Final Ion Distribution and Location of Catagory IV Defects. 190 keV ^{75}As 1 x 10^{15}/cm^2, {100}, Wayflow Endstation

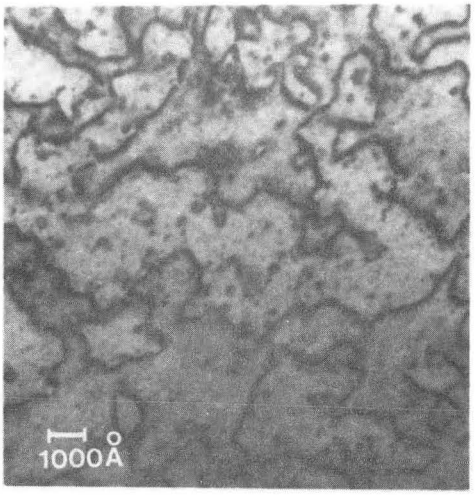

Plan-view, 550°C 16 hours

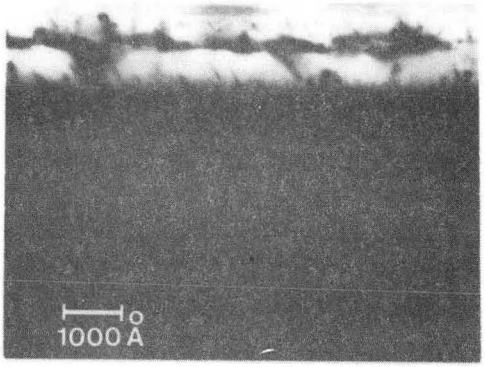

Cross-section, 550°C 16 hours

Plan-view, 900°C 30 minutes

Cross-section, 900°C 30 minutes

XBB 873-2377

Figure 28

190 keV ^{75}As 3 x 10^{15}/cm^2, {100}, Wayflow Endstation
Bright Field, g_{220}

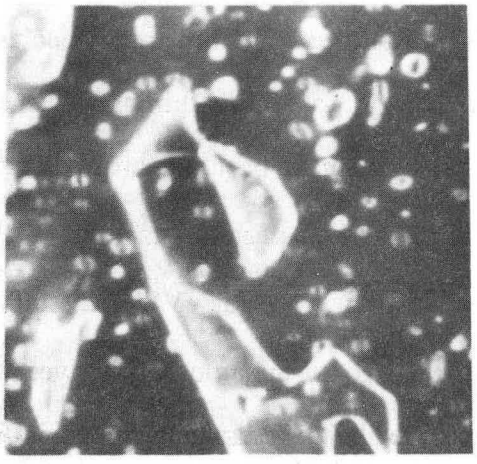

Plan-view, 190 keV

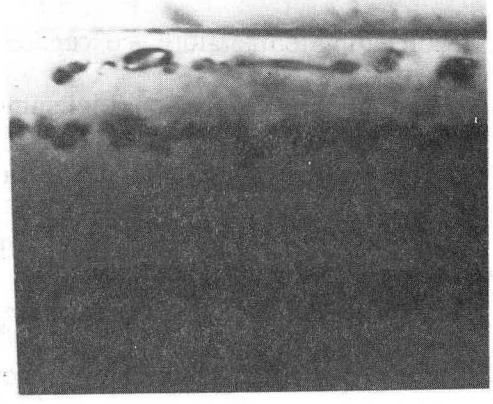

Cross-section, 190 keV

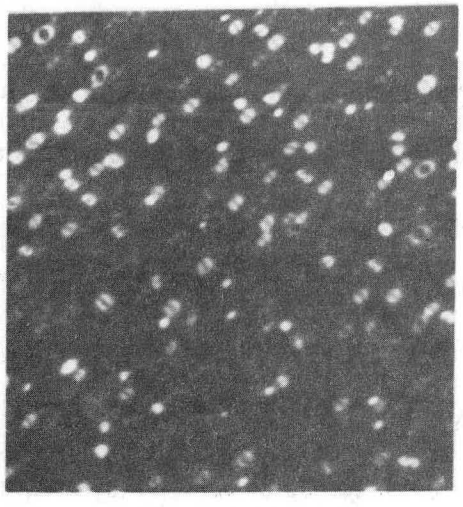

Plan-view, 100 keV

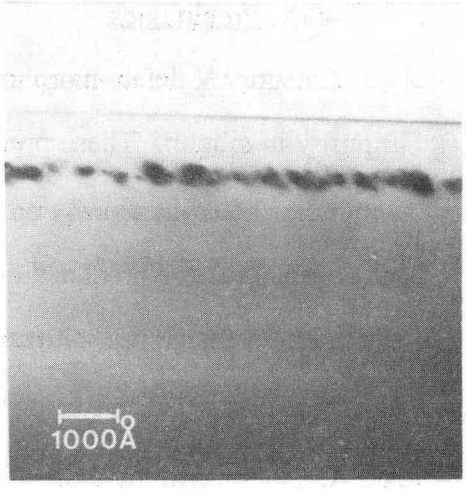

Cross-section, 100 keV

XBB 873-2378

Figure 29

1 x 10^{15}/cm^2 ^{75}As, {100}, Wayflow Endstation, 900°C 30 minutes
PTEM: Centered Dark Field, XTEM: Bright Field, g_{220}

4.5 Category V Damage

The final group of defects in this classification scheme are category V defects. As mentioned, these defects occur when the solid solubility of the implanted species at the annealing temperature is exceeded. These defects are not found for all implanted species, at least under the dose conditions investigated by us. There have been numerous observations of category V defects for both RBS and TEM studies of high dose In, Sb,[175-179] As,[140,180,181] Ga[177] and Al[182] implants after annealing. Category V defects most often arise from the following annealing sequence. Regrowth of the amorphous layer at 550°C for example, can result in the concentration of electrically active dopants exceeding the solid solubility of the dopant.[183] If the solid solubility has been exceeded then annealing at this higher temperature can produce precipitates (50-500Å in diameter) which may be imaged by diffraction contrast in the transmission electron microscope. The location of category V defects beneath the surface has been shown to be centered about the projected range where the maximum concentration occurs.[181]

4.5.1 Precipitates

Category V defect morphology almost always consists of precipitates of the implanted impurity in silicon. These precipitates are believed to nucleate both homogeneously and sometimes heterogeneously on category II dislocations.[64] The precipitates have in general the crystal structure predicted by the phase diagram and powder X-ray diffraction files. For example, extensive microdiffraction studies of antimony precipitates indicate they have a rhombohedral crystal structure and additional studies of other "alloy" systems (In,[177] Ga[178] and Al[182]) confirm the model that these defects are precipitates, which may involve silicon if predicted by the phase diagram. Category V defects are shown in figure 30 for Ga and Sb implants where the peak concentration exceeded the solid solubility at the 900°C annealing temperature. Category V defects have also been observed for high dose boron

implants into preamorphized silicon. These defects are probably a silicide, however the defects need to be larger for crystal structure determination by microdiffraction.

Category V defects may not always have a precipitate morphology. It has been reported by Pennycook et al[176-178] that extrinsic dislocation loops can also form if a group V element is the implanted impurity. They reported extrinsic dislocation loop formation and precipitate formation for antimony implants and only dislocation loop formation for arsenic implants. In addition, after studying the growth rate of precipitates for Sb, Ga,In and B implanted samples, as a function of annealing temperature, they conclude that the diffusivity is enhanced for group VA elements but not for IIIA elements. From these observations, they propose the existance of a trapped group VA-Si_i complex which can survive epitaxial regrowth of the amorphous layer but dissociates at higher temperatures (600°C-800°C) resulting in the enhanced diffusivity and extrinsic dislocation loop formation. In our studies, no category V dislocation loop formation was observed for antimony or phosphorus implants (figure 30 and 31). Initial investigations indicate that antimony, gallium and aluminum only formed precipitates and category II dislocation loops. The antimony observations contradict Pennycook's findings. The figure of the category V dislocation loops reported by Pennycook[193-195] for antimony implanted silicon consisted of a series of plan-view micrographs in which it is possible to confuse category II dislocation loops with category V defects. As stated, no category V defects (precipitates or dislocation loops) were observed for the high dose phosphorus implants (figure 31). However, since the effect on the category II dislocation loop annealing kinetics (enhanced dissolution) is quite pronounced and consistant with other high dose species implants studied, and our Hall effect measurements indicate an increasing surface carrier concentration with 900°C annealing, some form of clustering must occur.

4.5.2 Half Loop Dislocations

Unusual category V defects form for high dose arsenic implantation. These defects have a morphology consisting of extrinsic dislocation loops and/or possibly plate-like precipitates, as will be shown. Category V defects greatly influence the category II defect annealing kinetics making the need to understand them important in order to produce defect free Si with the minimum amount of thermal cycling. Arsenic implants, which result in the peak concentration exceeding the solid solubility, can also result in the nucleation and growth of relatively stable extrinsic half loop dislocations upon annealing. The study of these half loop dislocations enables us to better understand category V defects in As implanted Si. The rational behind this is two fold. First, half loop dislocations nucleate in the category V defect layer and second their growth can only be explained qualitatively and quantitatively by the dissolution of arsenic clusters or precipitates. Half loop dislocations were always observed for high dose As implants (above solid solubility) but were almost never observed for any other species. There may be a correlation between the unusual morphology of the category V defects in As implanted Si and the formation of half loop dislocations. This investigation of half loop dislocations is primarily based on observing the isothermal defect annealing kinetics.

The study of ion implantation damage annealing kinetics is interesting from the standpoint of understanding how to eliminate the damage as well as how to use the damage as an indicator of changes in the point defect equilibrium. One of the more notable uses of damage as an indicator involves the oxidation enhanced growth of extrinsic stacking faults, indicating that Si_i were the point defects being introduced by oxidation.[179,184] Another type of damage which also behaves as a "detector" of point defect perturbations has been discovered in high dose arsenic implanted silicon. As noted by several authors,[185-187] upon annealing high dose ($5 \times 10^{15}/cm^2$) arsenic implanted silicon, extrinsic half loops are

observed to form. Mader et.al.[186,129] has discussed a model for the nucleation of half loop dislocations which involves a transition from discrete dislocation loops to a winding dislocation structure and finally to half loop dislocations. We observed no winding dislocation structure during the nucleation of half loop dislocations therefore, a new model for the nucleation of half loop dislocations is proposed.

According to Mader, the winding structure is only observed for implants conducted through an oxide on the surface which implies that the recoiled oxygen may influence the annealing kinetics in favor of the winding structure by pinning the dislocations. The transition from descrete loops to winding loops according to the model occurs via Lomers type reactions[75] between neighboring dislocation loops. This may indeed be an accurate model for winding dislocation loop formation, unfortunately no cross-sectional TEM studies were performed so it is not possible to state whether the winding dislocation structure forms from reaction of the category II or V defects.

The remainder of this discussion on how category V defects account for half loop dislocations will be divided into explaining what a half loop dislocation is, how it nucleates and finally how its growth upon annealing can be quantitatively explained by arsenic precipitate dissolution and used as a detector to monitor gross changes in the interstititial/vacancy equilibrium.[108]

In this study the starting material was (001) p-type, 5-10 Ω-cm, Czrochralski grown silicon wafers which were implanted with 100 keV $^{75}As^{+}$ using a Waycool implanter endstation. The doses studied ranged from $2 \times 10^{14}/cm^2$ to $1 \times 10^{16}/cm^2$. These implant conditions resulted in the formation of a surface amorphous layer for all doses. Although the amorphous layer was produced by the arsenic implantation, it was not suprising to find the defect annealing kinetics, including half loop formation, to be exactly the same for samples which had been preamorphized by either Si or Ge implantation prior to the high dose As implantation. The amorphous layer was regrown by annealing at 550°C for 8

hours and subsequent annealings were performed at 900°C in a nitrogen ambient. Both plan-view and cross-sectional TEM were utilized to examine the defect structures.

Figure 32 shows the as-implanted cross-sectional TEM micrograph of a 1 x $10^{16}/cm^2$ As^+ implant. Note that a surface amorphous layer was produced. Figures 32 also shows cross-sectional and plan-view TEM micrographs of the same sample after annealing at 900°C for 4 minutes. Two descrete layers of defects are observed in the cross-section micrograph after annealing. The upper layer of defects are category V defects while the lower layer are category II extrinsic dislocation loops. This structure resembles the category IV and category II double layer of defects which occurs for buried amorphous layers. However, since a surface amorphous layer was produced, the two layer structure in figure 32 is not the result of a buried amorphous layer but rather forms from exceeding the solid solubility of As in Si.

Figure 33 shows, in plan-view, the effect of isothermal annealing, at 900°C, on the sample in figure 32. The straight lines in figures 33, after annealing for 4 and 16 hours, are half loop dislocations which have nucleated and grown. An extrinsic half loop is an extra plane of atoms inserted perpendicular to the surface. Figure 34 shows the plan-view sample in figure 33 (16 hours), tilted 35° form the (011) pole about the [110] direction. The sides of the half loop dislocation are now visible. The schematic in figure 35 illustrates the orientational relationship of the half loops. The habit planes are the (110) and $(1\bar{1}0)$ planes perpendicular to the surface and the Burgers vectors are a/2[110] and a/2$[1\bar{1}0]$ respectively, perpendicular to the habit planes. In other words, the half loop dislocation is pure edge in character.

<u>Nucleation</u>: Close inspection of figure 33 shows some of the loops becoming elongated after 30 minutes at 900°C. After 60 minutes of annealing some of the elongated loops have reached the surface. Burgers vector, **g·b**, analysis of the elongated loops in figure 33 indicate that the Burgers vectors are a/2[110] and a/2$[1\bar{1}0]$ parallel to the surface and equivalent to the Burgers vectors of the half loop dislocations. We propose that these

elongated dislocation loops are the half loop nuclei. Figure 36 show the cross-sectional micrographs corresponding to figures 33. Weak beam dark field **g·b** analysis of the cross-sectional sample indicates that some of the category V defects have Burgers vectors of a/2[101] or a/2[011] inclined to the surface. The analysis also showed the habit planes of these loops to be {112} type planes. High resolution TEM studies of the category V defects also showed some of the category V defects to be faulted dislocation loops with Burgers vectors a/3<111> on {111} type planes. The concentration of the elongated loops (half loop nuclei) is much less than the total category V defect concentration. The habit plane of the half loop nuclei was not determined.

In figure 36 (900°C, 1 hour) a half loop is seen in cross-section. The small half loop dislocation only extends down to the layer of category V loops. The depth of the half loop dislocations during their initial stage of growth was consistantly found to be equal to the depth of the category V defect layer and was also verified by tilting experiments using the plan-view TEM samples. In addition, only category V defects were observed to be growing larger in diameter with the shorter time annealing treatments (≤ 1 hour). It is therefore proposed that half loop nuclei are category V defects. The Burgers vector analysis also suggests that only those category V defects with Burgers vectors parallel to the surface become half loop dislocations. This may correlate with the fact that their glide cylinder is parallel to the surface and as such they cannot be eliminated by glide to the surface.

Growth: The half loop dislocations are observed to grow by negative climb. Discussions on the climb of edge dislocations on {110} planes in FCC materials were published many years ago.[188] Figures 36 also shows cross-sectional views after annealing for 4 and 16 hours at 900°C. In addition to a half loop which is seen edge on, it is also apparent that all of the category II defects are gone and only a few of the category V defects remain. Wu et.al.[189] has suggested that category II loops may be gliding to the surface. Based on our observations for As and other species implanted at high doses we found no evidence to

indicate that glide is occuring. We believe that the category II dislocation loops are dissolving by positive climb. This effect of category V defects on category II defect dissolution will be discussed further in chapter 5. Figure 33 also shows the total loop concentration to decrease upon annealing. The category II loops are known to be extrinsic, which implies that solution of the small loops could lead to growth of the half loop dislocations. The graph in figure 37 is a plot of the concentration of atoms (cm^{-2}) bound by the extrinsic loops for the different size loops as a function of annealing time. The concentration of atoms bound by the half loop dislocations increases steadily upon annealing from 4 hours to 72 hours at 900°C. However, the concentration of atoms bound by the small and medium loops decreases rapidly for annealing times between 30 minutes and 2 hours and then becomes insufficient to supply enough atoms for half loop growth.

One method to determine whether the source of point defects is in the near surface region or in the bulk is to study the length to depth aspect ratio of the "indicator" loop at the surface. This technique was used in the study of oxidation induced stacking faults.[190] A ratio greater than two implies that the source of the point defects is at or near the surface, which is the case during oxidation. Figure 38 shows the aspect ratio of the half loops (determined by tilting experiments) as a function of the size of the half loop, or annealing time. The graph shows the ratio to be much greater than two as the half loops grow, thus the bulk is not the source of the interstitials. Oxidation of the surface is also not the source since all annealings were performed in a neutral, dry nitrogen, ambient and subsequent oxide thickness measurements indicated less than 20Å of oxide growth.

Figure 39 shows the effect of dose on half loop formation. All samples were annealed four hours at 900°C. Doses less than or equal to $2 \times 10^{15}/cm^2$ resulted in no half loop formation, while higher doses did result in half loop formation. It was proposed earlier that the half loop nuclei are category V defects. This is confirmed in figures 39 and 40, which show that when the dose drops from $5 \times 10^{15}/cm^2$ to $2 \times 10^{15}/cm^2$, half loop dislocations

and category V defects do not form. The peak concentration is calculated to decrease from $1.6 \times 10^{21}/cm^3$ to $6.4 \times 10^{20}/cm^3$ when the dose is decreased from $5 \times 10^{15}/cm^2$ to $2 \times 10^{15}/cm^2$. This was confirmed by SIMS analysis of the samples. The solid solubility of As in Si, as determined by Trumbore[191], does not extend as low as 900°C. However by using the As:Si phase diagram,[192,193] in combination with Trumbor's data and the method described by Weber,[194] a crude extrapolation of the solid solubility down to 900°C may be made. The estimated solid solubility is $\sim 1.4 \times 10^{21}/cm^3$. This value matches well with the value published by Olesinski et. al.[193] of $\sim 1.2 \times 10^{21}/cm^3$. Thus, category V defects as well as half loop nuclei appear to be associated with exceeding the solid solubility of As in Si.

The source of the interstitials for half loop growth has yet to be determined. Nucleation of the half loop dislocations is associated with precipitation, it is therefore logical to suggest that dissolution of arsenic clusters or precipitates might supply the excess interstitials for half loop growth. In order to test this model, room temperature Hall effect measurements[21] of the surface concentration of electrically active dopants as a function of annealing time at 900°C were performed (figure 41). After 16 minutes only 2-3% of the dopant is electrically active. With additional annealing the concentration of free carriers was observed to increase, implying that arsenic clusters or precipitates are dissolving during the growth of the half loops. Also plotted in figure 41 is the concentration of atoms bound by the half loop dislocations as a function of annealing time. Direct comparison of these two curves indicates the dissolution of arsenic precipitates can both qualitatively and quantitatively explain the observed climb of half loop dislocations. These results are supported by recent results published by Kamgar et. al.[180] They indicate that for arsenic implants of dose $5 \times 10^{15}/cm^2$, sufficient to produce half loop dislocations, there exist three domains in terms of electrical activation of the arsenic. The first domain is recrystallization of the amorphous layer which results in a large fraction of the arsenic occupying

substitutional sites, as previously stated. The second domain shows a drop in the substitutional arsenic concentration due to precipitation, and the third domain shows reactivation of the arsenic due to diffusion of the arsenic and subsequent declustering of the precipitates. Kamgar's results indicate that, for 900°C annealing, the transition from precipitation to declustering occurs between 1 and 2 minutes. Since our shortest annealing time was 4 minutes then declustering occured during half loop growth.

The question of the morphology of the arsenic precipitates remains. High Resolution TEM studies were done on the category V defects to determine if any of the defects are plate-like precipitates. Such a morphology is predicted since arsenic forms a hexagonal phase which would fit well on the {111} planes of silicon. The results of this study are shown in figure 42. Some of the defects (seen edge-on) showed no displacement across the loop and showed a dark contrast within the loop. A CEMPAS[195,196] computer simulation of the image expected if the Si atoms of one (111) plane were replaced by As atoms is also shown in the figure. The optimum Schertzer defocus and a thickness of 500Å was used in the simulation. The match between the computer simulation and the image is quite good implying that at least some of the category V defects may be plate-like precipitates. The concentration of atoms bound by both the category II and V dislocation loops is shown in figure 37 to be have a maximum value of $2 \times 10^{14}/cm^2$ after 30 minutes at 900°C. The concentration of arsenic which is electrically inactive is approximately $9.9 \times 10^{15}/cm^2$. Thus, if some of the category V defects are plate-like precipitates, they cannot account quantitatively for all of the electrically inactive arsenic. No other defects were observed by HRTEM, so the inactive arsenic clusters must be smaller than the detectability limit of this technique. Integration of the SIMS profile indicates that essentially 100% of the arsenic is in the near surface region. It has been proposed that arsenic forms stable dimers and trimers.[197,198] This has been used to explain why phosphorus implantation gives lower resistivity contacts than arsenic implantation.[136] Therefore, small clusters may account for

the missing arsenic precipitates.

Half Loop Summary: The following is a summary of the events leading to the formation and growth of half loop dislocations in high dose ($\geq 5 \times 10^{15}/cm^2$) As implanted {100} Si. Upon recrystallization of the amorphous layer at 550°C approximately 100% of the implanted arsenic is electrically active. With isothermal annealing at 900°C the following sequence occurs. For times less than 1 minute, clustering or precipitation occurs. After 2 minutes, declustering begins and after 4 minutes, category V defects were observed. The category V defects may exist after shorter anneals but this was the shortest time investigated. After 30 minutes, elongated loops which are proposed to be the half loop nuclei were observed. Upon annealing for 1 hour, half loop dislocations were observed. For annealing times between 2 hours and 72 hours, the half loops were observed to grow.

The half loop nuclei have been shown to be category V defects. These loops are associated with exceeding the solid solubility of As in Si. By decreasing the dose such that the peak of the As profile is below the solid solubility, neither the projected range loops nor the half loops form. The half loop nuclei are shown to be extrinsic dislocation loops, in the category V defect layer, which have Burgers vectors of a/2<110> type parallel to the surface. The half loops are extrinsic in nature with Burgers vectors of a/2<110> perpendicular to the {110} type habit plane and parallel to the surface.

The source of the point defects resulting in half loop growth, appears to be the declustering of arsenic precipitates. This model is supported by Hall effect measurements which indicate arsenic clusters are dissolving during half loop growth and that the precipitates can quantitatively account for the observed half loop size. HRTEM results indicate that some of the category V defects may be plate-like precipitates. Quantitative analysis of the concentration of atoms bound by all of the dislocation loops which are not half loops, indicates that the dissolution of the other loops, including any plate-like precipitates, is not responsible for the observed half loop growth. It is therefore concluded that both the nucleation and growth of half loop dislocations in As implanted Si are a result

of exceeding the solid solubility of As in Si.

Category V defects for all species except As appear to be precipitates and some of these appear to be plate-like precipitates. Category V defects do not always form (as with phosphorus) but they do have a pronounced affect on the defect annealing kinetics. This is believed to be associated with a disturbance of the point defect equilibrium and can result in enhanced dissolution of the category II defects.

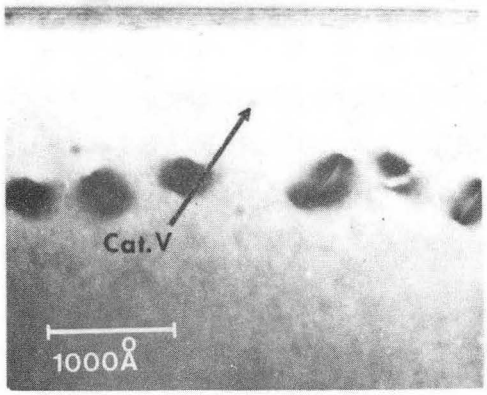

100 keV ^{70}Ga 1 x 10^{15}/cm^2, {100}
Annealed 900°C 2 hours

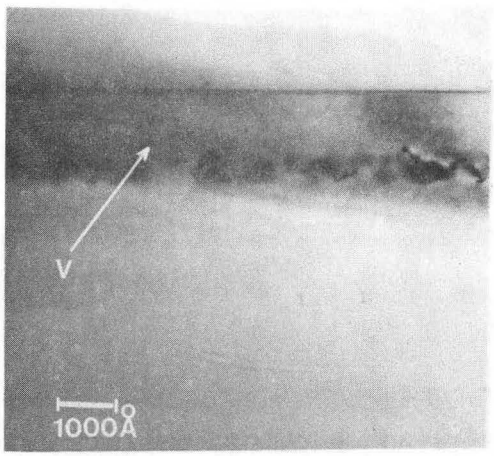

190 keV ^{122}Sb 2 x 10^{15}/cm^2, {100}
Annealed 900°C 30 minutes

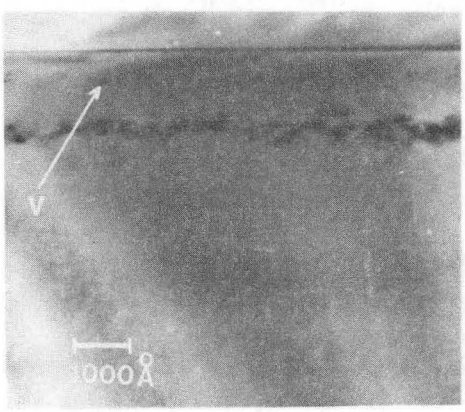

17 keV ^{11}B 1 x 10^{16}/cm^2 into {100} preamorphized Si,
(70 keV + 30 keV ^{28}Si, 5 x 10^{15}/cm^2 each)
Annealed 900°C 1 hour

XBB 873-2379

Figure 30
Cross-sectional TEM, Bright Field, g_{220}

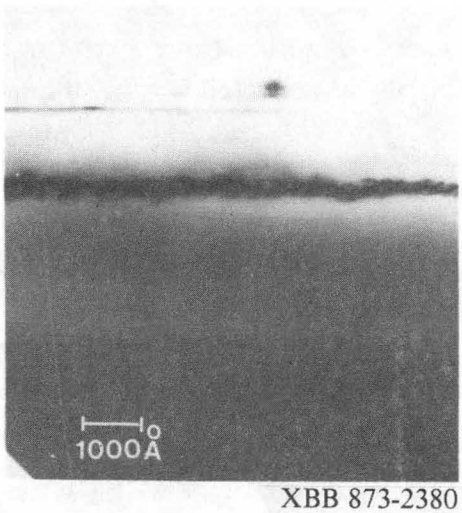

XBB 873-2380

Figure 31

50 keV P 1 x 10^{16}/cm^2, {100}
Annealed 900°C 8 minutes, Bright Field, g_{220}

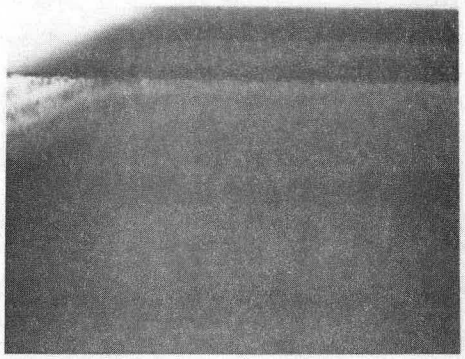

as-implanted

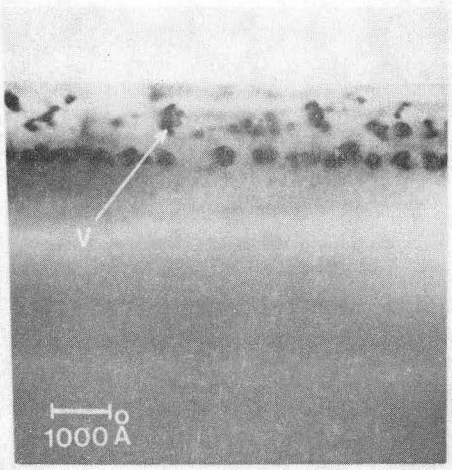

900°C 4 minutes

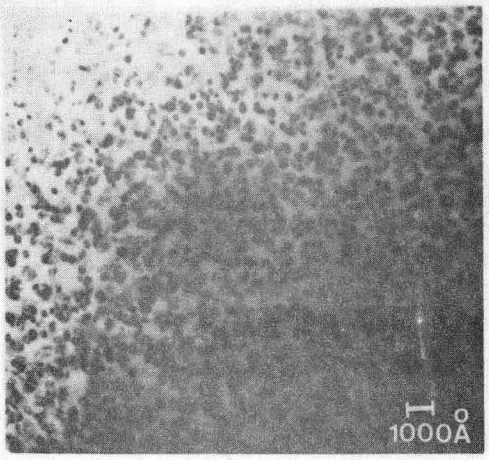

900°C 4 minutes

XBB 873-2381

Figure 32

100 keV ^{75}As 1 x 10^{16}/cm^2, {100}, Waycool Endstation
Bright Field, PTEM: g_{040}, XTEM: g_{220}

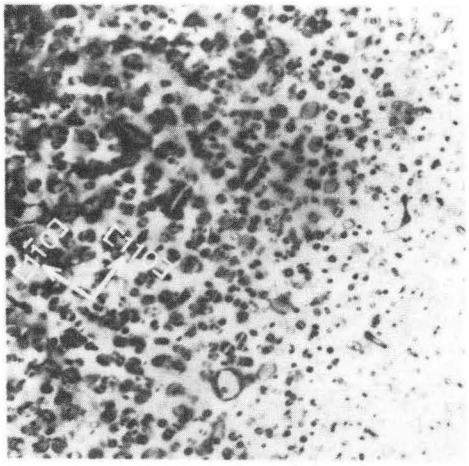

900°C 30 minutes

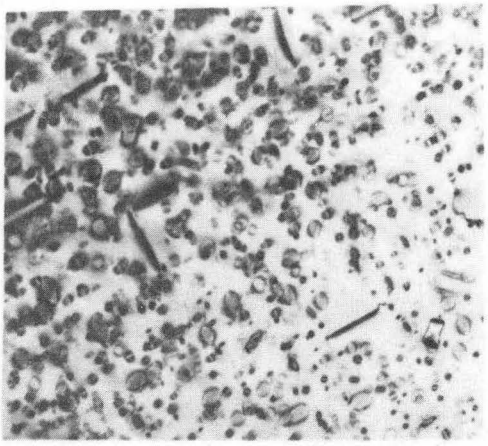

900°C 1 hour

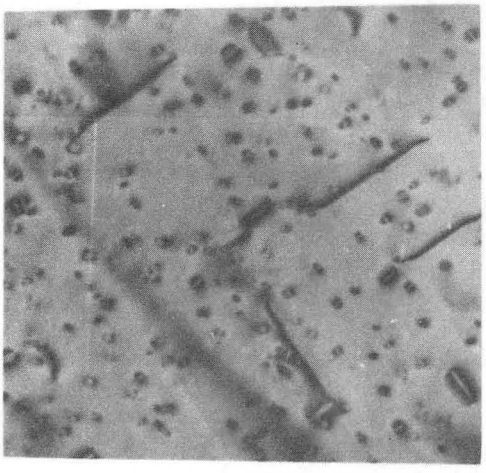

900°C 4 hours

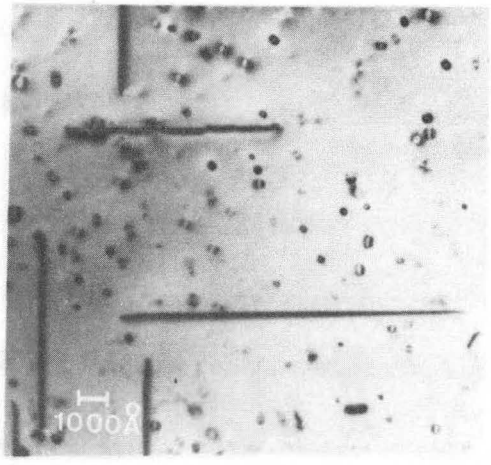

900°C 16 hours

XBB 873-2382

Figure 33

100 keV ^{75}As 1 x 10^{16}/cm^2, {100}
Bright Field g_{040}

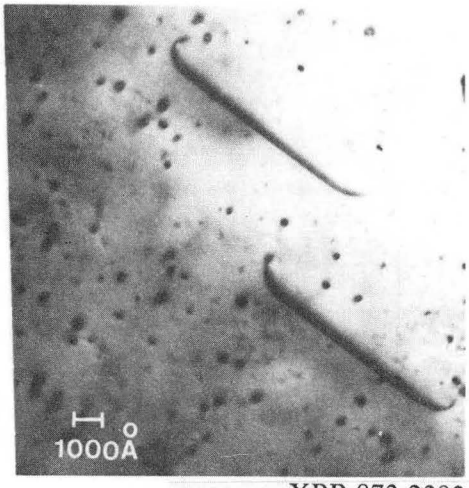

XBB 873-2383

Figure 34

Plan-view, Tilted ~35° from (001) pole, g_{111}
100 keV ^{75}As 1 x 10^{16}/cm^2, Annealed 900°C 16 hours

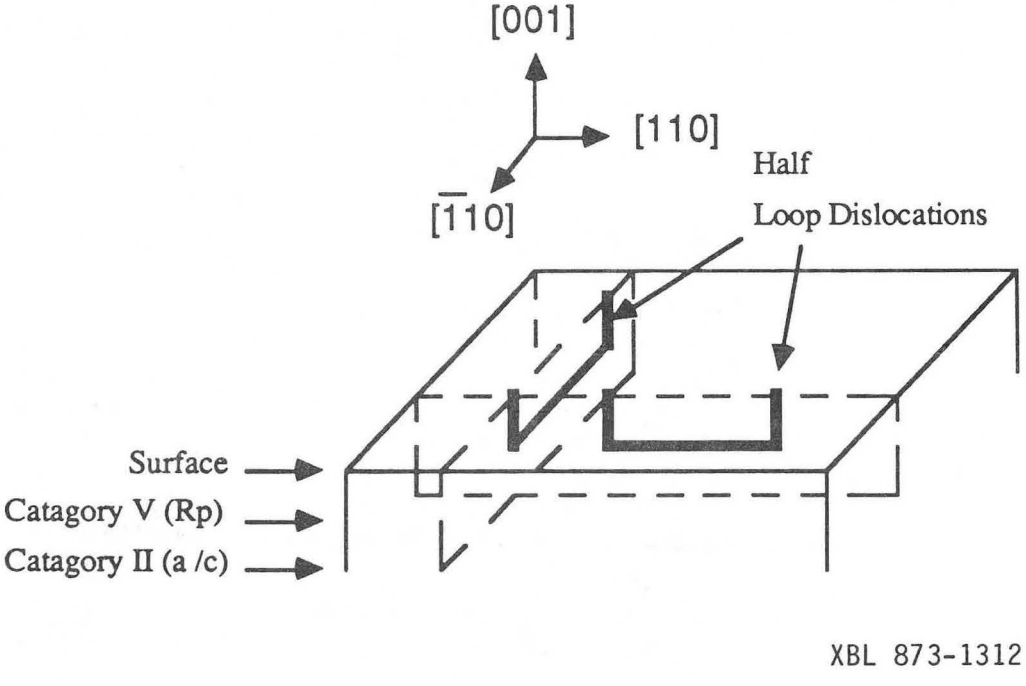

Figure 35

Half Loop Dislocation Orientational Relationship

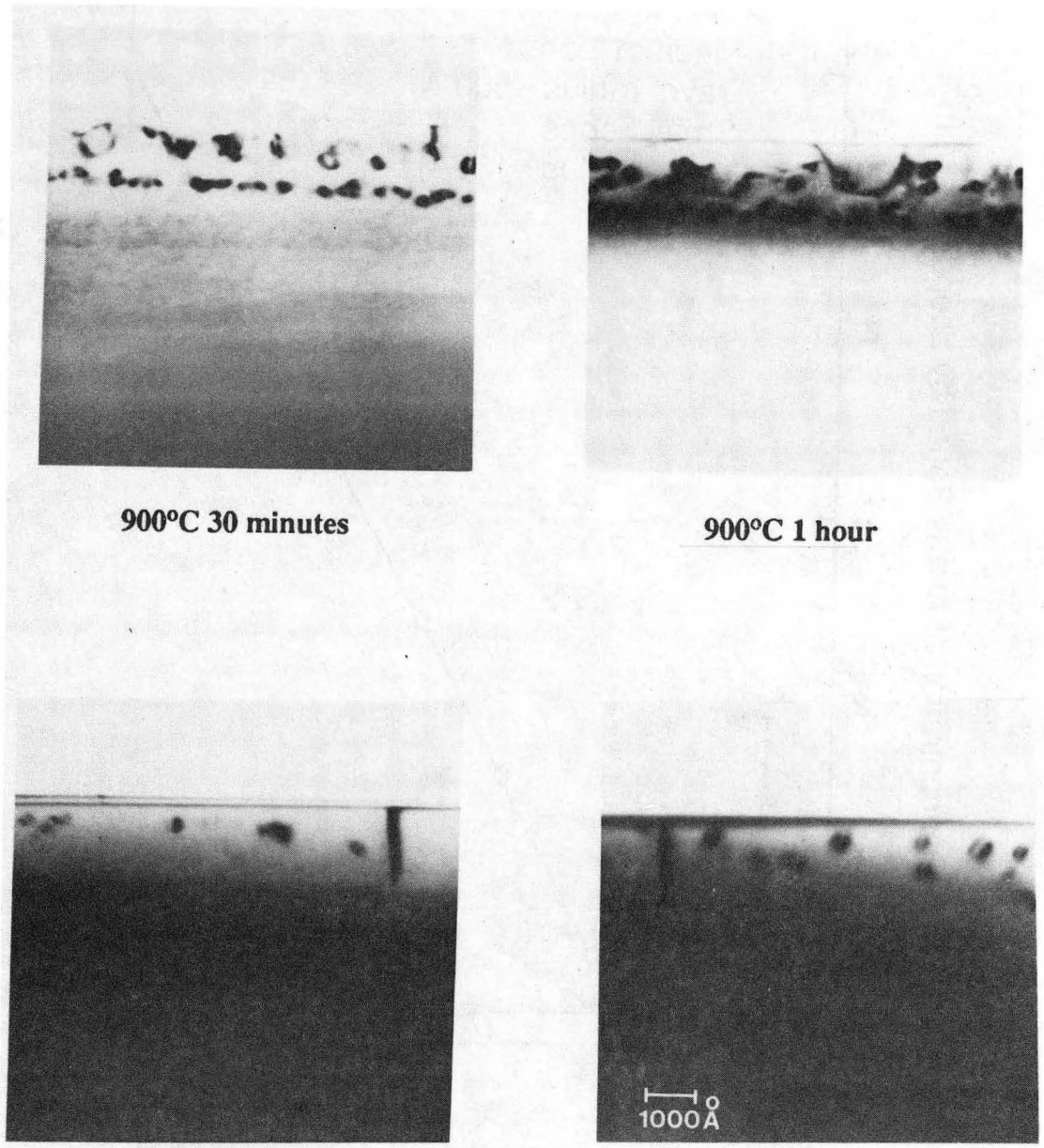

900°C 30 minutes

900°C 1 hour

900°C 4 hours

900°C 16 hours

XBB 873-2384

Figure 36

100 keV ^{75}As 1 x 10^{16}/cm^2, {100}
Bright Field g_{220}

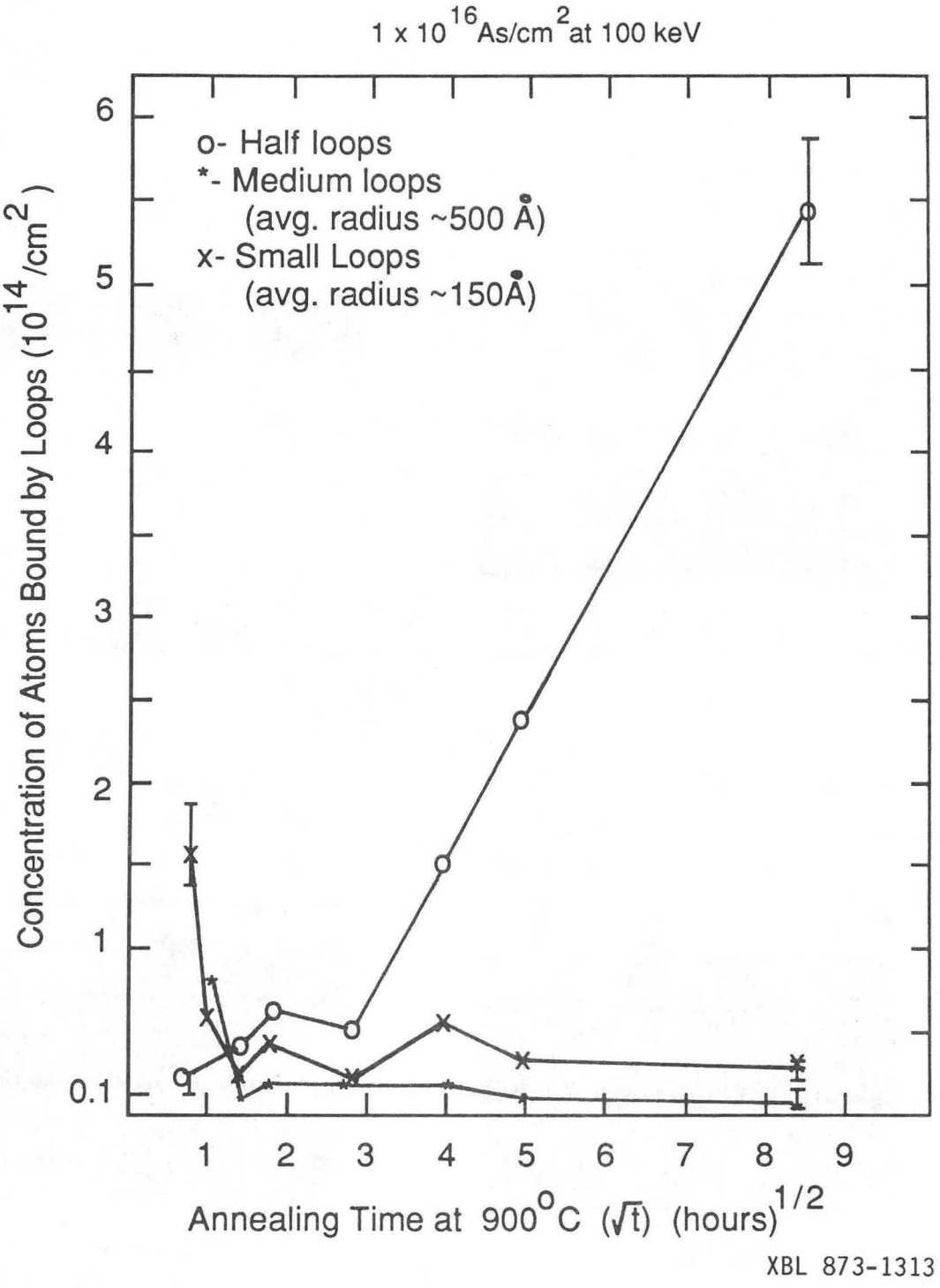

Figure 37

Concentration of Atoms bound by Dislocation Loops as a Function of Annealing Time

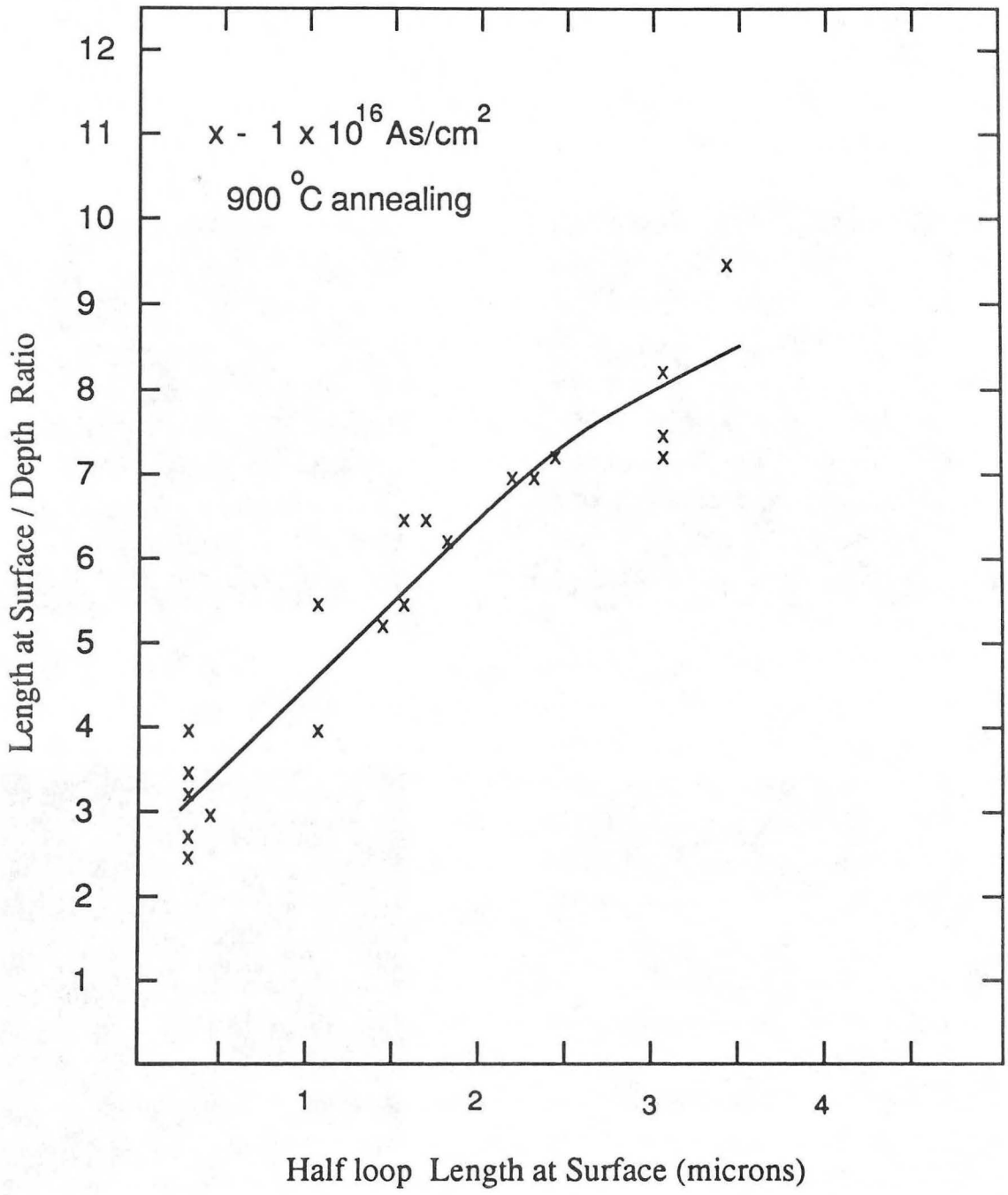

XBL 873-1314

Figure 38

Half Loop Dislocation Aspect Ratio as a Function of Size

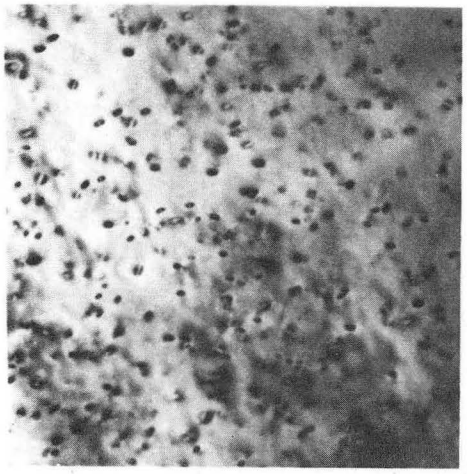

$5 \times 10^{14}/cm^2$

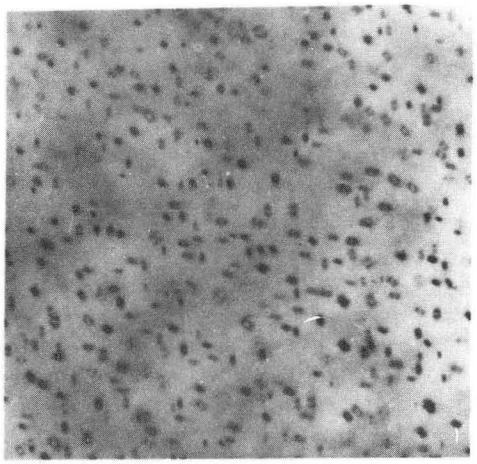

$2 \times 10^{15}/cm^2$

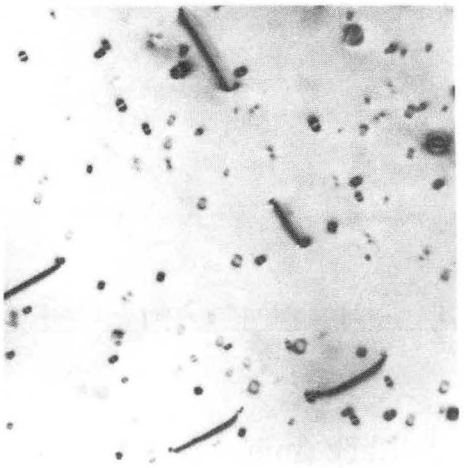

$5 \times 10^{15}/cm^2$

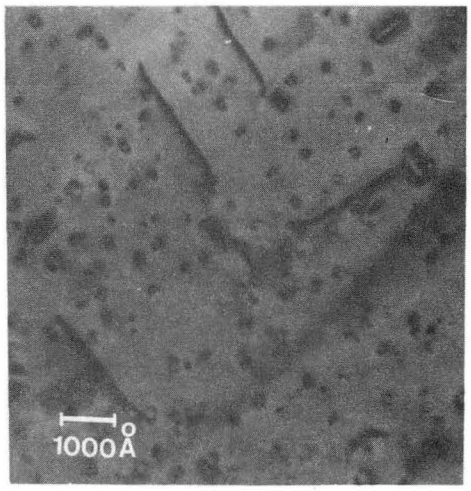

$1 \times 10^{16}/cm^2$

XBB 873-2385

Figure 39

100 keV ^{75}As, {100}, Annealed 900°C 4 hours
Bright Field, g_{040}

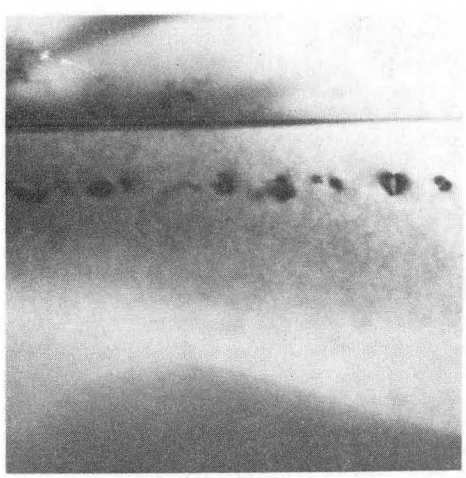

$2 \times 10^{15}/cm^2$

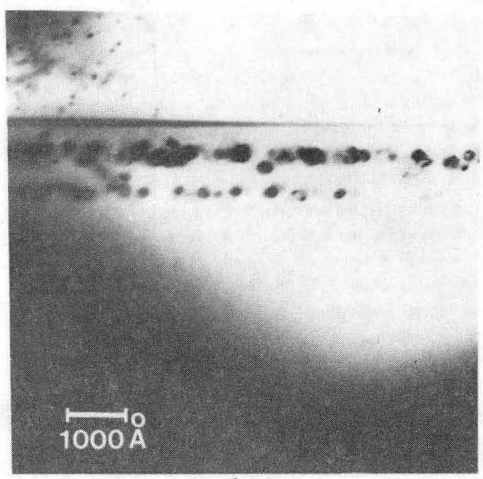

$5 \times 10^{15}/cm^2$

XBB 873-2386

Figure 40

100 keV ^{75}As, {100}, Annealed 900°C 1 hour, Bright Field, g_{220}

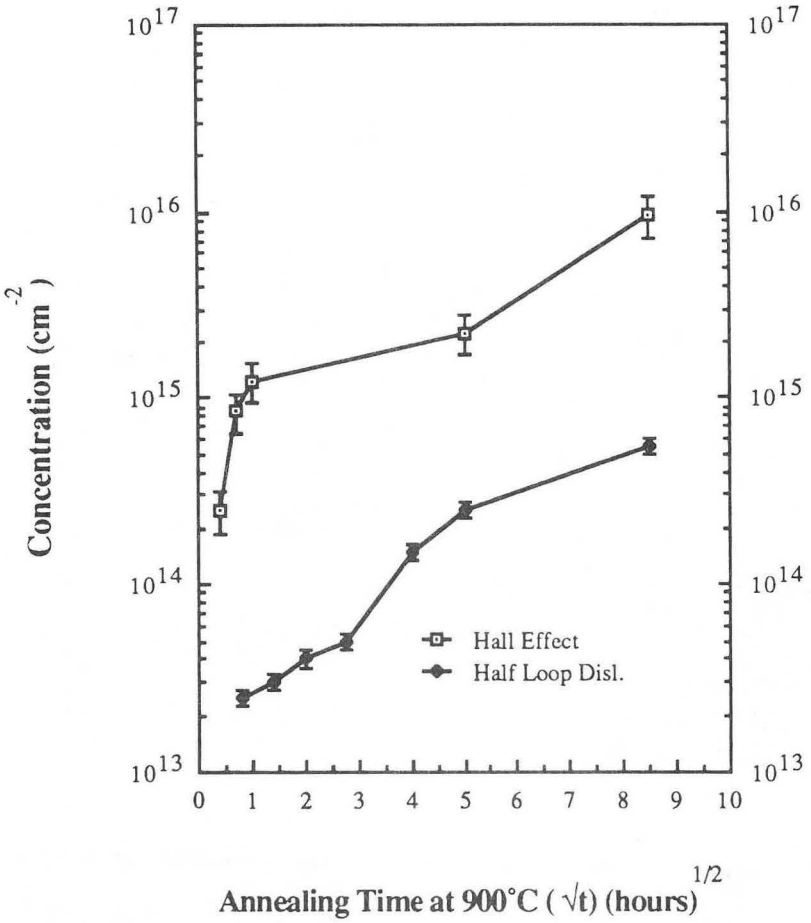

XBL 873-1315

Figure 41

Hall Effect Surface Carrier Concentration and Concentration of Atoms Bound by Half Loop Dislocations as a Function of Annealing Time

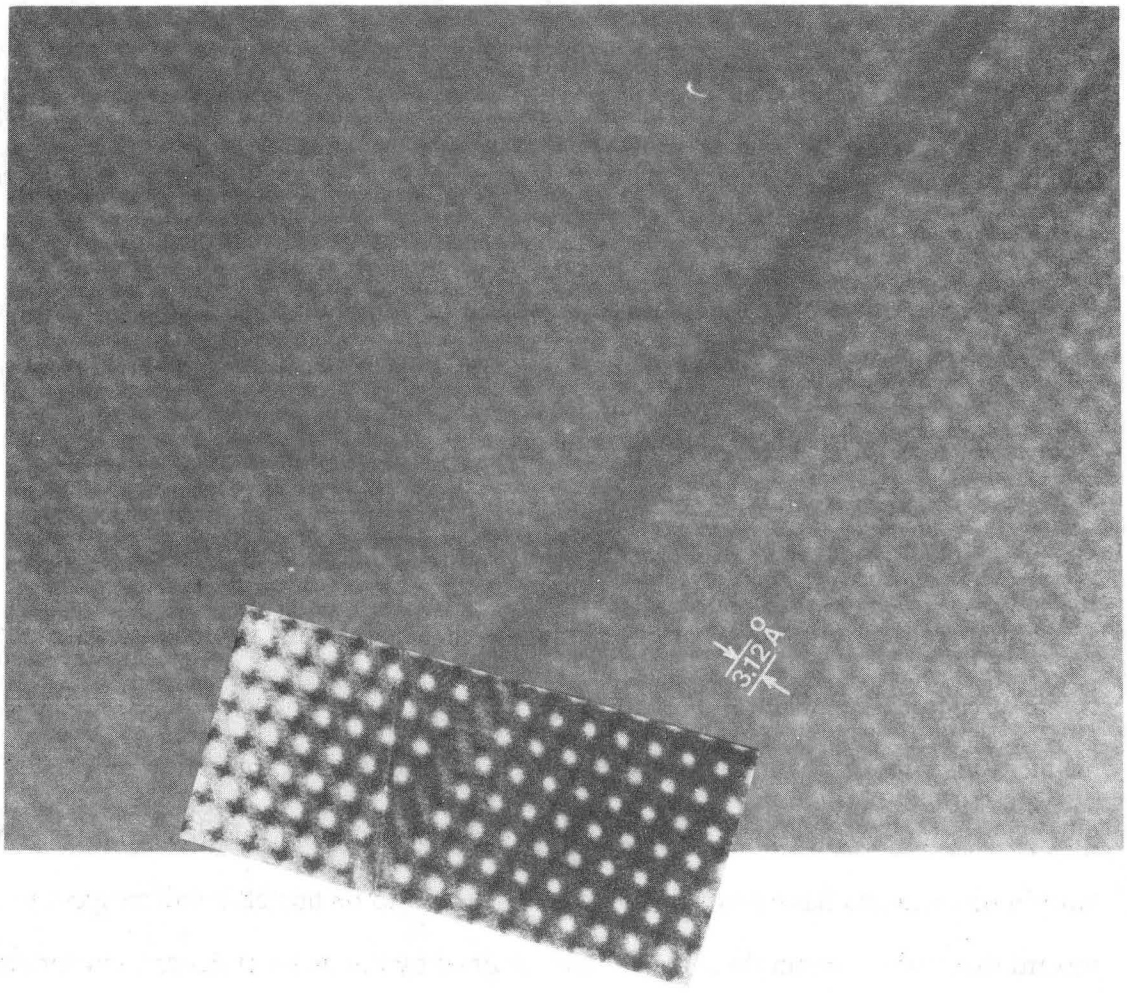

XBB 873-2387

Figure 42

Catagory V Defect

High Resolution TEM and
CEMPAS Computer Simulation of Arsenic Plate-Like Precipitate
100 keV ^{75}As 1 x 10^{16}/cm^2, Annealed 900°C 1 hour
Bright Field Multibeam Condition

4.6 Defect Stability

Most ion implantation damage can be avoided or reduced by adjusting the implant conditions. Category I damage can be avoided by either decreasing the dose below the critical level necessary for extended defect formation or by increasing the damage density above the threshold damage density thereby creating an amorphous layer. For the case of light ions such as B, implantation into a preamorphized substrate can be used to avoid category I damage. As stated, production of an amorphous layer leads to category II defects which are favored over category I damage for the following reasons. The concentration of category I damage is very dose dependent leading to network formation at doses above 2 x $10^{15}/cm^2$. Such networks are stable and difficult to eliminate by annealing. In addition, category I damage is believed to be associated with reverse annealing and may influence the high diffusivities observed with increasing dose.[165,199]

Category III microtwin defects can be avoided by using (100) wafers instead of (111) wafers as previously discussed. It may be possible to remove microtwins by a two step annealing cycle,[159] but our experience indicates that microtwins evolve into a dislocation tangle upon 900°C annealing. The category III hairpin dislocations can be avoided by using heavier ions (Ge) or low implant temperatures (77K) for preamorphization or VLTA (very low temperature annealing)[157,158] to remove the misoriented microcrystallites. When hairpin dislocations have formed they were observed to be unstable with respect to glide toward the surface within the glide cylinder defined by the inclined Burgers vector and the dislocation line direction.[137] The results in figure 24 indicate that hairpin dislocations are less stable than the category II damage at 900°C.

Category IV damage for low dose phosphorus implants (5 x $10^{14}/cm^2$) into {111} Si was relatively stable[112] after furnace annealing at 1050°C. Category IV defects were also stable for the lower dose (1 x $10^{15}/cm^2$) As implants in figure 24. However the same figure

shows that with increasing dose, the category IV defects like the category III defects are less stable than the category II defects. This dependence of the defect stability on the concentration of the implanted impurity is most pronounced when the impurity concentration is above solid solubility as will be discussed.

Category V defects are primarily precipitates. They occured when the solid solubility at the annealing temperature is lower than the peak concentration of the implanted species. With the exception of arsenic, category V defects were not observed to form extended defects other than the precipitates so, as expected, the dissolution of category V defects is very dependent upon the species implanted. The rate of growth or dissolution of precipitates can be limited either by long range diffusion away from the precipitate or transfer of atoms across the matrix-precipitate interface.[200] In the case of ion implantation, the diffusion of the impurity profile laterally will cause the peak of the concentration to drop below the solid solubility limit. Comparison of SIMS and carrier concentration measurements indicate that a plateau region exists in the carrier concentration profile around the projected range when the solid solubility is exceeded. The plateau dissappears as the peak concentration drops below the solid solubility with annealing and the total concentration of electrically active carriers increases. This implies that long range diffusion, not interfacial reactions, control the stability of the category V precipitates.

4.6.1 Enhanced Category II Dissolution

If an amorphous layer is produced, category II defects will form upon annealing. This is the one form of damage which cannot be avoided for implants resulting in an amorphous layer and, as stated, they are prefered over category I (subthreshold) defects. Thus, understanding the dissolution kinetics of category II defects is imperative for optimizing the production of shallow junction defect free contacts. Appendix 1 is a collection of micrographs which show the effect of annealing on category II damage for a number of species. All micrographs, except As, are of category II dislocation loops and category V

precipitates only. Figures 30 and 31 shows some of the corresponding cross-sectional TEM micrographs. Category II defects are thought to be composed primarily of Si atoms so their dissolution by positive climb is expected to be governed by self diffusion. For Si and Ge implants ,as well as low dose (well below solid solubility) implants of other species, the category II defects were observed to be stable. However, for some implant species where the solid solubility was exceeded, enhanced dissolution of the category II dislocation loops was observed [As, Ga and P (appendix 1e-g)]. For other species above solid solubility, a network of dislocations was observed to form (Al and Sb, appendix 1c,d). Understanding this phenomena could provide a processing means of rapidly dissolving category II defects. A number of different experiments have been conducted in an effort to better understand this enhanced dissolution phenomena.

4.6.1a Activation Energy for Defect Dissolution

It is possible to determine the activation energy for removal of the category II defects by producing an Arrhenius plot of the inverse of the time necessary to remove all category II defects versus the annealing temperature. In a recent paper, Seidel et.al.[201] report an activation energy of ~5 eV for removal of the category II defects in As implanted Si (figure 43). The energy and dose were such that the peak concentration exceeded the solid solubility for the annealing temperatures studied, indicating that category V defects were expected and, in fact, were observed.[202] Therefore, the 5 eV activation energy corresponds to the removal of category II loops only, not for the removal of category V defects. Our results for a higher dose As implant are also summarized in figure 43. An activation energy of ~5 ± 0.5 eV for removal of the category II dislocation loops was also found. The category V defects were observed to be unstable at 1100°C after 2 seconds thus, the higher temperature results of the Arrhenius curve reflect complete defect removal (category II and V). The slight shift in the y-intercept may not be significant within the error bars of the

experiment. The y-intercept or t_o reflects the concentration of vacancies or the magnitude of the interstitial sink which is enhancing the category II dislocation positive climb rate. With increasing dose, the value of t_o should increase to reflect the increased interstitial sink or vacancy source.

Similar Arrhenius plots were made for P and Ga implants above solid solubility and are shown in figure 44 along with the As data. An activation energy of ~5 ± 0.5 eV was observed for all of the species. If category II dislocation loops are composed primarily of Si atoms then the activation energy of 5 eV is explainable in the context of self diffusion away from the loops or diffusion of vacancies to the loops, as stated earlier. The shift in t_o is again questionable but may imply that P accelerates the defect dissolution slightly better than As when implanted at the same dose. Ga also accelerates the defect dissolution but at a much lower dose. For all Ga implant doses studied ($2 \times 10^{14}/cm^2$ to $1 \times 10^{15}/cm^2$), the peak of the impurity profile (~$3.6 \times 10^{19}/cm^3$ for $2 \times 10^{14}/cm^2$) exceeded the solid solubility of Ga in Si at the annealing temperatures (e.g. $2 \times 10^{19}/cm^3$ at 900°C) studied. The amount of data at different temperatures was limited for Ga and further studies are needed to determine accurately the activation energy. The results for Ga and P represent complete defect removal. This is because either no category V defects were observed (P) or the category V precipitates dissolved simultaneously with the category II dislocation loops (Ga). The observation that Ga enhanced the defect dissolution is one of the strong pieces of evidence relating this phenomena with exceeding the solid solubility and not the diffusion of the implanted impurity. The diffusivity of Ga ($4 \times 10^{-16} cm^2/s$) is between that of P (~$1 \times 10^{-15} cm^2/s$) and As ($8 \times 10^{-17} cm^2/s$) at 900°C. However, at a lower doses ($1 \times 10^{15}/cm^2$) where the peak concentrations are below the solid solubility both P and As category II defects were stable after 72 hours at 900°C (the longest time studied). In addition, there is

evidence that diffusion of P results in a supersaturation of interstitials[203-205] which would favor negative not positive climb of the category II loops. Also, a diffusion argument would suggest that Sb diffusion, which is believed to have a vacancy flux associated with it,[206] would favor the dissolution of the extrinsic category II dislocation loops which was clearly not observed.

When the solid solubility cannot be exceeded, as with Si and Ge implants, the category II defects were very stable. It was not possible to determine the activation energy for dissolution of the category II loops for these implants. The primary reason for this is that after 24 hours at 1075°C in dry N_2, which was the most extreme thermal cycling, the effect of residual oxidation overwhelmed any dissolution process and growth of faulted category II loops occured. The Ge results imply that a large biaxial compressive stress field in the implanted layer is not the reason for the enhanced category II loop dissolution. The stability of the category II defects for the Si implants implies that dissolution because of the thermodynamic instability of the dislocation loops is kinetically limited at these annealing temperatures.

4.6.1b Sheet Resistivity Measurements

As shown in appendix 1c and d, exceeding the solid solubility of the implanted species (Al and Sb) does not mean that enhanced dissolution of the category II defects will be observed. Under these annealing conditions, both Sb and Al implants resulted in formation of a network of dislocations rather than elimination of the defects. Sheet resistivity measurements were used to further study the role of precipitation on the observed enhanced category II defect dissolution rate. Figure 45 shows that, for doses below $1 \times 10^{15}/cm^2$, the sheet resistivity decreases proportional to the dose, as expected. However, when the dose increases above $1 \times 10^{15}/cm^2$ precipitation results in a saturation of the conductivity. At these higher doses, metallic precipitates were observed in the TEM samples. In order to understand why, upon annealing at 900°C, enhanced category II loop dissolution was

observed for Ga, P, and As implants but not for Sb implants, the sheet resistivity was measured as a function of annealing time (figure 46), for samples implanted above the solid solubility. For P, Ga, and As the precipitates were dissolving (sheet resistivity decreasing) during the process of enhanced dissolution of the category II loops. Precipitation was still occuring (sheet resistivity increasing) for the Sb implants. For Ga samples the metallic precipitates were physically observed, by TEM, to be dissolving (appendix 1f) however, no dissolution of the Sb precipitates was observed. These results imply that in addition to exceeding the solid solubility, the enhanced dissolution mechanism for category II defects requires the precipitates to be dissolving during the annealing process.

The question arises, if the flux of dopant atoms from the precipitates could somehow accelerate the category II dissolution, if the precipitates are dissolving. The surface of a low dose ($1 \times 10^{15}/cm^2$) Si^+ implanted sample, which had previously been annealed at 900°C for 30 minutes to form the category II loops (figure 14) was lightly oxidized ($t_{ox} < 400Å$). The results are shown in figure 47. The category II loops grow from injection of interstitials, as expected. Thus, the enhanced dissolution observed for the other implanted species is not related to a supersaturation of interstitials.

4.6.1c Model for Enhanced Dissolution

It is proposed, from the above evidence, that the enhanced dissolution observed for the extrinsic category II dislocation loops is a result of the release of vacancies or the generation of an interstitial sink during precipitation dissolution. Precipitation of SiP has been studied extensively by Bourret et al[207] for high concentration (exceeding the solid solubility) P predeposition into Si. Their results indicate that precipitation is an excellent source of interstitials. This would support our model that the dissolution of precipitates is a source of vacancies or is an interstitial sink.

For Ga implants, the volume occupied by the precipitates which were resolved by

TEM, could be filled by ~7 x $10^{13}/cm^2$ atoms if they occupied lattice sites and the concentration of atoms bound by the extrinsic dislocation loops was ~6 x $10^{13}/cm^2$. Since the precipitates and the category II dislocation loops were observed to dissolve simultaneously, this might be the means by which the enhanced dissolution occurs.

It should, in principle, be possible to derive the excess concentration of vacancies above the equilibrium concentration necessary for enhanced category II defect dissolution. This could be done by using the relationship:[184]

$$dr_{SF}/dt = -a_{eff}\, D_v\, C_v^{eq}\, [\, C_v/C_v^{eq} - \exp(-\Delta G/kT)]\, A/\Omega$$

where r_{SF} is the radius of the faulted dislocation loop, a_{eff} contains the factors related to interaction potentials and D_v is the self diffusion coefficient. C_v^{eq} is the equilibrium concentration of vacancies at the annealing temperature, C_v is the excess concentration of vacancies introduced by the dissolution of precipitates in our case. ΔG is the free enthalpy gained by removing an atom from the loop which, for larger stacking faults (dia > 10 μm) is dominated by the stacking fault energy. Unfortunately, ΔG is not accurately known for small faulted dislocation loops. A is the area of an atom in the faulted category II loop and Ω is the atomic volume.

A ratio of the shrinkage rate above and below solid solubility (S.S.) should be proportional to the ratio of the excess vacancies to the equilibrium concentration of vacancies:

$$\frac{dr_{SF}/dt\ (\text{above S.S.})}{dr_{SF}/dt\ (\text{below S.S.})} = \frac{C_v\ (\text{above S.S.})}{C_v\ (\text{below S.S.})} - 1$$

However, the shrinkage rates for category II loops in a system below solid solubility, of which a Si^+ implant is ideal, are indeterminant since some loops shrink while other loops grow. This makes it impossible to determine the actual concentration increase of vacancies, or the magnitude of the interstitial sink.

Based on the TEM studies of the different species at different doses and annealing temperatures, the sheet resistivity measurements, the oxidation results and what is known about the diffusivities of the different species as well as the tetrahedral covalent radii, it is concluded that the dissolution of clusters or category V precipitates greatly increases the rate at which category II defects dissolve.

The dissolution of category II defects needs to be correlated with diffusion studies if the optimum p-n junctions are to be produced. An important point made by Sedgwick[208] and Seidel et.al.[201] is that the activation energy for defect dissolution is greater than the activation energy for diffusion of the major dopants. Thus, effective removal of the defects with the minimum amount of dopant redistribution would occur at high temperatures for short times i.e. rapid thermal annealing (RTA). There is evidence that during RTA[199] and/or implantation above solid solubility,[177,178] transient enhanced diffusion occurs. By studying with SIMS, the same As implanted sample illustrated in figure 43 (above solid solubility) Seidel et. al.[201] showed that the activation energy for As diffusion was ~4 eV while, as stated, the activation energy for defect removal was ~5 eV. The observed diffusivity can be explained in the context of "normal" concentration enhanced diffusion. An additional point is that the maximum dissolution rates occur when the solid solubility is exceeded. These conditions can lead to formation of category V defects (especially for As implants). Our results indicate that the category V defects are very stable at 900°C after 72 hours but are unstable at 1100°C after 2 seconds. This implies that category V defects in As implanted Si have an even larger activation energy for dissolution than the category II defects. This may be related to the increasing solubility limit at higher temperatures. Thus,

in order to completely dissolve both the category V and category II defects for As implants, it is best to use rapid thermal processing conditions (1100°C, 2 seconds).

The correlation between the activation energy for diffusion and the activation energy for dissolution has only been done for one species, As. The discussion of transient enhanced diffusivities is still being actively addressed. It appears that a full understanding of the diffusivities observed cannot be made without correlating them with the defect annealing kinetics, since the point defects generated by the dissolution process may affect the dopant redistribution. Without an extensive SIMS investigation of the dopant (i.e. P, Ga) redistribution which occurs during the enhanced dissolution of category II defects, it is difficult to predict the amount of diffusion which will accompany the dissolution process. However, when combined with rapid thermal annealing, using conditions which support enhanced defect dissolution may provide a "window" for the production of defect free sub-micron p-n junctions.

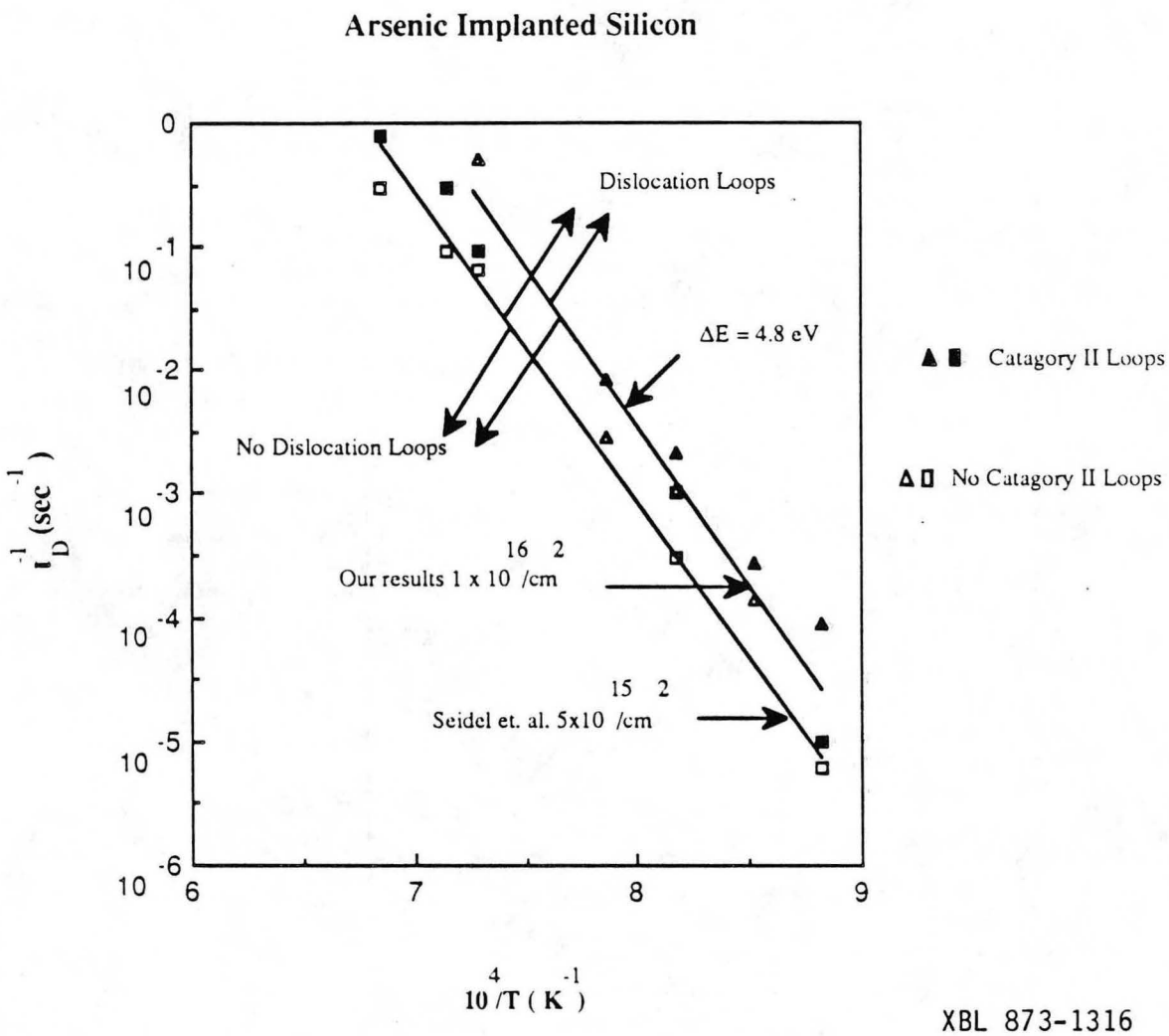

Figure 43

Arrhenius Curve for Arsenic Catagory II Dislocation Loop Dissolution, Peak Concentration Above Solid Solubility

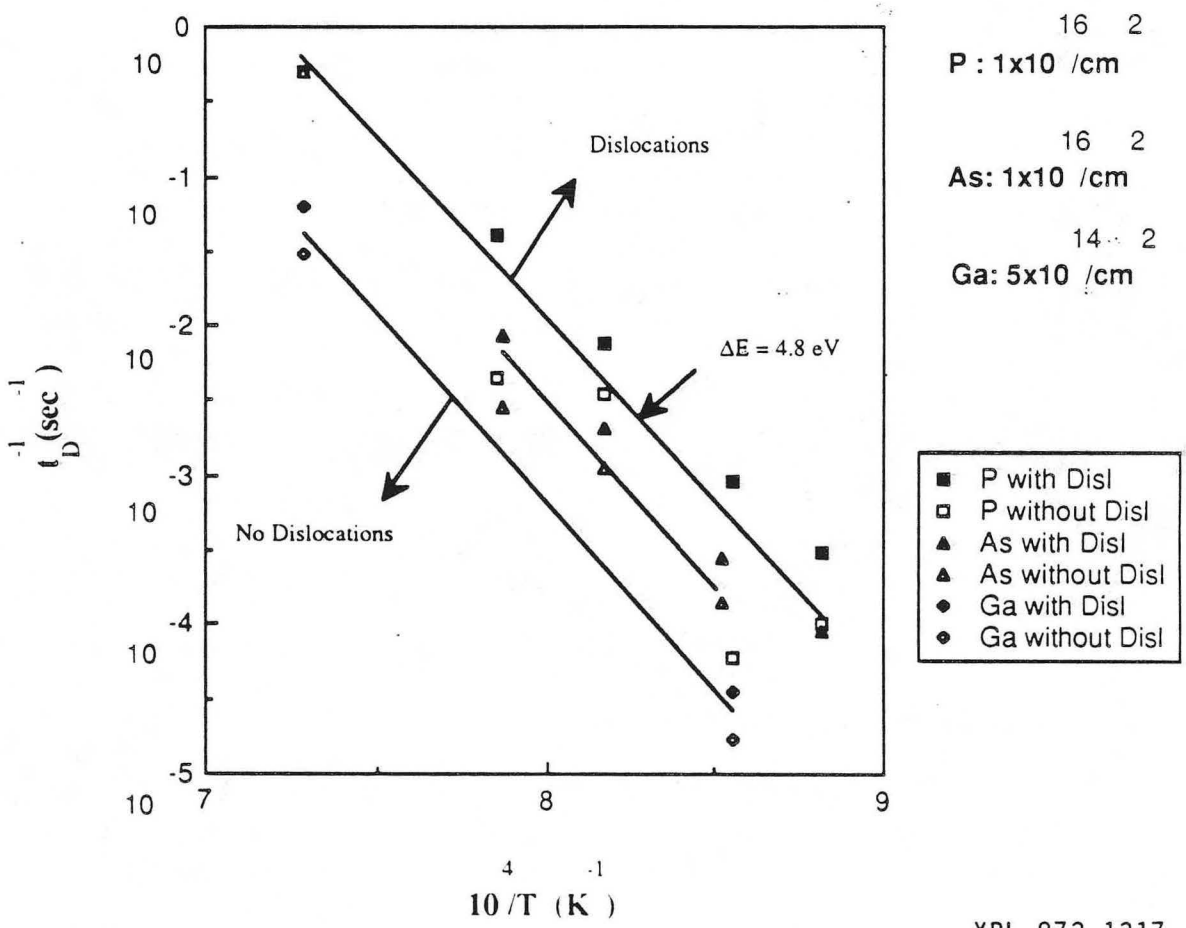

Figure 44

Ahrennius Curve for P, Ga, As Catagory II
Dislocation Loop Dissolution, Peak Concentration
Above Solid Solubility

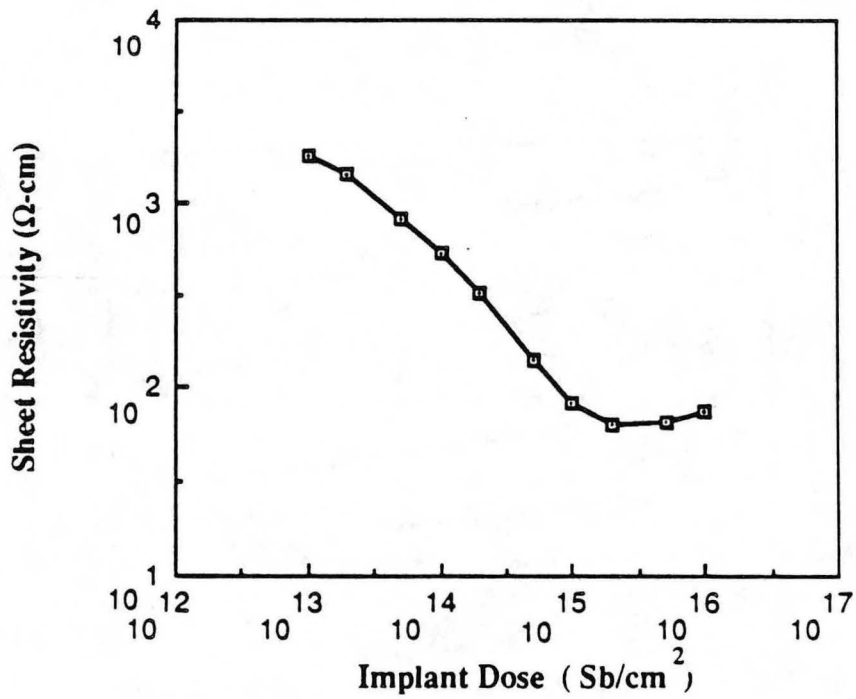

XBL 873-1318

Figure 45

Sheet Resistivity versus Implant Dose

190 keV ^{122}Sb, {100}, Waycool Endstation, Annealed 900°C 30 minutes

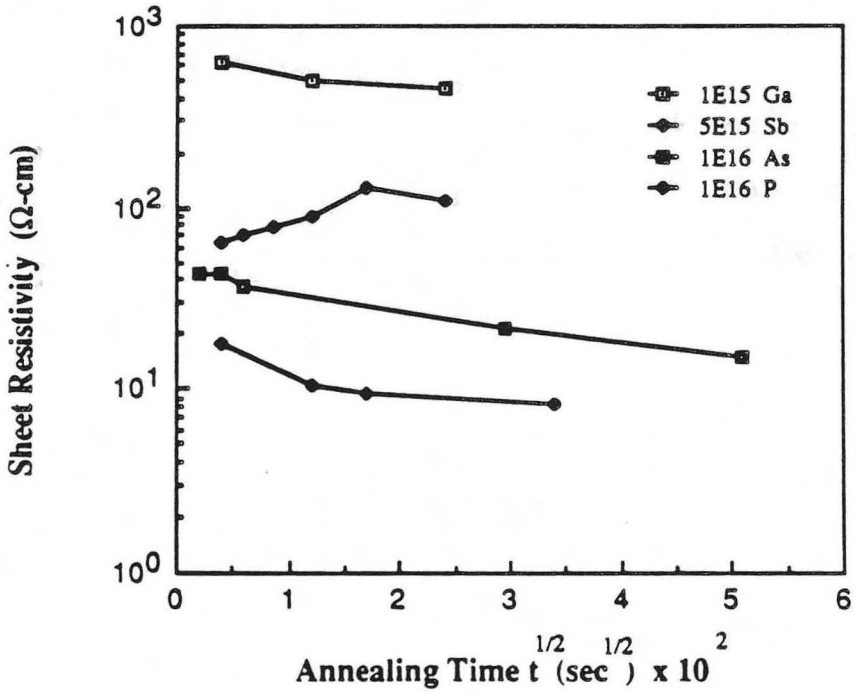

XBL 873-1319

Figure 46

Sheet Resistivity versus Annealing Time at 900°C

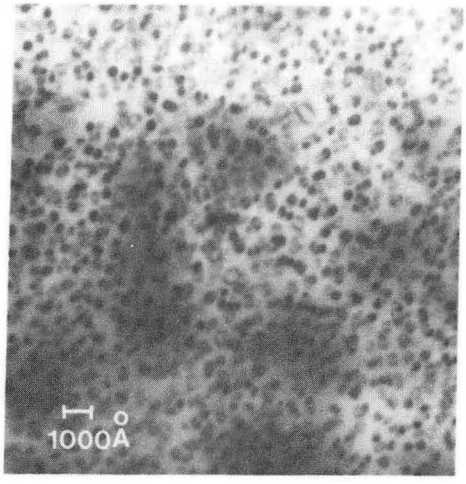

900°C 30 minutes
t_{ox} = 90Å

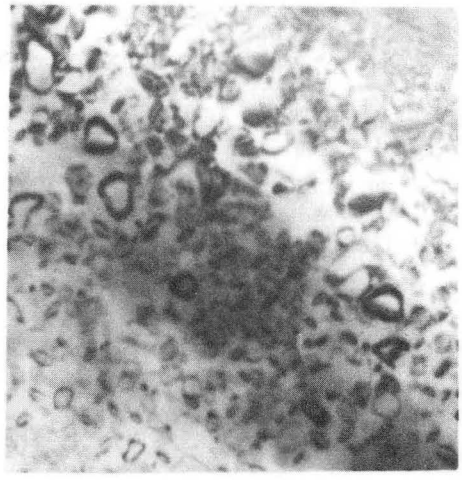

900°C 4 hours
t_{ox} = 343Å

50 keV ^{28}Si 2 x $10^{15}/cm^2$

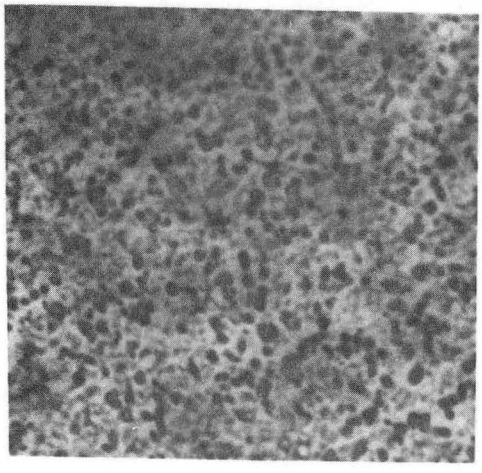

900°C 30 minutes
t_{ox} = 90Å

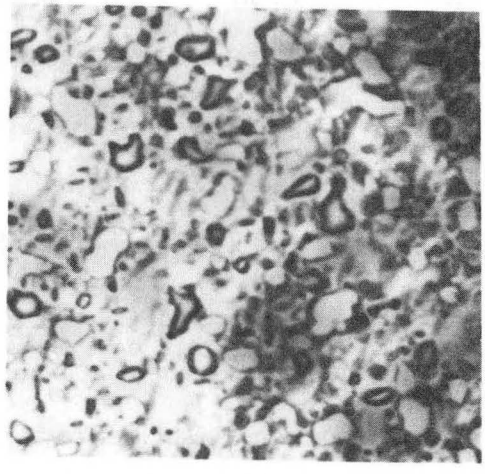

900°C 4 hours
t_{ox} = 343Å

50 keV ^{28}Si 1 x $10^{16}/cm^2$

XBB 873-2388

Figure 47

Oxidation of Catagory II Dislocation Loops
Dry O_2, Bright Field TEM g_{040}

5. CONCLUSIONS

A systematic study of the effect of implant species, dose and annealing conditions by both plan-view and cross-sectional TEM specimens has been made. Comparison of the as-implanted morphology with the defect structures which form upon annealing has led to the development of a classification scheme for extended defects associated with implantation damage. Combining our results with those reported in the literature, it was shown that all defects which form when ion implanted silicon is annealed, fall into one of the five categories of the classification scheme.

Several new models have been proposed based on these investigations of the effects of implant species, dose, annealing time and temperature, implantation temperature and pre- and post-amorphization on the defect structures which form upon annealing. There is evidence that the category I and II dislocation loops are extrinsic because of the increase in density of the lattice from implantation. Also, implantation of a pre-amorphized layer increases the amount of category II damage beyond the amorphous/crystalline interface (category II defects). Half loop dislocations, which have often been observed to form upon annealing high dose (≥ 5 x 1015/cm2) arsenic implants, are observed to nucleate from category V defects. Category V defects are associated with exceeding the solid solubility of the implanted species in silicon at the annealing temperature and are most often precipitates. The source of the point defects necessary for growth of the extrinsic half loop dislocations appears to be the dissolution of arsenic clusters and precipitates.

Finally, it was shown that all defects except category II (end of range) defects can be avoided at the higher doses necessary for low resistivity contacts. Enhanced dissolution of the category II defects was observed after <u>exceeding</u> the solid solubility of the implanted species in silicon and annealing in a time and temperature such that the precipitates are <u>dissolving</u>. The activation energy for this enhanced dissolution is ~5eV. The enhanced dissolution is <u>not</u> to be associated with diffusivity of the implanted species, stress from the implanted species occupying substitutional sites, injection of interstitials, or the

thermodynamic instability of the defects. A model involving the emission of vacancies or generation of an interstitial sink by the dissolving clusters or precipitates was proposed. Implantation with species which are completely soluble in silicon (i.e. silicon and germanium), or at doses such that the peak of the concentration profile is well below the solubility limit, or finally for species in which precipitates are not dissolving (antimony and aluminum) results in very stable category II defects. For phosphorus and gallium, the category V defects associated with exceeding the solid solubility either do not form or are unstable. Thus, upon annealing samples implanted with these species above solid solubility it is possible to produce defect free contacts after relatively low thermal cycling. Combining the enhanced dissolution conditions with rapid thermal annealing may provide a means of fabricating submicron, defect free low resistivity contacts suitable for VLSI technology.

The systematic study presented here has yielded numerous results for the determination of defect creation and annealing mechanisms arising from the process of ion implantation. In the areas where questions remain open, it is hoped that this study might serve as a foundation for more detailed work on those specific problems.

References

1. G. Carter and W.A. Grant, "Ion Implantation of Semiconductors", (Halstead Press, New York, NY), 1976.
2. G. Alvager and N.J. Hansen, Rev. Sci. Instrum., **33**, 567, 1962.
3. J.F. Ziegler, "Ion Implatation: Science and Technology", (Academic Press, New York, NY), 1984.
4. J.F. Gibbons, Proc. IEEE, 1062, Sept., 1972.
5. K.H. Nicholas, J. Phys. D.: Appl. Phys., **9**, 393,1976.
6. S. Prussin, private communication.
7. J. Washburn, G. Thomas and H.J. Queisser, J. Appl. Phys., **35**, 1909, 1964.
8. S. Prussin, J. Appl. Phys., **32**, 1876, 1961.
9. D.B. Holt, J. Phys. Chem. Solids, **27**, 1053, 1966.
10. E. Levine, J. Washburn and G. Thomas, J. Appl. Phys., **38**, 81, 1967.
11. M Watanabe, Y. Matsushita and K. Shibata, Inst. Phys. Conf. Ser. No. 59; ICDRES-11, Oiso, Japan, 123, 1980.
12. J. Fletcher and G.R. Booker, Electrochemical Society Proceedings, 1155, 1980.
13. K.H. Nicholas, J. Phys. D.: Appl. Phys., **9**, 393, 1977.
14. C. Bull, P. Ashburn, G.R. Booker and K.H. Nicholas, Sol. Sta. Electronics, **22**, 95, 1979.
15. M. Finetti, R. Galloni and M.Mazzone, J. Appl. Phys., **50**, 1381, 1979.
16. D.K. Sadana, J. Fletcher and G.R. Booker, Elect. Letters, **13**, 632, 1977.
17. P. Ashburn, C. Bull, K.H. Nicholas and G.R. Booker, S. St. Elect., **20**, 731, 1977.
18. J. Lindhard, M. Scharff and H.E. Schiott, Mat. Fys. Medd. Dan. Vid. Selsk., **33**, 1, 1963.
19. J.F. Gibbons, W.S. Johnson and S.W. Mylroie, "Projected Range Statistics", (Halstead Press, Stroudsburg, PA), 1975.
20. P. Sigmund, Appl. Phys. Lett., **14**, 114, 1969.

21. K.S. Jones, "Ion Implantation of Boron in Germanium", Lawerence Berkeley Laboratory Report-19615, 1985, p. 24.

22. D.K. Brice, "Ion Implantation Range and Energy Deposition Distribution", (Plenum Press, New York), **1**, 1975.

23. P. Sigmund and J.B. Sanders, Proc. Int. Conf. Appl. of Ion Beams to Semiconductor Technology, ed. P. Glotin (Centre d'Etudes Nucleaires, Genoble), 215, 1967.

24. B.L. Crowder and R.S. Title, "Proceedings 1st International Conference on Ion Implantation", eds. L.T. Chadderton and F.H. Eisen, (Gordon and Breach) 87, 1971.

25. S. Prussin, David I. Margolese and Richard N. Tauber, J. Appl. Phys. **57**, 180, 1985.

26. J. P. Biersack and L.G. Haggmark, Nucl. Inst. and Meth., **174**, 257, 1980.

27. J. F. Ziegler, J. P. Biersack and U. Littmark, " The Stopping and Range of Ions in Solids", (Pergamon Press, New York, NY), 1, 1984.

28. Hing Wong, private communication.

29. H.J. Geipel and W.K Tice, Appl. Phys. Lett., **30**, 325, 1977.

30. T.E.Seidel, R.L. Meek and A.G. Cullis, J. Appl. Phys., **46**, 600, 1975.

31. W.K. Tice and T.Y. Tan, "Defects in Semiconductors" eds. J. Narayan and T.Y. Tan, (North Holland Publishing, Amsterdam), 367, 1981.

32. H. Bender, Phys. Stat. Sol. (a), **86**, 245, 1984.

33. H.J. Geipel and W.K. Tice, Appl. Phys. Lett., **30**, 325, 1977.

34. T. Sands, J. Washburn, R. Gronsky, W. Maszara, D. K. Sadana and G.A. Rozgonyi, 13th Int. Conf. on Defects in Semiconductors, Coronado, 1984.

35. S. Prussin, David I. Margolese and Richard N. Tauber, J. Appl. Phys., **56**, 915, 1984.

36. W.K. Chu, M.R. Poponiak, E.I. Alessandrini and R.F. Lever, Rad. Eff., **49**, 23, 1980.

37. Y. Shih, "The Formation of Amorphous Si by Light Ion Damage", Ph. D. Dissertation, University of California, Berkeley, 1985.

38. D.E. Polk, J. Non-Cryst. Solids, **5**, 365, 1971.

39. W.H. Zachariasen, J. American Chem. Soc., **54**, 3841, 1932.

40. D.E. Polk and D.S. Bondreaux, Phys. Rev. Lett., **31**, 92, 1973.

41. S. Veprek, Z. Iqbal, H.R. Oswald, F.A. Sarott, J.J. Wagner and A.P. Webb, Solid. St. Comm., **39**, 509, 1981.

42. C. Kittel, "Introduction to Solid State Physics", 4th Edition, (Wiley Press, New York, NY), 1971.

43. K.P. Jain, A.K. Shukla, R. Ashokan, S.C. Abbi and M. Balkanski, Phys. Rev. B., **32**, 6688, 1985.

44. D. Kirillov, R.A. Powell and D.T. Hodul, Proceedings of Fall Mat. Res. Soc. Meeting, Symposium B, 1985.

45. S. Veprek, Z. Iqbal and F.A. Sarrott, Phil. Mag. B, **45**, 137, 1982.

46. M.H. Brodsky and R.S. Title, Phys. Rev. Lett., **23**, 581, 1969.

47. M.H. Brodsky, R.S. Title, K. Weiser and G.D. Pettit, Phys. Rev. B1, 2632, 1970.

48. J. Washburn, C.S. Murty, D.K. Sadana, P. Byrne, R. Gronsky, N. Cheung and R. Kilaas, Nucl. Inst. and Meth., **209**, 345, 1983.

49. J. Narayan, D. Fathy, O.S. Oen and O.W. Holland, Materials Letters, **2**, 211, 1984.

50. J. Washburn, C.S. Murty, D.K. Sadana, P. Byrne, R. Gronsky, N. Cheung and R. Kilaas, Int. Conf. on Ion Beam Modification of Materials, Grenoble, 1982.

51. J. Narayan, D. Fathy, O.S. Oen and O.W. Holland, J. Vac. Sci. Tech. **A2(3)**, 1303, 1984.

52. Z. Iqbal and S. Verprek, J. Phys. C., **15**, 377, 1982.

53. T. Kamiya, M. Kishi, A. Ushirokawa and T. Katoda, Appl. Phys. Lett., **38**, 377, 1981.

54. W.E. Spear, G. Willeke, P.G. LeComber and A.G. Fitzgerald, Physica B and C, **117-118**, 908, 1983.

55. H. Fritzsche, "Fundamental Physics of Amorphous Semiconductors", ed. F. Yonezawa, (Springer Verlag, New York, NY), 1, 1981.

56. G. Carter and W.A. Grant, "Ion Implantation of Semiconductors", (Halstead Press, New York, NY), 109, 1976.

57. F.F. Morehead, Jr. and B.L. Crowder, Rad. Eff. **6**, 27, 1970.

58. J.F. Gibbons, "Lectures on Ion Implantation and Proton Enhanced Diffusion", University of Tokyo, Tokyo, Japan, Jap. Soc. Appl. Phys., Aug, 1977.

59. Y. Shih, J. Washburn, E.R. Weber and R. Gronsky, Proceedings of the Materials Research Society, **45**, 65, 1985.

60. Kevin S. Jones, D. Sadana, S. Prussin, J. Washburn, E.R. Weber and W. Hamilton, J. Appl. Phys. in preparation.

61. F.F. Morehead, B.L. Crowder and R.S. Title, J. Appl. Phys., **43**, 1112, 1972.

62. H.J. Stein, F.L. Vook, D.K. Brice, J.A. Borders and S.T. Picraux, Rad. Eff., **6**, 19, 1970.

63. S. Prussin and Kevin S. Jones, "Materials Issues in Silicon Integrated Circuit Processing", eds. M. Strathman, J. Stimmel and M. Wittmer, Proc. Mat. Res. Soc., **71**, 1986.

64. J. Narayan and O.W. Holland, Phys. Stat. Sol. (a), **73**, 225, 1982.

65. Varian/Extrion Div. Gloucester, Mass. 01930.

66. B. Drosd and J. Washburn, J. Appl. Phys. **51**, 4106, 1980.

67. L. Cspregi, E.F. Kennedy, T.J. Gallagher, J.W. Mayer and T.W. Sigmon, J. Appl. Phys., **48**, 4234, 1977.

68. L. Cspregi, E.F. Kennedy, T.J. Gallagher, J.W. Mayer and T.W. Sigmon, J. Appl. Phys., **49**, 3906, 1978.

69. J. Washburn, "Defects in Semiconductors" eds. J. Narayan and T.Y. Tan, (North Holland Publishing, Amsterdam), 209, 1981.

70. S.S. Lau, J.Vac. Sci. Technol., **15**, 1656, 1978.

71. L. Csepregi, E.F. Kennedy, J.W. Mayer and T.W. Sigmon, J. Appl. Phys., **49**, 3906, 1978.

72. M. Tamura, K.Yagi, N. Sakudo, K. Tokiguti and T. Tokuyama, Rad. Eff. **48**, 109, 1980.

73. R. Drosd and J.Washburn, J.Appl. Phys., **53**, 397, 1982.

74. B.L. Crowder and F.F. Morehead, Appl. Phys. Lett., **14**, 313, 1969.

75. W.M. Lomer, Phil. Mag., **42**, 1327, 1951.

76. H.P. Fredrichs and S. Kalbitzer, Rad. Eff., **83**, 135, 1984.

77. C.E. Christodoulides, G. Carter and J.S. Williams, Rad. Eff., **48**, 87, 1980.

78. C. Carter, W. Maszara, D.K. Sadana, G.A. Rozgonyi, J. Liu and J. Wortman, Appl. Phys. Lett., **44**, 459, 1984.

79. S. Lau, J. Vac. Sci. Tech., **15**, 1656, 1978.

80. L. Csepregi, E.F. Kennedy, T. J. Gallagher, J.W. Mayer and T.W. Sigmon, J. Appl. Phys., **48**, 4234, 1977.

81. R.G. Elliman, J.S. Williams, D.M. Maher and W.L. Brown, Proceedings of Fall Mat. Res. Soc. Meeting, Symposium A, 1985.

82. F.F. Komarov, A.P. Novikov, T.T. Samoilyuk, V.S. Solov'yev and S.Yu. Shiryaev, Rad. Eff., **90**, 307, 1985.

83. J. Linnros and G. Holmen, Proceedings of Fall Mat. Res. Soc. Meeting, Symposium A, 1985.

84. T.Y. Tan, H. Foll and S.M. Hu, Phil. Mag. A, **44**, 127, 1981.

85. G.H. Kinchin and R.B. Pease, Rep. Prog. Phys., **18**, 2, 1955.

86. E.I. Alessandrini, W.K. Chu and M.R. Poponiak, "TEM Study of the Two-Stage Annealing of As implanted {100} Si", IBM Research Report. 1976.

87. D. Baither, R. Koegler, D. Panknin and E. Wieser, Phys. Stat. Sol. (a), **94**, 767, 1986.

88. L.C. Kimerling and J.L. Benton, "Laser and Electron Beam Proc. of Materials", eds. C.W. White and P.S. Pearcy, (Academic Press, New York, NY), 385, 1980.

89. D.K Sadana, M. Strathman, J. Washburn and G.R. Booker, J Appl. Phys., **52**, 744, 1981.

90. K. Seshan and J. Washburn, Phys. Stat, Sol. (a), **26**, 345, 1974.

91. R.B. Marcus and T.T. Sheng "Transmission Electron Microscopy of Silicon VLSI Circuits and Structures", (john Wiley and Sons, New York), 1983.

92. J.C. Bravman and R. Sinclair, "The Preparation of Cross-sectional Specimens for TEM", Dept. of Mat. Sci. and Eng., Stanford University, unpublished report, 1983.

93. P. Petroff and T.T. Sheng, Bell Telephone Laboratories Report, m.m. 73-2253-3, 1973.

94. D.K. Sadana and J. Washburn, Inst. Phys. Conf. Ser. No. 60, 301, 1981.

95. P.B. Hirsch, A. Howie and M.J. Whelan, Phil. Trans. Roy. Soc. London **A252**, 499, 1960.

96. A. Howie and M.J. Whelan,Proc. Roy. Soc. London **A263**, 217, 1961.

97. J.W. Edington, "Monographs in Practical Electron Microscopy in Materials Science", (The Macmillan Press Ltd., London), 1974.

98. G. Thomas and J. Washburn, Reviews of Modern Physics, **35**, 992, 1963.

99. G. Thomas and M.J. Goringe, "Transmission Electron Microscopy of Materials", (John Wiley and Sons, New York), 1979.

100. P.M. Kelly and R.G. Blake, Phys. Stat. Sol. (a), **25**, 599, 1974.

101. H. Foll and M. Wilkens, Phys. Stat. Sol. (a), **31**, 519, 1975.

102. D.J. Mazey, R.S. Barnes and A. Howie, Phil. Mag., **7**, 1861, 1962.

103. U. Dahmen, K.H. Westmacott and G.Thomas, Acta Met., **29**, 627, 1981.

104. P.B. Hirsch, A. Howie, R.B. Nicholson, D.W. Pashley and M.J. Whelan, "Electon Microscopy of Thin Crystals", (Butterworths, London), 263, 1965.

105. E. Levine, W.L. Bell and G.Thomas, J. Appl. Phys., **37**. 2141, 1966.

106. D.J.H. Cockayne, D. Phil. Thesis, University of Oxford.

107. A. Ourmazd, K. Ahlborn, K. Ibeh and T. Honda, Appl. Phys. Lett., **47**, 685, 1985.

108. Kevin S. Jones, S. Prussin and E.R. Weber, "Proceedings of the 14th International Conference on Defects in Semiconductors", ed. H.J. von Bardelben, Trans Tech Publications, Aedermannsdorf 1986 (Materials Science Forum Vol. 10), p. 751.

109. T.Y. Tan, Phil. Mag., **44**, 101, 1981.

110. T.Y. Tan, H. Föll and W.Krakow, Inst. Phys. Conf. Ser. No. 60, section 1, 1, 1981.

111. W. Krakow, T.Y. Tan and H. Foll, "Defects in Semiconductors" eds. J. Narayan and T.Y. Tan, (North Holland Publishing, Amsterdam), 185, 1981.

112. D.K. Sadana, J. Washburn and G.R. Booker, Phil. Mag. B. **46**, 611, 1982.

113. J. Narayan and J.Fletcher, "Defects in Semiconductors" eds. J. Narayan and T.Y. Tan, (North Holland Publishing, Amsterdam), 191, 1981.

114. H. Foll, T.Y. Tan and W. Krakow, "Defects in Semiconductors" eds. J. Narayan and T.Y. Tan, (North Holland Publishing, Amsterdam), 173, 1981.

115. M. Pasemann, D. Hoehl, A.L. Aseev and O.P. Pchelyakov, Phys. Stat.Sol. (a), **80**, 135, 1983.

116. H. Bartsch, D. Hoehl and G. Kastner, Phys. Stat. Sol. (a), **83**, 543, 1984.

117. I.G. Salisbury and M.H. Loretto, Rad. Eff., **59**, 59, 1981.

118. I.G. Salisbury and M.H. Loretto, Phil. Mag. A, **39**, 317, 1979.

119. C.A. Ferreira Lima and A. Howie, Phil Mag., **34**, 1057, 1976.

120. W.K. Wu and J. Washburn, J. Appl. Phys., **48**, 3742, 1977.

121. V.V. Kalinin and N.N. Gerasimenko, Phys. Stat. Sol. (a), **86**, 185, 1984.

122. J.C.H. Spence, "Experimental High Resolution Electron Microscopy", (Oxford Press, New York), 1980.

123. S.M. Davidson and G.R. Booker, "Proceedings of the 1st International Conference on Ion Implantation", eds. L.T. Chadderton and F.H. Eisen, (Gordon and Breach), 51, 1971.

124. S.M. Davidson, Proc. Of European Conf. on Ion Implantation (Reading, England), 238, 1970.

125. F.F. Komarov, V.S. Solovev, S. Yu. Shiryaev, Rad. Eff. Lett., **58**, 177, 1981.

126. J.J. Comer, Rad. Eff., **36**, 57, 1978.

127. V.V. Kalinin and N.N. Gerasimenko, Phys. Stat. Sol. (a), **76**, 65, 1983.

128. L.J. Chen and I.W. Wu, J. Appl. Phys., **52**, 3310, 1981.

129. S. Mader, "Ion Implatation: Science and Technology", ed. J.F. Ziegler, (Academic Press, New York, NY), 109, 1984.

130. I.W. Wu and L.J. Chen, J. Appl. Phys., **58**, 3032, 1985.

131. R.W. Bicknell, Proc. Of European Conf. on Ion Implantation (Reading, England), 57, 1970.

132. L.D. Glowinski, K.N. Tu and P.S. Ho, Appl. Phys. Lett., **28**, 312, 1976.

133. D.K. Sadana, J. Washburn, M. Strathman, M. Current and M. Maenpaa, Inst. Phys. Conf. Ser. No. 60, section 9, 453, 1981.

134. W.K. Chu, M.R. Poponiak, E.I. Alessandrini and R.F. Lever, Rad. Eff., **49**, 23, 1980.

135. S. Albin, R.Lambert, S.M. Davidson and M.I.J. Beale, Inst. Phys. Conf. Ser. No. 67, section 4, 241, 1983.

136. D.K. Sadana, J. Washburn and C.W. Magee, J. Appl. Phys., **54**, 3479, 1983.

137. O. Scherzer, Journal of Applied Physics, **20**, 20, 1949.

138. D.K Sadana, N.R. Wu, J. Washburn, M. Current, A. Morgan, D.Reed and M. Maenpaa, Nucl. Inst. and Meth., **209-210**, 743, 1983.

139. K Sumino and M. Imai, Phil. Mag. A, **47**, 753, 1983.

140. C.F. Cerofolini, L. Meda, M.L. Polignano, G. Ottaviani, H. Bender, C. Claeys, A. Armigliato and S. Solmi, "Semiconductor Silicon", Proc. of Electrochemical Society, (ECS Press, Pennington N.J.) 1986.

141. N.R. Wu, P.Ling, D.K. Sadana, J. Washburn and M.I. Current, "Defects in Silicon" Proc. of the Electrochemical Society, eds. W.M. Bullis and L.C. Kimerling, (ECS Press, Pennington N.J.) **83-9**, 366, 1983.

142. M. Nemiroff and V.S. Speriosu, J. Appl. Phys., **58**, 3735, 1985.

143. L.D. Glowinski, K.N. Tu and P.S. Ho, Appl. Phys. Lett., **28**, 312, 1976.

144. K.N. Tu, S.I. Tan, P. Chaudhari, K. Lai and B.L. Crowder, J. Appl. Phys. **43**, 4262, 1972.

145. M.H. Brodsky, R.S. Title, K. Weisser and G.D. Pettit, Phys. Rev. B1, 2632, 1969.

146. S.B. Felch and R.A. Powell, Proc. 6th Int. Conf. on Ion Implantation Technology, Berkeley, Nucl. Inst. and Meth. in Phys. Res., section B, Beam Interaction with Materials and Atoms, 1986, in print.

147. M.Y. Tsai and B.G. Streetman, J. Appl. Phys., **50**, 183, 1979.

148. W. Maszara, C. Carter, D.K. Sadana, J. Liu, V. Ozguz, J. Wortman and G.A. Rozgonyi, Mat. Res. Soc. Symp. Proc. Vol. **23**, 285, 1984.

149. W.K. Hofker, W.J.M. Josquin, D.P. Oosthoek and J.R.M. Gijsbers, Rad. Eff. **47**, 183, 1980.

150. M.Servidori and I. Vecchi, Solid State Electronics, **24**, 329, 1981.

151. S.T. Picraux, W.H. Weissenberger and F.L. Vook, "Proceedings of the 1st International Conference on Ion Implantation", eds. L.T. Chadderton and F.H. Eisen, (Gordon and Breach), 411, 1971.

152. H. Leibel, J.Vac. Sci. Tech., **12**, 385, 1975.

153. D.K. Sadana, W. Maszara, J.J. Wortman, G.A. Rozgonyi and W.K. Chu, J. Electrochem. Soc., **131**, 943, 1984.

154. T.E. Seidel, R. Knoell, F.A. Stevie, G. Poli and B. Schwartz, "Proc. of the Electrchemical Society, VLSI Science and Technology", eds. K.E. Beale and G.A. Rozgonyi, (ECS Press, Pennington N.J.)1984.

155. D.K. Sadana, E. Myers, J.Liu, T. Finstad and G.A. Rozgonyi, Mat. Res. Soc. Symp. Proc. Vol. **23**, 303, 1984

156. G.F. Cerofolini, L. Meda, G. Queirolo, A. Armigliato, S. Solmi, F. Nava and G. Ottaviani, J. Appl. Phys, **56**, 2981, 1984.

157. G.A. Rozgonyi, E. Myers and D.K. Sadana, "Semiconductor Silicon", Proc. of Electrochemical Society, (ECS Press, Pennington N.J.) 1986.

158. E. Myers, G.A. Rozgonyi, D.K. Sadana, W. Maszara, J.J. Wortman and J. Narayan, Proc. Mat. Res. Soc. Fall Meeting, Symp. B, 1985.

159. Y. Shih, J. Washburn and S.C. Shatas, SPIE Vol. 463 Advanced Semiconductor Processing and Characterization of Electronic and Optical Materials, 93, 1984.

160. H. Muller, W.K. Chu, J. Gyulai, J.W. Mayer, T.W. Sigmon and T.R. Cass, Appl. Phys. Lett., **26**, 293, 1975.

161. M.D. Rechtin, P.P. Pronko, G. Foti, L. Csepregi, E.F. Kennedy and J.W. Mayer, Phil. Mag. A, **37**, 605, 1978.

162. P.P. Pronko, M.D. Rechtin, G. Foti, L. Csepregi, E.F. Kennedy and J.W. Myer, "Ion Implantaion in Semiconductors, 1976", eds. F. Chernow, J.A. Borders and D.K. Brice, (Plenum Press, New York, NY), 503, 1977.

163. M.I.J. Beale and G.R. Booker, Inst. Phys. Conf. Ser. No. 67, Section 4, 235, 1983.

164. F.F. Komarov, V.S. Solov'yev and S. Yu. Shiryayev, Rad. Eff., **42**, 169, 1979.

165. P.I. Gaiduk, F.F. Komarov, V.A. Pilipenko, V.S. Solov'yev and N.I. Sterzhanov, Rad. Eff. Lett., **86**, 213, 1984.

166. J. Narayan, J.Appl. Phys, **53**, 8607, 1982.

167. M. Tamura, Phil. Mag., **35**, 663, 1977.

168. T. Sands, J. Washburn, R. Gronsky, W. Maszara, D.K. Sadana and G.A. Rozgonyi, Appl. Phys. Lett., **45**, 982, 1984.

169. T. Sands, J. Washburn, E. Myers and D.K. Sadana, Nucl. Inst. and Meth. in Phys. Res. **B7/8**, 337, 1985.

170. S. Prussin, David I. Margolese and Richard N. Tauber, J. Appl. Phys., **54**, 2316, 1983.

171. B.J. Masters, J.M. Fairfield and B.L. Crowder, Rad. Eff., **6**, 57, 1970.

172. D.K. Sadana, J. Fletcher and G.R. Booker, Elect. Lett., **13**, 631, 1977.

173. D.K. Sadana, M. Strathman, J. Washburn and G.R. Booker, J. Appl. Phys. **51**, 5718, 1980.

174. Kevin S. Jones and S.Prussin, "Materials Issues in Silicon Integrated Circuit Processing", eds. M. Strathman, J. Stimmel and M. Wittmer, Proc. Mat. Res. Soc., Vol. 71, 1986.

175. J. Fletcher, J. Narayan and O.W. Holland, Inst. Phys. Conf. Ser. No. 60, Section 1, 295, 1981.

176. S.J. Pennycook and R.J. Culbertson, "Transient Thermal Processing" eds. T. Sedgwick, T. Seidel and B.Y. Tsaur, (Materials Research Society, Pittsburgh, PA), 1986, in print.

177. S.J Pennycook, R.J. Culbertson and J. Narayan, Journal of Materials Research, 1986.

178. S.J. Pennycook, J. Narayan and O.W. Holland, J. Electrochem. Soc.: Solid-State Science and Technology, **132**, 1962, 1985.

179. S.M. Hu, "Defects in Semiconductors", eds. J. Narayan and T.Y. Tan, (North Holland, New York, Oxford), 333, 1981.

180. A. Kamgar, F.A. Baiocchi and T.T. Sheng, Appl. Phys. Lett., **48**, 1090, 1986.

181. N.R. Wu, D.K Sadana and J. Washburn, Appl. Phys, Lett., **44**, 782, 1984.

182. D.K. Sadana, M.H. Norcott, R.G. Wilson and U. Dahmen, Appl. Phys. Lett., **49**, 1169, 1986.

183. A. Lietoila, R.B. Gold, J.F. Gibbons, T.W. Sigmon, P.D. Scovell and J.M. Young, J. Appl. Phys. **52**, 230, 1981.

184. U. Gosele aand W. Frank, "Defects in Semiconductors", eds. J. Narayan and T.Y. Tan, (North Holland, New York, Oxford), 55, 1981.

185. S. Mader and A.E. Michel, J. Vac. Sci. Technol., **13**, 391, 1976.

186. S. Mader and A.E. Michel, Phys. Stat. Sol. (a), **33**, 793, 1976.

187. S. Mader, J. Electronic Materials, **9**, 963, 1980.

188. R.S. Barnes, Acta Met., **2**, 380, 1954.

189. N.R. Wu, P. Ling, D.K. Sadana, J. Washburn and M.I. Current, "Defects in Silicon", Electrochemical Society Proceedings Vol. **83**, eds. W.M. Bullis and L.C. Kimerling, (Electrochemical Society, Pennington, NJ), 363, 1983.

190. K.V. Ravi, "Imperfections and Impurities in Semiconductor Silicon", (John Wiley and Sons, New York, NY), 130, 1981.

191. F.A. Trumbore, Bell Syst. Tech. J., **39**, 210, 1962.

192. M. Hansen and K. Anderko, "Constitution of Binary Alloys", (McGraw-Hill, New York, NY), 1958.

193. R.W. Olesinski and G.J. Abbaschian, Bulletin of Alloy Phase Diagrams, **6**, 254, 1985.

194. E.R. Weber, Appl. Phys. A, **30**, 1, 1983.

195. D.A. Ackland, U. Dahmen, C.J. Echer, R. Kilaas, K.M. Krishnan, C. Nelson, M.A. O'Keefe, W. Smith and J. Turner, Journal of Metals, **38**, 19, 1986.

196. P. Pirouz, Phil. Mag. A, **41**, 33, 1980.

197. R.O. Schwenker, E.S. Pan and R.F. Lever, J. Appl. Phys, **42**, 3195, 1971.

198. R.B. Fair and G.R. Weber, J. Appl. Phys., **44**, 273, 1973.

199. A.E. Michel, Proc. Mat. Res. Soc. Fall Meeting, Symp. B, 1985.

200. F.V. Nolfi, Jr., P.G. Shewmon and J.S. Foster, Transactions of the Met. Soc. of AIME, **245**, 1427, 1969.

201. T.E. Seidel, D.J. Lischner, C.S. Pai, R.V. Knoell, D.M. Maher and D.C. Jacobson, Nucl. Inst. and Meth. in Phys. Res. **B7/8**, 251, 1985.

202. T.E. Seidel, private communication.

203. C.L. Jones and A.F.W. Willoughby, J. Electrochem. Soc.: Solid-state Science and Technology, **123**, 1531, 1976.

204. C.L. Jones and A.F.W. Willoughby, J. Electrochem. Soc.: Solid-state Science and Technology, **122**, 1531, 1975.

205. W. Frank, A. Seeger and U. Göesele, "Defects in Semiconductors", eds. J. Narayan and T.Y. Tan, (North Holland, New York, Oxford), 31, 1981.

206. S. Mizuo and H. Higuchi, Mat. Res. Soc. Symp. Proc. Vol. **36**, 125, 1985.

207. A. Bourret and W. Schroter, Ultramicroscopy, **14**, 97, 1984.

208. T.O. Sedgwick, J. Electrochem. Soc. **130**, 484, 1983.

Appendix 1a

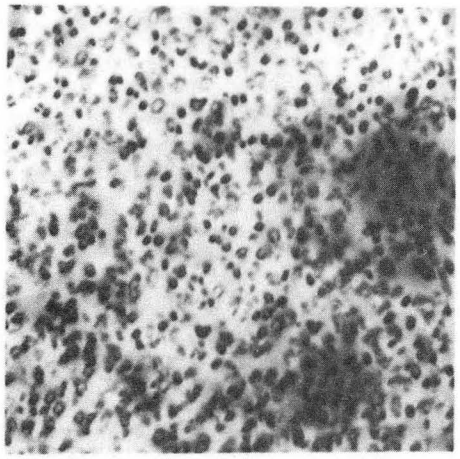

1 x 10^{15}/cm^2
900°C 30 minutes

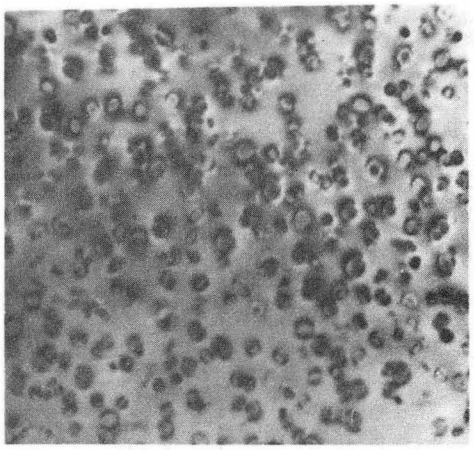

1 x 10^{15}/cm^2
900°C 8 hours

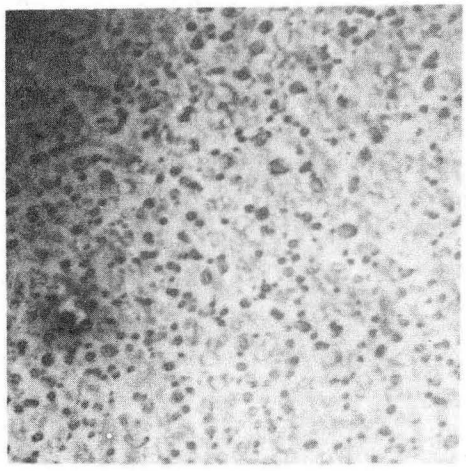

1 x 10^{16}/cm^2
900°C 30 minutes

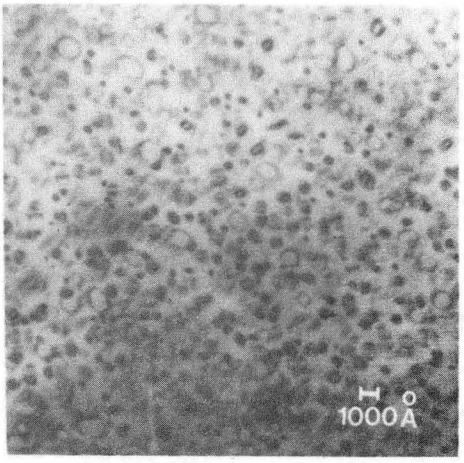

1 x 10^{16}/cm^2
900°C 8 hours

50 keV ^{28}Si, {100}, Waycool Endstation
Bright Field, g_{040}

XBB 873-2389

Appendix 1b

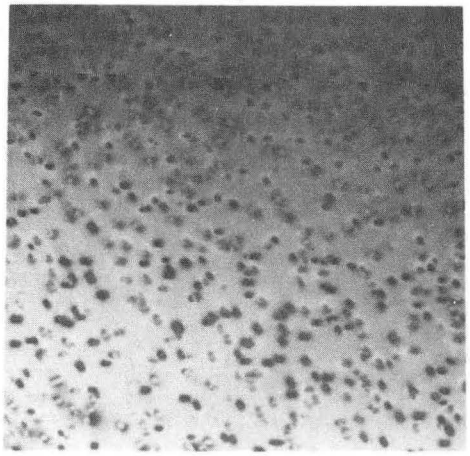

$1 \times 10^{15}/cm^2$
900°C 30 minutes

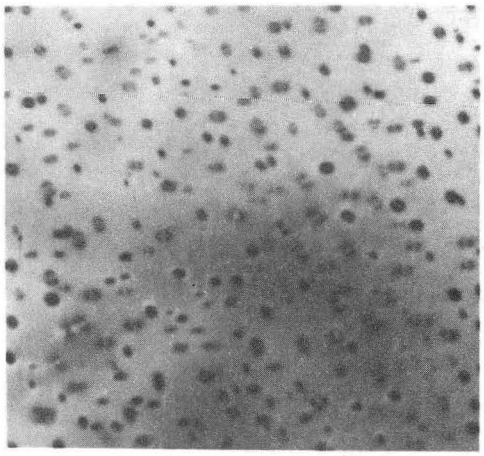

$1 \times 10^{15}/cm^2$
900°C 8 hours

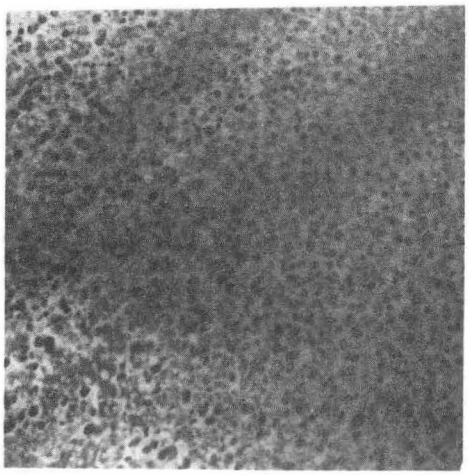

$1 \times 10^{16}/cm^2$
900°C 30 minutes

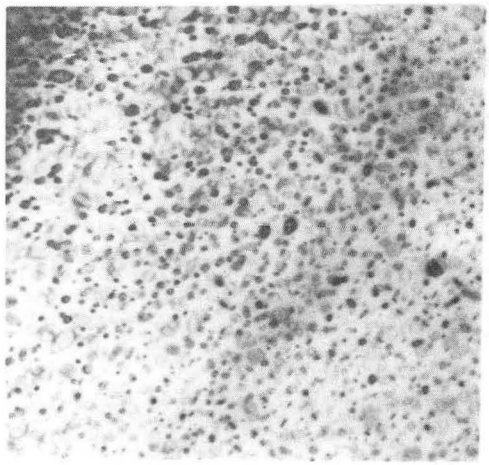

$1 \times 10^{16}/cm^2$
900°C 8 hours

100 keV ^{72}Ge, {100}, Waycool Endstation
Bright Field, g_{040}

XBB 873-2390

Appendix 1c

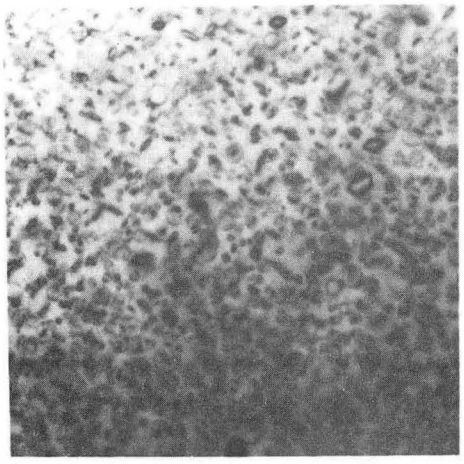

1 x 10^{15}/cm^2
900°C 60 minutes

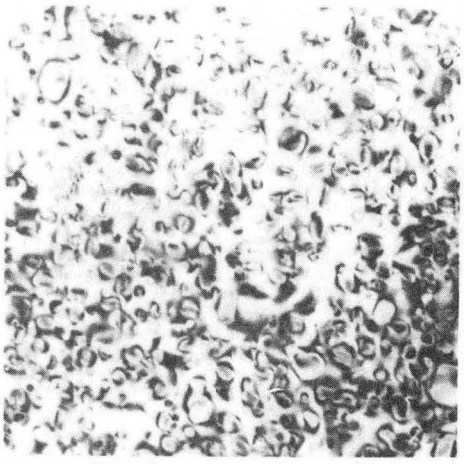

1 x 10^{15}/cm^2
900°C 8 hours

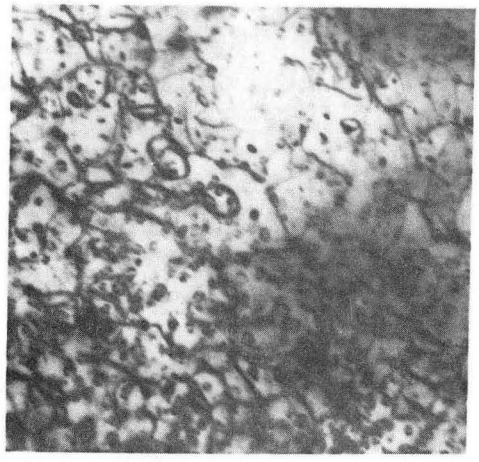

2 x 10^{16}/cm^2
900°C 60 minutes

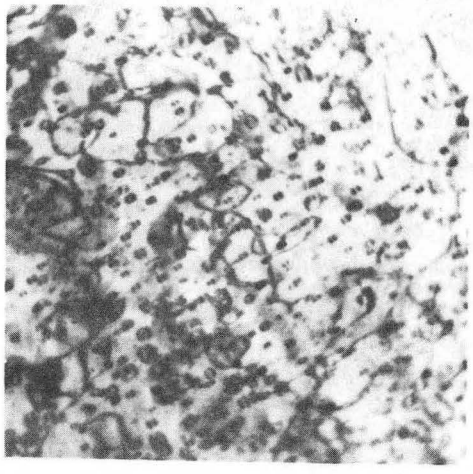

2 x 10^{16}/cm^2
900°C 8 hours

100 keV ^{27}Al, {100}, Waycool Endstation
Bright Field, g_{040}

XBB 873-2391

Appendix 1d

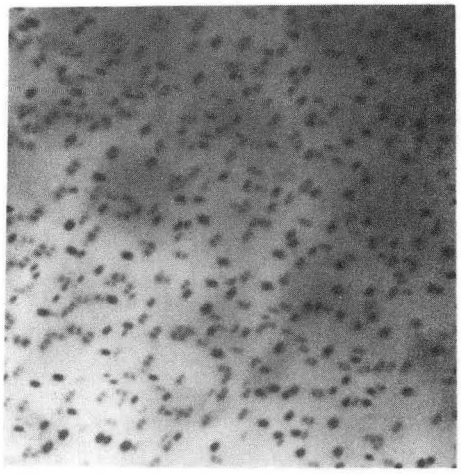

$2 \times 10^{14}/cm^2$
900°C 60 minutes

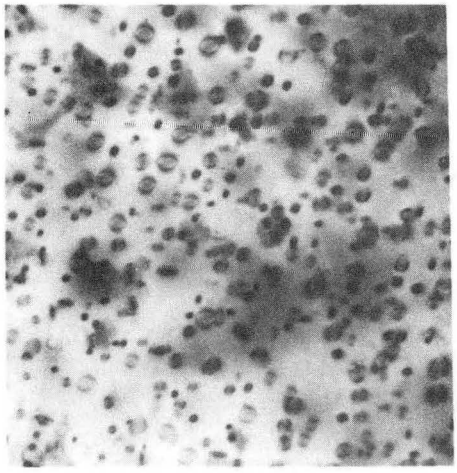

$2 \times 10^{14}/cm^2$
900°C 8 hours

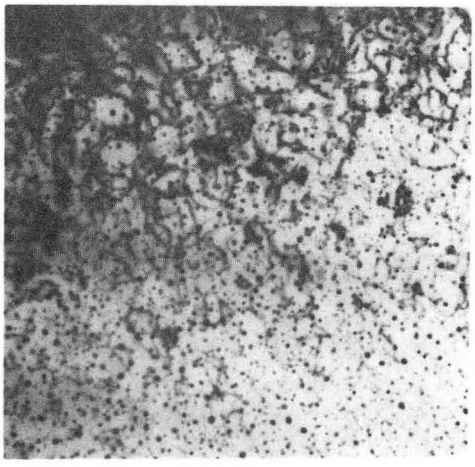

$1 \times 10^{16}/cm^2$
900°C 60 minutes

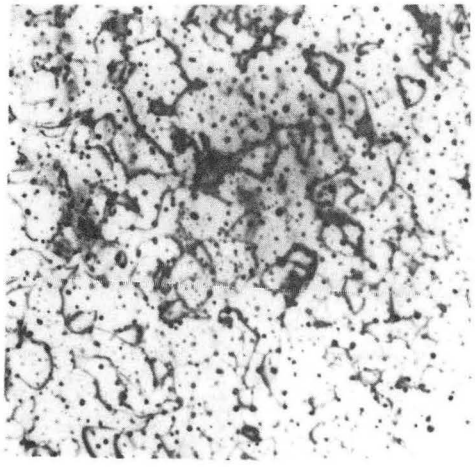

$1 \times 10^{16}/cm^2$
900°C 8 hours

190 keV ^{122}Sb, {100}, Waycool Endstation
Bright Field, g_{040}

XBB 873-2392

Appendix 1e

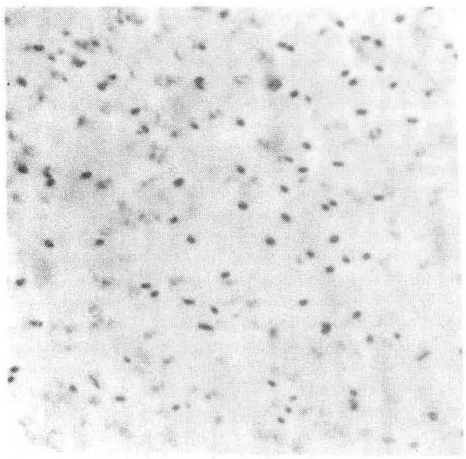

$5 \times 10^{14}/cm^2$
900°C 30 minutes

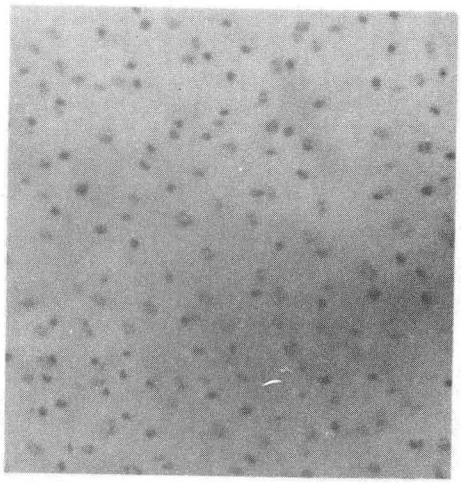

$5 \times 10^{14}/cm^2$
900°C 8 hours

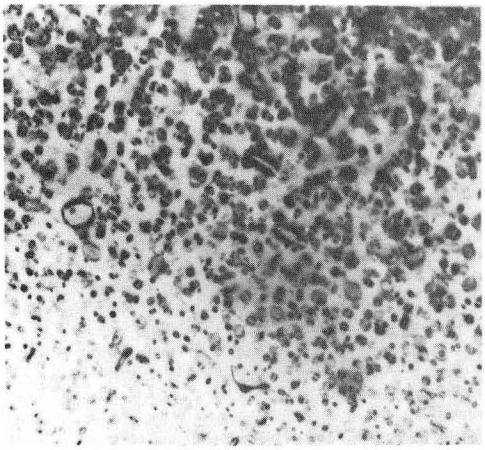

$1 \times 10^{16}/cm^2$
900°C 30 minutes

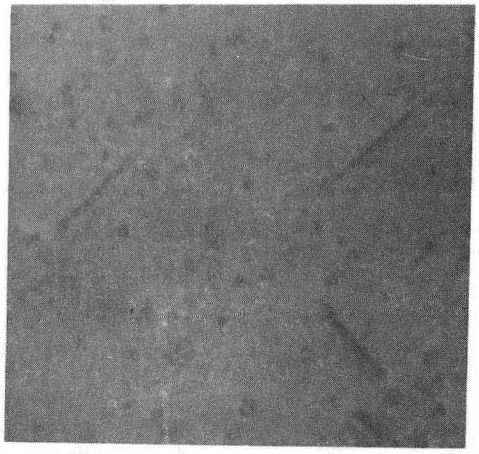

$1 \times 10^{16}/cm^2$
900°C 8 hours

100 keV ^{75}As, {100}, Waycool Endstation
Bright Field, g_{040}

XBB 873-2393

Appendix 1f

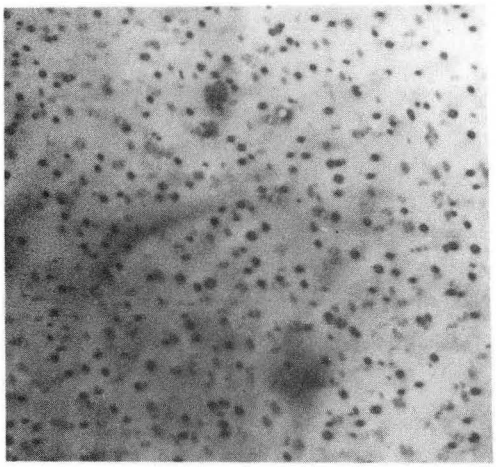

$2 \times 10^{14}/cm^2$
900°C 30 minutes

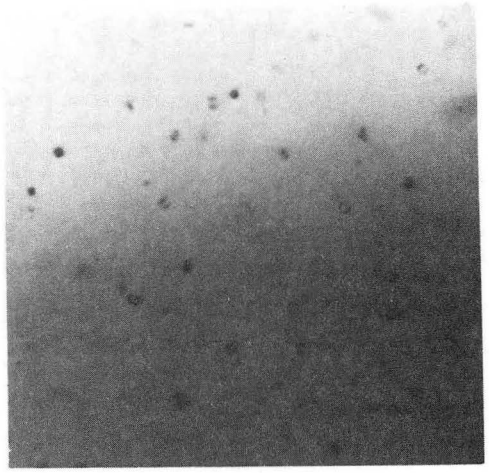

$2 \times 10^{14}/cm^2$
900°C 8 hours

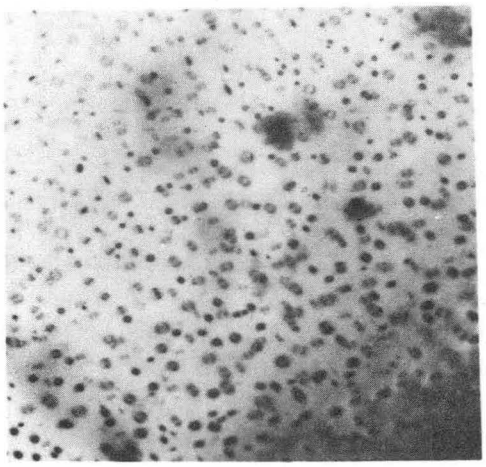

$1 \times 10^{15}/cm^2$
900°C 30 minutes

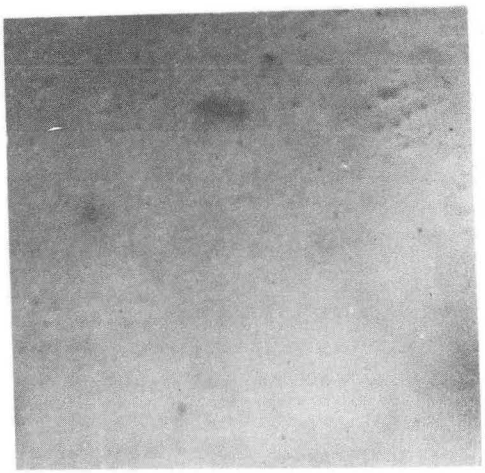

$1 \times 10^{15}/cm^2$
900°C 8 hours

100 keV ^{70}Ga, {100}, Waycool Endstation
Bright Field, g_{040}

XBB 873-2394

Appendix 1g

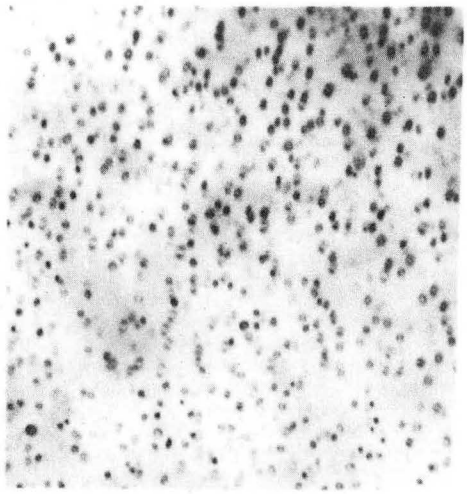

$1 \times 10^{15}/cm^2$
900°C 30 minutes

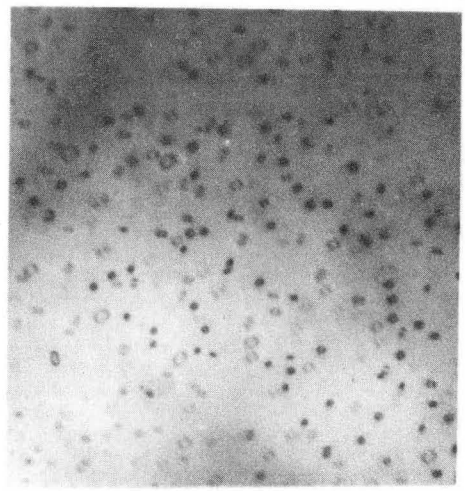

$1 \times 10^{15}/cm^2$
900°C 8 hours

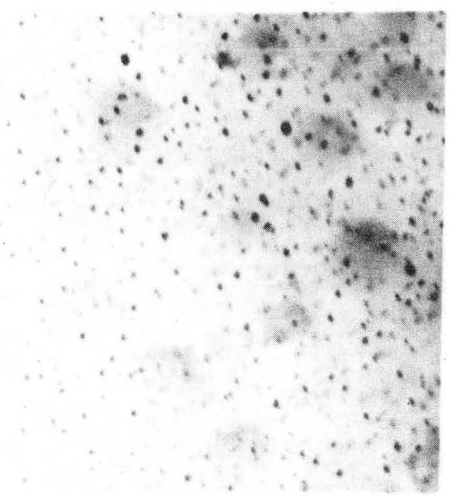

$1 \times 10^{16}/cm^2$
900°C 30 minutes

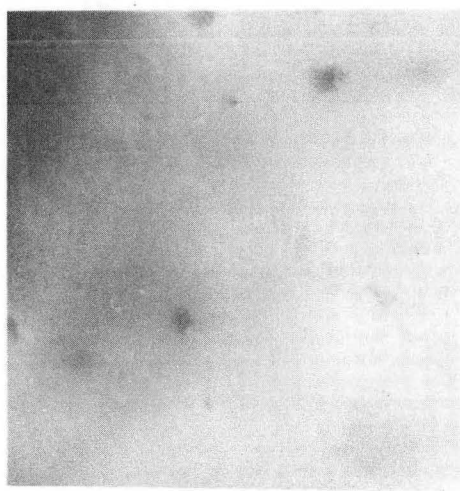

$1 \times 10^{16}/cm^2$
900°C 8 hours

50 keV ^{31}P, {100}, Waycool Endstation
Bright Field, g_{040}

XBB 873-2395

This report was done with support from the Department of Energy. Any conclusions or opinions expressed in this report represent solely those of the author(s) and not necessarily those of The Regents of the University of California, the Lawrence Berkeley Laboratory or the Department of Energy.

Reference to a company or product name does not imply approval or recommendation of the product by the University of California or the U.S. Department of Energy to the exclusion of others that may be suitable.

LAWRENCE BERKELEY LABORATORY
TECHNICAL INFORMATION DEPARTMENT
UNIVERSITY OF CALIFORNIA
BERKELEY, CALIFORNIA 94720